Energy Management and Power System Operation Vol 7

Dirk Fetzer

Development of a MATLAB/Simulink Framework for Phasor-Based Power System Simulation and Component Modeling Based on State Machines

e²n Energiemanagement und Betrieb elektrischer Netze

Fraunhofer IEE

KDEE Kompetenzzentrum für Dezentrale Elektrische Energieversorgungstechnik

Energy Management and Power System Operation

Vol. 7

Edited by
Prof. Dr.-Ing. Martin Braun
University of Kassel

Dirk Fetzer

Development of a MATLAB/Simulink Framework for Phasor-Based Power System Simulation and Component Modeling Based on State Machines

kassel
university
press

This work has been accepted by the Faculty of Electrical Engineering / Computer Sciences of the University of Kassel as a thesis for acquiring the academic degree of Doktor der Ingenieurwissenschaften (Dr.-Ing.).

Supervisor: Prof. Dr.-Ing. Martin Braun (University of Kassel)
Co-Supervisor: Prof. Dr.-Ing. Antonello Monti (RWTH Aachen)

Defense day: 21st September 2018

Bibliographic information published by Deutsche Nationalbibliothek
The Deutsche Nationalbibliothek lists this publication in the Deutsche Nationalbibliografie; detailed bibliographic data is available in the Internet at http://dnb.dnb.de.

Zugl.: Kassel, Univ., Diss. 2018
ISBN 978-3-7376-0608-0 (print)
ISBN 978-3-7376-0609-7 (e-book)
DOI: http://dx.medra.org/10.19211/KUP9783737606097
URN: https://nbn-resolving.org/urn:nbn:de:0002-406094

www.upress.uni-kassel.de

Printing Shop: Print Management Logistics Solutions, Kassel
Printed in Germany

Danksagung

Diese Arbeit entstand im Rahmen meiner Tätigkeit als wissenschaftlicher Mitarbeiter am Fachgebiet für Energiemanagement und Betrieb elektrischer Netze der Universität Kassel im Zeitraum Mitte 2013 bis Mitte 2018.

Mein Dank gilt zuerst Professor und Fachgebietsleiter Martin Braun für die Möglichkeit diese Dissertation im Rahmen meiner Tätigkeit am Fachgebiet zu verfassen und mich während dieser Zeit in einem sehr produktiven und freundschaftlichen Arbeitsumfeld fachlich, sowie persönlich weiterzuentwickeln. Ohne seine engagierte Begleitung wäre diese Dissertation nicht möglich gewesen. Ich danke Ihm auch sehr für den fachlichen Freiraum, den ich genießen durfte. Dieser hat es mir erlaubt die Dissertation in meinem Interessensschwerpunkt, dem Berechnen und der Simulation von elektrischen Energieversorgungssystemen zu verfassen. Vielen lieben Dank Martin!

Bei Professor Antonello Monti von der RWTH Aachen bedanke ich mich sehr herzlich für die Übernahme des Zweitgutachtes. Ich schätze dies sehr, da die Terminkalender doch immer sehr voll sind. Außerdem habe ich während meines Studiums an der RWTH Aachen und während meiner Masterarbeit am EON ACS wertvolle Grundlagen und Spezialwissen über die Simulation elektrischer Netze von Professor Monti und seinem damaligen Mitarbeiter Andrea Benigni erlernt. Dafür bedanke ich mich nochmals ganz herzlichst.

Mein Dank gilt ganz Besonders der Firma EnergieNetz Mitte GmbH für das Verfügbar machen von Netzdaten, die im Rahmen dieser Arbeit genutzt werden durften.

Ein ganz besonderer Dank gilt meinen beiden Bürokollegen Dr. Dario Lafferte und Gustav Lammert. Wir saßen nicht nur in einem Büro, sondern wir haben uns durchgehend persönlich und fachlich bei der Erstellung von Veröffentlichungen und bei dieser Dissertation unterstützt. Wir haben immer sehr produktiv, freundschaftlich und mit viel Freude zusammengearbeitet. Ohne die fachliche Unterstützung und den Motivationskünsten von Dario und Gustav wäre diese Dissertation nicht entstanden. Insgesamt kann ich nur sagen, dass ich sehr dankbar dafür bin, dass ich ein Büro mit euch teilen durfte.

Ich bedanke mich besonders bei Herrn Diplom Ingenieur Bernd Gruß. Durch seine fachliche Unterstützung und Beratung im Labor hat er mir interessantes und wertvolles praktisches Knowhow vermittelt. Außerdem bedanke ich mich für die zahlreichen interessanten und motivierenden Gespräche.

Ich danke vielmals Dr. Stefan Gehler, Dr. Jan Hegemann, Tina Paschedag und Dr. Robert Schmoll für den fachlichen und persönlichen Austausch und dafür, dass sie den anspruchsvollen Job der Teamleitung in unserem damals noch so jungen Fachbebiet übernommen haben und das Fachgebiet maßgeblich geformt haben. Nur durch ihren engagierten Einsatz sind die Strukturen entstanden, die es nun ermöglichen, dass zahlreiche Dissertationen am Fachgebiet vorangetrieben werden. Ich danke von ganzem Herzen Elisabeth Drayer für den fachlichen, persönlichen und motivierenden Austausch während der kompletten Zeit am Fachgebiet. Elisabeth, du warst eine wirkliche Bereicherung. Ich bedanke mich außerdem natürlich beim kompletten e2n-Team für die Zusammenarbeit. Dazu gehören Leon Thurner, Florian Schäfer, Dr.-Ing. Nils Borhorst, Diplom Ingenieurin Tina Paschedag, Gourab Banerjee, Priyanka Chaudhari, Marcel Ernst, Jonas Haack, Christian Hachmann, Alexander Klingmann, Jannis Kupka, Zheng Liu, Steffen Meinecke, Jan-Hendrik Menke, Florian Schäfer und alle die ich hier vergessern habe.

Ich bedanke mich bei Gustav Lammert, Dario Lafferte, Elisabeth Drayer, Tina Paschedag, Robert Schmoll und Christian Hachmann für das Korrekturlesen dieser Dissertation und die zahlreichen nützlichen Anmerkungen.

Ich bedanke mich bei meinen Studenten Kai Fischbach, Johannes Weide, Manuel Nuhn, Christian Jähner, Matteo Troncia und Daniel Solano. Alle durfte ich entweder im Rahmen einer HiWi-Anstellung oder im Rahmen einer Bachelor- oder Masterarbeit betreuen. Ich kann nur sagen, es hat mir sehr viel Freude bereitet mit euch zusammenzuarbeiten und euch die Welt der Simulation elektrischer Netzer näher zu bringen.

Ich bedanke mich bei allen Kommilitonen die mich in meiner Studienzeit begleitet haben. Ganz besonders bei Dr. rer. nat. Christian (Bietz) Eberl, Tobias Lohse, Markus Harden und allen anderen aus der Zeit des Physikstudiums in Göttingen. Ich bedanke mich bei meinem Freund Sascha Schneider für die Zeit in San Diego und alles was noch kommen wird. Mein ganz besonderer Dank gilt Danny D'Souza, der mir in den ersten sechs Studiensemestern als WG-Mitbewohner durch sein Vorbild und seine Ratschläge sehr früh aufgezeigt hat, auf was es im akademischen Umfeld ankommt.

Ich bedanke mich bei allen Lehrern, Betreuern und Professoren die zu meiner Ausbildung beigetragen haben. Dazu zählen im besonderen Herr Hellwig, Burkhard Wilm, Frau Tolle-Nelke, Arno Leithäuser, Herr Hackel, Professor Dr. Hans-Ulrich Krebs, Dr. Tobias Liese, Dr. Uwe Boettcher und Professor Frank E. Talke.

Sehr danke ich meinen langjährigen Freunden David und Sascha, welche mein Leben sehr bereichern, für die Unterstützung, Gespräche und Weisheiten vor und während der Promotion. Außerdem Danke ich von ganzem Herzen Michael, Christian, Suzana, Harald und allen anderen, die fortwährend ihre Sichtweise auf die Dinge mit mir geteilt haben und von denen ich viel lernen konnte. Vielen, vielen lieben Dank an Tess, Vanessa und Stephie. Nur durch eure Mitwirkung ist diese Dissertation so möglich gewesen, vielen Dank!!!

Ich danke meiner kompletten Familie, also meiner lieben Mutter, meinem lieben Vater, Antje, Horst und meinen beiden Brüdern Frank und Jochen und natürlich meinen Großeltern für die Unterstützung in den zurückliegenden Jahren, und zwar nicht nur während der Dissertation. Ich bin sehr froh, dass ich euch in meinem Leben habe und von euch lernen konnte und kann und dass wir uns stets zusammen weiterentwickeln, auf der relativen, und auch auf der absoluten Ebene.

Abstract (German)

Diese Arbeit besteht aus vier Hauptteilen. Im ersten Teil wurde ein Algorithmus entwickelt, der spannungsabhängige Einspeisung von Wirk- und Blindleistung, auch genannt $P(V)$ und $Q(V)$, in den Newton Power Flow-Algorithmus integriert. Methoden nach dem derzeitigen Stand der Technik berücksichtigen $P(V)$ und $Q(V)$ in einer externen Schleife, was die Berechnung mehrerer Leistungsflüsse notwendig macht. Dies ist zeitintensiv und wird mit dem in dieser Arbeit vorgestellten internen Algorithmus gelöst. Der interne Algorithmus erreicht eine Beschleunigung von bis zu einer Größenordnung gegenüber dem Stand der Technik und hat den Vorteil einer verbesserten Robustheit. Es wird eine Laboruntersuchung vorgestellt, bei der der Algorithmus die gemessene statische Spannung eines netzgekoppelten Wechselrichters in einem Zweibussystem erfolgreich vorhersagt.

Im zweiten Teil wird ein Phasor-Framework entwickelt, das die dynamische Simulation von elektrischen Energiesystemen ermöglicht. Das entwickelte Framework ermöglicht die einfache Integration und Modifikation von Komponentenmodellen, sowie die einfache Anpassung neuer Algorithmen. Das Framework ist ein Whitebox-System. Das bedeutet, dass alle Berechnungsschritte und der komplette Code vom Anwender identifiziert werden. Das Phasor-Framework ist für den Einsatz im Bereich Forschung und Lehre konzipiert.

Im dritten Teil werden Modelle für das Phasor-Framework entwickelt. Die Modelle umfassen einen Synchrongenerator, einen Dieselgenerator und ein Photovoltaik Modell für kleinere Anlagen im Niederspannungsnetz. Innerhalb des Photovoltaik-Modells liegt der Schwerpunkt auf der Darstellung des dynamischen Verhaltens von $P(V)$, $Q(V)$ und $P(f)$. Das Modell ist für den Einsatz in dynamischen Studien im Bereich von Sekunden bis Minuten vorgesehen. Das Modell ist in das Phasor-Framework integriert. Das dynamische Verhalten von $P(V)$ und $Q(V)$ wurde erfolgreich mit Messungen eines handelsüblichen Wechselrichters im Labor gegengeprüft.

Im vierten Teil der Arbeit werden das Phasor-Framework und die entwickelten Modelle verwendet, um zu untersuchen unter welchen Bedingungen das Wiederzuschaltverhalten von Photovoltaikanlagen in einem dieselbetriebenen Inselnetz in der Niederspannung stabil ist. Fokus liegt dabei auf der Untersuchung von mehreren kleinen Photovoltaikanlagen, welche nach verschiedenen Normen eingestellt sind, verhalten. Die Studie zeigt, dass ein periodisches An- und Abschalten von Photovoltaikanlagen während des Wiedereinschaltvorgangs vorkommen kann.

Abstract (English)

This work consists of four main parts. In the first part an algorithm was developed which incorporates voltage dependent active and reactive power injections, also called $P(V)$ and $Q(V)$, into the Newton power flow algorithm. State-of-the-art methods consider $P(V)$ and $Q(V)$ in an external loop which makes the calculation of multiple power flow problems necessary and which is time consuming. This issue is solved with the internal algorithm presented in this thesis. The internal algorithm reaches a speedup of up to one magnitude compared to the state-of-the-art method and has the advantage of an improved robustness. A laboratory investigation is presented in which the algorithm successfully predicts the measured static voltage of a grid coupled inverter in a two bus system.

In the second part, a phasor-framework was developed which enables the dynamic simulation of electric power systems. The developed framework allows for easy integration and modification of component models and also allows for straight forward adaption of new algorithms. The framework is a white-box system. That means that all calculation steps and the complete code can be inspected by the user. The phasor-framework is intended to be used in the area of research and education where this kind of flexibility is beneficial.

In the third part, models for the phasor-framework are developed. The models include a standard synchronous generator, a diesel generator and a small-scale photovoltaic system model. Within the photovoltaic model, the main focus lays on the representation of the dynamic $P(V)$, $Q(V)$ and $P(f)$ behavior. The model is intended to be used in dynamic studies in the range of seconds up to minutes. The model is integrated into the phasor-framework. The dynamic $P(V)$ and $Q(V)$ behavior is validated against an off-the-shelf commercial inverter.

In the fourth part of the thesis, the phasor-framework and the developed models are used in order to investigate the stability of the reconnection behavior of photovoltaic systems in a diesel-powered low-voltage island grid. The focus is on the investigation of serveral small-scale photovotlaic systems which behave according to different grid codes. The study shows that a periodical connection and disconnection of photovoltaic systems can occur during the reconnection process.

Authors Publication List

Journals

(a) **D. Fetzer**, G. Lammert, S. Gehler, J. Hegemann, R. Schmoll, M.Braun, *Integration of voltage dependent power injections of distributed generators into the power flow by using a damped Newton method*, International Journal of Electrical Power and Energy Systems, Volume 99, 2018, Pages 695-705, ISSN 0142-0615

(b) U. Boettcher, **D. Fetzer**, H. Li, R. A. de Callafon, F. E. Talke, *Reference Signal Shaping for Closed-loop Systems with Application to Seeking in Hard Disk Drives*, IEEE Transactions on Control Systems Technology, Vol. 20, No. 2, pp. 335-345, March 2012

Conference Proceedings

(c) **D. Fetzer,** G. Lammert, A. Ishchenko, L. Tabit, M.Braun, *A Flexible MATLAB/Simulink RMS-Framework for Electrical Power Systems Designed for Research and Education*, ISGT 2018

(d) **D. Fetzer**, G. Lammert, T. Paschedag, D. Lafferte, K. Fischbar, M. Nuhn, C. Jaehner, H. Becker, L.R. Roose, M. Braun, *Reconnection of Photovoltaic Systems in Low-Voltage Diesel-Powered Microgrids*, 1st International Conference on Large-Scale Grid Integration of Renewable Energy in India, New Delhi, September 6-8 2017

(e) D. Lafferte, A. Klingmann, **D. Fetzer**, G. Lammert, C. Hachmann, T. Paschedag, M. Braun, Black Start and Island Operation of Distribution Grids with Significant Penetration of Renewable Resources, 1st International Conference on Large-Scale Grid Integration of Renewable Energy in India, New Delhi, September 6-8, 2017

(f) **D. Fetzer**, G. Lammert, K. Fischbach, M. Nuhn, J. Weide, D. Lafferte, T. Paschedag, M. Braun, *Modelling of Small-Scale Photovoltaic Systems with Active and Reactive Power Control for Dynamic Studies, 6th Solar Integration Workshop*, Vienna, Austria, November 14-15, 2016.

(g) G. Lammert, L. D. Pabón Ospina, P. Pourbeik, **D. Fetzer**, M. Braun, *Implementation and Validation of WECC Generic Photovoltaic System Models in DIgSILENT PowerFactory*, IEEE PES General Meeting 2016, Boston, USA, July 17-21, 2016.

(h) G. Lammert, J. C. Boemer, D. Premm, O. Glitza, L. D. Pabón Ospina, **D. Fetzer**, M. Braun, *Impact of Fault Ride-Through and Dynamic Reactive Power Support of Photovoltaic Systems on Short-Term Voltage Stability*, IEEE PowerTech 2017, Manchester, Great Britain, June 18-22, 2017

(i) M. Vogt, F. Marten, L. Löwer, D. Horst,K. Brauns, **D. Fetzer**, J.-H. Menke, M. Troncia, J. Hegemann, C. Tobermann, M. Braun, *Evaluation of interactions between multiple grid operators based on sparse grid knowledge in context of a smart grid co-simulation environment*, IEEE PowerTech, June 29-July 2, 2015, Eindhoven

(j) U. Boettcher, **D. Fetzer**, H. Li., K. Amemiya, R. A. de Callafon, F. E. Talke, *Reference Signal Shaping for Time- Optimal Track-Seeking in Hard Disk Drives*, Asia-Pacific Magnetic Recording Conference, Singapore, 2010

(k) A. Benigni, F. Adler, **D. Fetzer**, A. Monti, R. W. De Doncker, *Real-time simulation of a doubly fed induction generator wind turbine on a new DSP based hardware platform*, 15th European Conference on Power Electronics and Applications (EPE), 2013

Publications used in this Thesis

Some contents of this work has been published previously by the author or is currently being published by the author. The mapping between the publications and the corresponding chapters of this thesis is shown in Table 1.

Table 1: Mapping between contents of the thesis and corresponding publications.

Chapter	**Contents partly published in**
Chapter 2	(a)
Chapter 3	(c)
Chapter 4	(d), (f)
Chapter 5	(d)

Supervised thesis and teaching

Supervised theses

- Kai Fischbach, *Enhanced Data Management and Model Development for a Dynamic Grid Simulation Solver*, **Bachelor project**, November 2015
- Kai Fischbach, *Modellentwicklung und Untersuchung der Stabilität der spannungsabhängigen Wirkleistungseinspeisung von Photovoltaik-Wechselrichtern*, **Bachelor thesis**, May 2016
- Manuel Nuhn, *Modellierung und Untersuchung des dynamischen Verhaltens von Photovoltaikanlagen in Niederspannungsnetzen*, **Master thesis**, May 2017
- Christian Jähner, Analyse, *Konvertierung und Parametrierung von Daten für die dynamische Simulation von elektrischen Netzen in Matlab/ Simulink*, **Bachelor thesis**, June 2017
- Kai Fischbach, *Development, Implementation and Comparison of EMT and RMS Voltage Source Inverter Models for Micro Grid Applications*, **Master thesis**, April 2018
- Johannes Weide, *Operation of a Diesel-PV Island Grid*, **Master thesis**, currently intermitted

Contents

Abstract **i**

Publication List **iii**

Supervised Thesis and Teaching **vi**

Contents **vii**

1 Introduction **1**

1.1 Objectives 2

1.2 Thesis structure 3

2 Efficient power flow routine **5**

2.1 Introduction 5

2.2 Modeling of voltage dependent power injections 7

2.2.1 Piecewise function 7

2.2.2 Smoothing function 8

2.2.3 Exemplary P(V) and Q(V) characteristics 9

2.3 Power flow formulation 10

2.4 Integration into the power flow 12

2.4.1 External algorithm 12

2.4.2 Internal algorithm 14

2.5 MATLAB power flow tool 16

2.5.1 Data format 16

2.5.2 Program execution 17

2.6 Test cases 18

2.6.1 Two-bus system 18

2.6.2 Performance Analysis 26

2.7 Conclusion 27

3 Phasor-Framework **29**

3.1 Introduction 29

3.2 Comparison of phasor based simulation tools 30

3.3 Design objectives for phasor-framework 33

3.4 Framework overview 35

3.4.1 Data structure 35

3.4.2 Generation of valid data sets and data parsing 37
3.4.3 Workflow 37
3.4.4 Simulation methodology 38
3.4.5 Measurements 39
3.5 Grid model 40
3.5.1 Grid model equations 40
3.5.2 Grid model implementation 41
3.6 Component models 41
3.6.1 Modeling approach 42
3.7 Fault simulation 44
3.8 Parameter variation 46
3.9 Discussion on phasor-framework 47
3.10 Conclusion 49

4 Model development 51
4.1 Introduction 51
4.2 Synchronous generator 52
4.2.1 Electrical equations 53
4.2.2 Mechanical equations 55
4.2.3 dq-transformation 56
4.2.4 Conversion of standard into fundamental parameters 57
4.2.5 Initialization 59
4.3 Diesel generator 61
4.4 Photovoltaic system 63
4.4.1 Introduction to photovoltaic system modeling 63
4.4.2 Model basis - the generic WECC model 64
4.4.3 Model overview 65
4.4.4 Frequency dependent active power injection 68
4.4.5 Initialization 71
4.4.6 Model testing against real-life inverter 72

5 Diesel-PV Microgrid Study 81
5.1 Introduction 81
5.2 Modelling 82
5.2.1 Networks 83
5.2.2 Diesel frequency control 83
5.3 Reconnection of new PV systems 84
5.3.1 Available PV power smaller than load 85
5.3.2 Available PV power larger than load 85
5.3.3 Load smaller than minimum load of diesel unit 87
5.4 Reconnection of old PV systems 87
5.4.1 Available PV power smaller than load 88
5.4.2 Available PV power identical to load 88
5.5 Reconnection of a mix of old and new PV systems 90
5.5.1 12 new and 8 old PV systems 90

5.5.2 3 new and 17 old PV systems 91
5.6 Conclusion 92

6 Conclusion **95**
6.1 Novelties 95
6.2 Outlook 97

A Modeling approach **99**
A.1 Example: Internal VSI and CSI vectors 99
A.2 Adding new components 100

B Numerical Example for Internal Algorithm **107**

Nomenclature **110**

List of Symbols **111**

List of Figures **116**

List of Tables **119**

List of Listings **121**

Bibliography **122**

Chapter 1

Introduction

The need for a more sustainable electricity generation is driven by various factors including politics, climate change mitigation and economics. The share of renewable energy resources (RES) in the overall electricity production in the European Union was about 16 % in 2015 and is expected to grow to about 21 % in 2020 [1]. Looking even more into the future, the worldwide share of RES among the electricity supply will be about 50 % in 2050 according to recent studies [2]. Integrating these large shares of RES into the electrical network poses multiple challenges in the fields of production, distribution, policy design, economics and industry.

The generation of electricity from renewable sources is mostly based on supply units like offshore and onshore windparks, photovoltaic (PV) systems, hydro power plants or biogas plants. In general, large wind parks and large solar parks are connected to the high-voltage level. Off-shore windparks are often connected via DC-links. Smaller units are connected to the medium or low-voltage level. Thus, the production of energy based on distributed RES affects the complete electrical energy system ranging from the distribution to the transmission grid. As electrical energy was historically produced by a few centralized and large power plants, the power system itself was designed to enable the distribution of the electrical energy from a few generating units to the consumers. With the growing share of RES the structure of the power system changes from centralized to decentralized generation. For example, the penetration of medium and low-voltage grids with inverter coupled distributed generators (DGs) has increased substantially in recent years and is expected to keep growing [3, 4]. In summary, it can be said that the increasing amount of distributed RES in power systems causes more complexity [5].

The high fluctuation of renewable distributed energy resources (DER) can cause voltage fluctuations [6], which make it challenging for grid operators to adhere to their respective static voltage quality standards like IEC 60038 [7] or EN 50160 [8]. This issue has to be taken into account during grid planning and operation. Furthermore, the intermittency of DER has an influence onto the dynamic behavior of the overall power system and DER might cause instabilities that need to be addressed appropriately in grid codes [9].

Some questions concerning the static or dynamic behavior of DER can be tackled by laboratory experiments. However, out of logistic and economic reasons it is practically impossible to recreate realistic power systems in a laboratory environment and perform measurements. To investigate large-scale, real-life power systems, it is required to use a simulation approach in which the most important physical aspects of the system under investigation are modeled. Simulation approaches are applied to a wide range of power system problems like grid planning [10, 11], power system stability [12, 13, 14] or in the area of microgrid control [15, 16]. The practical relevance of dynamic grid studies is elaborated in [17] where it is shown that a significant amount of utilities and system operators are working on dynamic modeling and simulation of DERs.

There is a growing demand of representing DER in static as well as in dynamic power system studies. There are, of course, sophisticated commercial and open-source simulation tools available that are specifically focused on simulating the electrical power system. These tools are also able to incorporate DERs into static and dynamic simulations. However, many of these tools have limitations in the area of rapid model development or they are black box tools in which the grid calculation algorithms cannot be seen by the user which is a drawback for research and education.

The main goal of this work is to close this gap and develop a simulation environment which can perform static and dynamic simulations of electrical power systems. Especially it is a goal to design the simulation environment such that it is suited for a rapid component model development that is easy to use and has little software overhead.

1.1 Objectives

There are four specific objectives of this thesis:

Objective 1 Modern DER have the ability of voltage dependent active and reactive power injection, also called $P(V)$ and $Q(V)$. Thus, the first objective of this thesis is the development of a power flow algorithm that is able to handle the $P(V)$ and $Q(V)$ behavior and be computationally light at the same time.

Objective 2 The second objective is the development of a phasor simulation environment that enables a relatively easy integration of new component models and allows adjustments of existing component models. Furthermore, the phasor simulation environment should be targeted for the use in research and education and therefore fostering power system and scripting knowledge. Included in this objective is also the integration of a synchronous machine model into the simulation environment as this is one of the most important components of a power system.

Objective 3 The third objective of this work is to develop a realistic, small-scale PV system model, that behaves according to the German low-voltage grid code. The model is integrated into the simulation environment in order to enable power system studies with realistic small-scale PV system models. The novelty

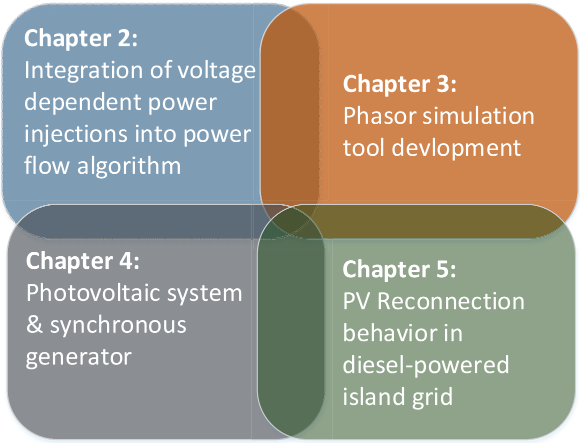
Chapter 2:
Integration of voltage dependent power injections into power flow algorithm
Chapter 3:
Phasor simulation tool devlopment
Chapter 4:
Photovoltaic system & synchronous generator
Chapter 5:
PV Reconnection behavior in diesel-powered island grid

Figure 1.1: Thesis structure

of this objective is the usage of a visual state machine model in the PV system model which simplifies the modeling process.

Objective 4 The fourth objective is the investigation of the stability of the reconnection behavior of PV systems in a low-voltage island grid, that is driven by a diesel generator. The PV systems are modeled according to either the present or old German low-voltage grid code. The investigation is also focused on the behavior of a mix of old and new PV systems.

1.2 Thesis structure

The four main chapters of the thesis can be seen in Fig. 1.1.

In Chapter 2 the development of the power flow routine is described. The routine incorporates voltage dependent active and reactive power injections into the Newton Raphson algorithm. The chapter starts with the description of the modeling process of voltage dependent power injections in Section 2.2. The power flow formulation is presented in Section 2.3. The integration of $P(V)$ and $Q(V)$ into the power flow is shown in Section 2.4. In this section the state-of-the-art external method is presented as well as the internal method developed within this work. Some details about the power flow tool implemented in MATLAB are presented in Section 2.5 and test cases are shown in Section 2.6. The test cases also contain a laboratory investigation which compares the results of the developed algorithm with measurements of a inverter in a two bus system. The chapter ends with a conclusion in Section 2.7.

In Chapter 3 the development of a phasor-framework is presented. The Chapter starts with a review and comparison of phasor based simulation tools in Section 3.2. After that, an overview of the framework is given in Section 3.4 which includes, beside other points, an explanation of the the data structure, the simulation workflow and the simulation methodology. The design and implementation of the grid and component models are explained in Section 3.5 and 3.6, respectively. The implementation of faults is shown in Section 3.7 and the possiblity of parameter variations is explained in Section 3.8. A discussion of the developed phasor framework is conducted in Section 3.9 and a conclusion is given in Section 3.10.

Chapter 4 describes the modeling of the main components of the framework. The synchronous generator model is explained in detail in Section 4.2 including electrical and mechanical equations as well as the dq-transformation and the initialization. In Section 4.3 the diesel model is described briefly. In Section 4.4 the developed PV model is presented. The section also contains a laboratory validation of the model.

In Chapter 5 the reconnection behavior of PV systems in a low-voltage diesel-PV microgrid is investigated. After the network model and frequency control strategy of the diesel generator is explained in Section 5.2, the reconnection behavior of new and old PV systems is explained in Section 5.3 and Section 5.4. The reconnection behavior of a mix of old and new PV systems is presented in Section 5.5. A conclusion of the investigation is given in Section 5.6.

The conclusion and an outlook of the thesis is given in Chapter 6.

Chapter 2

Efficient power flow routine

2.1 Introduction

This chapter has two goals:

1. The first goal of this chapter is to develop a power flow initialization routine that can be used within the RMS-framework presented in Chapter 3.

2. The second goal of this chapter is to develop a power-flow routine with integrated voltage dependent active and reactive power injections. This is the main novelty of this chapter and a **key outcome of this work**.

As the power flow routine is implemented in MATLAB, the power-flow routine can also be integrated into the RMS-framework. Therefore, this chapter will mainly focus on the second goal because it implies the first goal. All in all, in this chapter it will be shown how voltage dependent power injections of DGs can be integrated into the widely known Newton (or Newton-Raphson) power flow algorithm [19]. This is done by incorporating the voltage dependent power injections into the nonlinear grid equations and using a damped Newton method presented in [20]. This solution method is referred to as *internal algorithm* in order to distinguish between the proposed solution method and the state-of-the art method. The damped (under-relaxed, modified) method used in this paper is presented in [20] under the name bisection method. It is based on famous work done in the 19th and 20th century, e.g., [21, 22, 23]. A recent overview can be found in [24].

With the *internal algorithm* the need to perform multiple power flows for a single operating point is no longer given. The *internal algorithm* is compared to the state-of-the-art approach, also called *external algorithm* in this paper. This approach is used in [25, 26, 27]. We conduct this comparison to show the benefits of our new approach compared to the state-of-the-art method. Also, this comparison is used to validate the computation results of the newly developed *internal algorithm.* In the *internal algorithm* the voltage dependent power injection is considered within the Newton algorithm. In the *external algorithm* the voltage dependent power injection is considered outside of the Newton algorithm. Both algorithms are stand-alone and can be used independently of each other.

In this section an ill-conditioned two-bus system shows that the *internal algorithm* can have superior convergence properties compared to the *external algorithm*. Furthermore, the *internal algorithm* is validated for the case of a two-bus system with a laboratory setup. Also, in this work, the proposed *internal algorithm* is applied to the IEEE 118-bus test system and a real German 234-bus grid. It is demonstrated that, for these cases, the *internal algorithm* is computationally faster than the *external algorithm*.

In this chapter, the focus lays on the steady state operating point obtained from the power flow. Thus, the dynamics of this voltage dependent power injection will not be examined explicitly. A discussion on the dynamics can be found in [28, 29]. A detailed introduction and discussion about the economical as well as technical feasibilities can be found in [25, 26, 30, 31]. Also, combinations of voltage dependent power injection together with battery systems have been investigated in [32]. The power flow algorithm developed and described in this chapter serves as the initialization routine for the RMS-framework presented in Chapter 3.

Not investigated in this chapter is the effect of different parameter values for the $P(V)$ and $Q(V)$ characteristics on the resulting voltage profiles of the network. The reason for that is, that the grid operator choses theses characteristics based on grid planning and operation aspects such as loss minimization, minimizing grid reinforcement costs, obtaining optimal voltage profiles or maximizing the hosting capacity of distribution grids for DGs. Details can be found in [25]. Therefore, it is not of practical interest to investigate the convergence behavior or the robustness of the proposed algorithm for different $P(V)$ and $Q(V)$ characteristics parameter values.

The chapter is structured as follows: The modeling of voltage dependent power injection strategies is outlined in Section 2.2. In Section 2.3 the power flow problem is explained briefly. In Section 2.4 the state-of-the-art *external algorithm* and the proposed *internal algorithm* is described. In Section 2.5 the MATLAB power flow tool that was developed during this work is presented briefly from a user perspective. Test cases are presented in Section 2.6. In Section B a numerical example of a 19 node low-voltage test feeder with five photovoltaic systems is presented in Section 2.7 the findings of the chapter are summarized.

This chapter is based on the publication

D. Fetzer, G. Lammert, S. Gehler, J. Hegemann, R. Schmoll, M.Braun, *Integration of voltage dependent power injections of distributed generators into the power flow by using a damped Newton method*, International Journal of Electrical Power and Energy Systems, Volume 99, 2018, Pages 695-705, ISSN 0142-0615

2.2 Modeling of voltage dependent power injections

Power injection methods of DGs can be categorized into two groups, as shown in Table 2.1. Group (a) is characterized by a reactive power injection that is either constant or depends on the injected active power. Here, φ is the angle of the injected complex power and $\cos(\varphi)$ is called power factor. DGs which employ one of these strategies are treated as constant power loads (i.e. P,Q constant) during a power flow. Therefore, no further elaboration is needed for this group from an algorithmic point of view as they are not voltage dependent. Injection methods from control group (a) are already used by transmission and distribution system operators and are specified in technical standards, such as VDE-AR-N 4120 [33].

Group (b) is characterized by a voltage dependent injection of active and/or reactive power. To consider this group within a power flow calculation, the voltage dependency has to be taken into account.

2.2.1 Piecewise function

The voltage dependency can be described with a piecewise function $f(V)$ as shown in Fig. 2.1. This function represents a unified approach for both voltage dependent active and reactive power injection. The maximum and minimum active and reactive power, depicted as y_3 and y_1, are the maximum and minimum possible active and reactive power outputs of the DG in the current operating state. The piecewise function $f(V)$ can be described as

$$f(V) = \begin{cases} y_1, & V \leq V_1 \\ y_1 + \gamma_1 \cdot (V - V_1), & V_1 < V \leq V_2 \\ y_2, & V_2 < V \leq V_3 \\ y_2 + \gamma_2 \cdot (V - V_3), & V_3 < V \leq V_4 \\ y_3, & V_4 < V \end{cases} \tag{2.1}$$

where the gradients are $\gamma_1 = \frac{y_2 - y_1}{V_2 - V_1}$ and $\gamma_2 = \frac{y_3 - y_2}{V_4 - V_3}$.

The method proposed in this work requires to calculate the derivative of (2.1). The derivative of (2.1) with respect to the voltage magnitude is a piecewise constant

Table 2.1: Voltage Dependent Power Injection for Distributed Generators

Group	Description	Injection Method
(a)	Reactive power injection is constant or depends on the injected active power.	$Q_{\text{const.}}$, $\cos(\varphi)_{\text{const.}}$, $\cos(\varphi)(P)$
(b)	Active and/or reactive power injection depend on the bus voltage magnitude.	$P(V)$, $Q(V)$

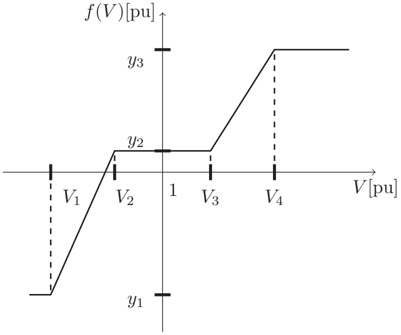

Figure 2.1: Piecewise function $f(V)$ for $P(V)$ and $Q(V)$ voltage dependent power injection. This is a generalized depiction of a characteristic. Positive and negative slopes are possible.

function $g(V)$ with

$$g(V) = \frac{\partial f}{\partial V} = \begin{cases} 0, & V < V_1 \\ \gamma_1, & V_1 < V < V_2 \\ 0, & V_2 < V < V_3 \\ \gamma_2, & V_3 < V < V_4 \\ 0, & V_4 < V. \end{cases} \tag{2.2}$$

The derivative $g(V)$ is discontinuous and not defined at the points V_1, V_2, V_3, V_4. To overcome this issue, a smoothing function will be introduced in Section 2.2.2 .

By choosing appropriate parameters V_1, V_2, V_3, V_4, y_1, y_2, y_3 the reactive and active power characteristics can be expressed by different realizations of $f(V)$. It is:

$$P(V) = f_{\mathrm{P}}(V) \tag{2.3a}$$
$$Q(V) = f_{\mathrm{Q}}(V). \tag{2.3b}$$

The choice of the parameters is typically done by the grid operator based on internal grid planning and operation guidelines. These guidelines may vary for different operators as well as countries.

2.2.2 Smoothing function

To avoid the issue of the discontinuity of the derivative $g(V)$, the following smoothing function for $f(V)$ is used

$$\begin{aligned} f_s(V) =& y_1 + \frac{\gamma_1}{k}\left[\ln(1+e^{k(V-V_1)}) - \ln(1+e^{k(V-V_2)})\right] \\ &+ \frac{\gamma_2}{k}\left[\ln(1+e^{k(V-V_3)}) - \ln(1+e^{k(V-V_4)})\right] \end{aligned} \tag{2.4}$$

where the difference between the smoothing function and the original function is reduced by increasing values of k. The derivative is

$$\begin{aligned} g_s(V) =&\gamma_1 \left[\operatorname{logsig}(k(V-V_1)) - \operatorname{logsig}(k(V-V_2))\right] \\ &+\gamma_2 \left[\operatorname{logsig}(k(V-V_3)) - \operatorname{logsig}(k(V-V_4))\right] \end{aligned} \tag{2.5}$$

with $\operatorname{logsig}(x) = \frac{1}{1+e^{-x}}$ being the log-sigmoid function.

Fig. 2.2 shows the original piecewise linear function f from (2.1) and its derivative g from (2.2) together with the smoothing functions f_s from (2.4) and its derivatives g_s from (2.5) for different values of k. The parameters chosen are $y_1 = 0.18, y_2 = 0, y_3 = -0.18, V_1 = 0.93, V_2 = 0.97, V_3 = 1.03, V4 = 1.07$ and thus $\gamma_1 = \gamma_2 = -4.5$. By analyzing the curves it can be seen that a choice of $k = 600$ results in a reasonable approximation of (2.1) as is shown in Fig. 2.2.

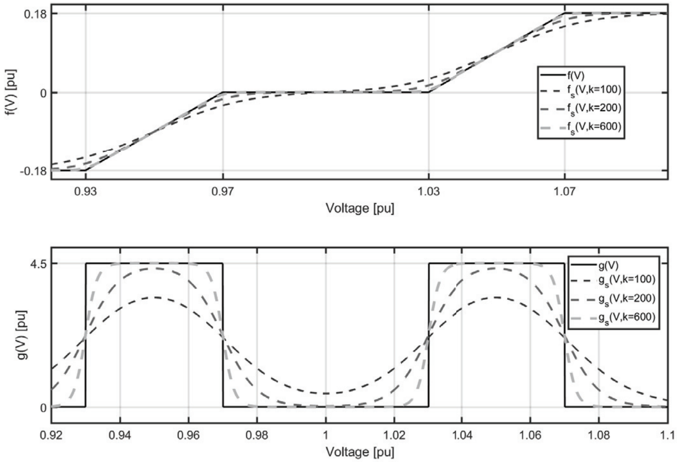

Figure 2.2: Smoothing function f_s and its derivative g_s for different values of k compared to the original piecewise linear function f and its derivative g.

2.2.3 Exemplary P(V) and Q(V) characteristics

To visualize a possible active and reactive power injection characteristic, lets assume a $P(V)$ characteristic with $[V_1, V_2, V_3 V_4] = [1.08, 1.08, 1.08, 1.09]$ and $[y_1, y_2, y_3] = [0.35, 0.35, 0.20]$ and a $Q(V)$ characteristic with $[V_1, V_2, V_3, V_4] = [0.93, 0.97, 1.03, 1.07]$ and $[y_1, y_2, y_3] = [0.18, 0.0, -0.18]$. Both characteristics are shown in Fig. 2.3a and 2.3b. These characteristics will also be used in the case study of the two-bus system presented in Section 2.6.1. It is important to notice that a reduction in active power occurs at $V = 1.08$ pu which is higher than the threshold of $V = 1.07$ pu for the maximum reactive power. In practical application this is a useful setting in order to minimize active power curtailment.

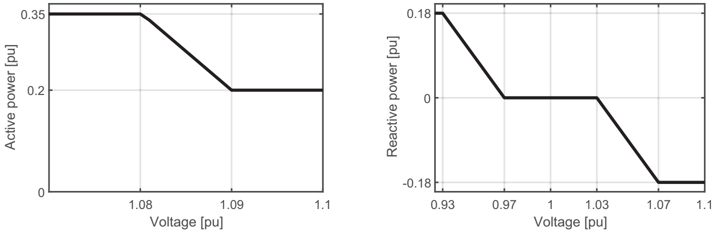

(a) $P(V)$ characteristic

(b) $Q(V)$ characteristic

Figure 2.3: Illustration of exemplary active and reactive power characteristics

2.3 Power flow formulation

In this section the power flow problem is presented. More details concerning power flow can be found in various literature such as [20, 34, 35]. The power flow problem is defined as follows: Assume a power system with n nodes and m DGs with a voltage dependent power injection. Without loss of generality it is assumed that the generators are connected to nodes $1, ..., m$. It is further assumed, that nodes $m+1, ..., n-1$ are connected to constant power loads and thus are modeled as PQ nodes. Node n is chosen as slack node. The active and reactive power characteristics of the DG connected to a node $k \in \{1, ..., m\}$ are described by the piecewise function $P_k = f_{\mathrm{P}k}(V_k)$ and $Q_k = f_{\mathrm{Q}k}(V_k)$, where V_k is the voltage magnitude of node k. A combination of a DG and a constant power load at the same node can be implemented by adjusting the parameters y_1, y_2, y_3 appropriately. If a DG with settings y_1, y_2, y_3 for a $P(V)$ characteristic is present at a bus and a constant power load of power P_{const} is also present at the same bus, then the new setting for the characteristic is $y_{1\,new} = y_1 - P_{\mathrm{const}}$, $y_{2\,\mathrm{new}} = y_2 - P_{\mathrm{const}}$ and $y_{3\,\mathrm{new}} = y_3 - P_{\mathrm{const}}$. The parameters y_1, y_2 and y_3 denote a generation whereas P_{const} is a load, therefore they are subtracted from each other.

For a valid steady-state solution of the system the injected power

$$\underline{S}_k = P_k + \mathrm{j}Q_k \tag{2.6}$$

into each node $k \in \{1, ..., n-1\}$ has to equal the sum of the branch power flows

$$\underline{S}_{k\ell} = P_{k\ell} + \mathrm{j}Q_{k\ell} \tag{2.7}$$

from node k to all connected nodes ℓ. The power mismatch equation describes the difference between those two quantities. $\underline{S}_{k\ell} = 0$ for cases where ℓ is not connected to node k. The power mismatch $\underline{F}_k$ at node k is

$$\underline{F}_k = \underline{S}_k - \sum_{\substack{\ell=1\\ \ell\neq k}}^{n} \underline{S}_{k\ell}. \tag{2.8}$$

As the local voltage characteristic depends on the voltage magnitude, it is practical to use the polar form for complex values. The voltage magnitude and angle at node k are denoted with V_k and δ_k. Thus, the state vector is given by

$$\boldsymbol{x} = \big(V_1, ..., V_{n-1}, \delta_1, ..., \delta_{n-1}\big)^{\mathrm{T}} \tag{2.9}$$

where $\boldsymbol{x} \in \mathbb{R}^{2n-2}$. The angle difference between the voltage at bus k and bus ℓ is defined as

$$\delta_{k\ell} = \delta_k - \delta_\ell. \tag{2.10}$$

The $k\ell$-th element of the bus admittance matrix is defined as

$$\underline{Y}_{k\ell} = G_{k\ell} + \mathrm{j}B_{k\ell} \tag{2.11}$$

where $G_{k\ell}$ is the conductance and $B_{k\ell}$ is the susceptance of the branch connecting nodes k and ℓ. The active and reactive power mismatch at node k is

$$\mathrm{Re}(\underline{F}_k) = P_k(V_k) - V_k \sum_{\substack{\ell=1\\ \ell\neq k}}^{n} V_\ell (G_{k\ell}\cos\delta_{k\ell} + B_{k\ell}\sin\delta_{k\ell}) \tag{2.12a}$$

$$\mathrm{Im}(\underline{F}_k) = Q_k(V_k) - V_k \sum_{\substack{\ell=1\\ \ell\neq k}}^{n} V_\ell (G_{k\ell}\sin\delta_{k\ell} - B_{k\ell}\cos\delta_{k\ell}). \tag{2.12b}$$

With this, the vector of all power mismatches is

$$\boldsymbol{F}(\boldsymbol{x}) = \big(\mathrm{Re}(\underline{F}_1), ..., \mathrm{Re}(\underline{F}_{n-1}), \mathrm{Im}(\underline{F}_1), ..., \mathrm{Im}(\underline{F}_{n-1})\big)^{\mathrm{T}} \tag{2.13}$$

where $\boldsymbol{F}(\boldsymbol{x}) \in \mathbb{R}^{2n-2}$. The goal of a power flow calculation is to find the bus voltage magnitudes and angles such that the system of nonlinear power mismatch equations becomes zero. These equations can be written in matrix form as

$$\boldsymbol{F}(\boldsymbol{x}) = \boldsymbol{0}. \tag{2.14}$$

If the nonlinear equation (2.14) is well conditioned, it can be solved by Newton's method. The system is linearized at point $\boldsymbol{x}^\nu$:

$$\boldsymbol{0} = \boldsymbol{F}(\boldsymbol{x}^\nu) + \boldsymbol{J}^\nu \Delta\boldsymbol{x}^{\nu+1} \tag{2.15}$$

where the superscript ν denotes the present iteration counter of Newton's method. $\boldsymbol{J}^\nu \in \mathbb{R}^{(n-1)\times(n-1)}$ is the Jacobian of $\boldsymbol{F}$ at point $\boldsymbol{x}^\nu$. The change of the state vector is

$$\Delta\boldsymbol{x}^{\nu+1} = \boldsymbol{x}^{\nu+1} - \boldsymbol{x}^\nu. \tag{2.16}$$

After the linear problem (2.15) is solved, the next approximation point is calculated by

$$\boldsymbol{x}^{\nu+1} = \boldsymbol{x}^{\nu} + \Delta\boldsymbol{x}^{\nu+1}. \tag{2.17}$$

This process is repeated iteratively until the maximum change of the state vector is below the power flow threshold $\varepsilon_{\mathrm{PF}}$:

$$\max|\Delta\boldsymbol{x}^{\nu+1}| < \varepsilon_{\mathrm{PF}}. \tag{2.18}$$

A value of $\varepsilon_{\mathrm{PF}} = 10^{-5}$ pu is usually sufficient for power system applications and also chosen in this work.

2.4 Integration into the power flow

In Section 2.4.1 the *external algorithm* is explained. It is the present state-of-the-art method for considering voltage dependent power injections in a power flow calculation. Section 2.4.2 presents the proposed novel *internal algorithm*. Figures 2.4 and 2.5 show the details of the implementation of both algorithms.

2.4.1 External algorithm

The *external algorithm*, as used in, e.g., [25, 26, 27], represents the present state-of-the-art to obtain static operation points in an electric grid under the presence of DGs with voltage dependent power injections. To compare the *external* and *internal algorithm*, it is beneficial to look at the *external algorithm* in some more detail. The main idea is to sequentially perform a power flow and to update the injected active and reactive powers according to the voltage characteristics of the DGs until the bus voltages converge. Details of the implementation are shown in Fig. 2.4. The prescript (i) denotes the iteration counter of the external loop, which represents the number of power flows. This avoids confusion with the index ν, which will later denote the counter of the Newton iteration of the *internal algorithm*. For example, ${}^{(i)}P_k$ is the active power injection at bus k during the (i)-th external iteration.

Initially, flat start conditions are chosen, thus the bus voltage magnitudes are set to 1 and the bus voltage angles are set to 0 (line 3 of Fig. 2.4). The active and reactive power injections of all DGs are initially calculated by using the voltage characteristics (2.3) divided by a filter value ζ (line 4-7). This avoids large overshoots of the voltages in the first power flow iteration. In practical applications, filter values between 3 and 5 result in a good convergence of the power flow. The higher the filter value the more likely the *external algorithm* is to converge. On the other hand, the computational time increases with higher filter values. Thus, the filter value has to be selected manually and adjusted if convergence is not reached. Each power flow is initialized with the previous power flow result (line 10). During the power flow the linear problem (2.15) is set up without considering the voltage dependency of the injected powers of the DGs. The DGs are only present at buses $1, ..., m$. The other buses are static. Therefore, an iteration across all DGs is started (line 11). The bus voltages are used to update the injected powers of the DGs (lines 12-13). A filter ζ

is applied (lines 14-15). The external loop is repeated until the maximum change of the bus voltages and angles is below a threshold $\varepsilon_{\text{external}}$ (line 17).

The overall power flow problem is nonlinear and convergence cannot be guaranteed in all cases. Some power flow problems without a solution exist. For example this is the case when the system is in a point of voltage collapse [36].

To gain more insights into the necessity of the filter it is useful to assume an example grid with a noticeable amount of DGs with voltage dependent active power injections. Normally, the power flow calculation starts with the full accessible active power injection of all DGs. That would be the case if lines 4-7 were not included in the algorithm. However, a power flow calculation in which all DGs inject their full active power often leads to very high bus voltages. These numerical voltage overshoots can be avoided if the injected powers of the DGs are not at 100 % during the first power flow. This is implemented by line 4-7, where the active and reactive powers are set to a value which is the injected active and reactive power, according to the $P(V)$ and $Q(V)$ characteristic, divided by the filter value. Let us further assume that the bus voltages computed by the first power flow calculation ($i = 1$) are very low because of the presence of the initial filter (line 4-7). In this case, the $P(V)$ characteristics in line 12 would result in using 100 % of the injected power in the next power flow calculation ($i = 2$). However, using the full active power might lead to very high bus voltages. This will result in a substantial reduction of injected active power in the subsequent power flow ($i = 3$), which will then show again high bus voltages and the cycle will start over again. This is denoted as numerical oscillation. The oscillation affects the voltages, the currents and the injected powers.

```
 1: procedure External Algorithm
 2:     $i = 0$
 3:     ${}^{(i)}\boldsymbol{x} = (1, ..., 1, 0, ..., 0)^{\mathrm{T}}$
 4:     for all $k \in \{1, ..., m\}$ do
 5:         ${}^{(i)}P_k = \frac{f_{\mathrm{P}k}({}^{(i)}V_k)}{\zeta}$
 6:         ${}^{(i)}Q_k = \frac{f_{\mathrm{Q}k}({}^{(i)}V_k)}{\zeta}$
 7:     end for
 8:     repeat
 9:         $i = i + 1$
10:         ${}^{(i-1)}\boldsymbol{x} \rightarrow \text{Power Flow} \rightarrow {}^{(i)}\boldsymbol{x}$
11:         for all $k \in \{1, ..., m\}$ do
12:             ${}^{(i)}P_k = f_{\mathrm{P}k}({}^{(i)}V_k)$
13:             ${}^{(i)}Q_k = f_{\mathrm{Q}k}({}^{(i)}V_k)$
14:             ${}^{(i)}P_k = {}^{(i-1)}P_k + \frac{{}^{(i)}P_k - {}^{(i-1)}P_k}{\zeta}$
15:             ${}^{(i)}Q_k = {}^{(i-1)}Q_k + \frac{{}^{(i)}Q_k - {}^{(i-1)}Q_k}{\zeta}$
16:         end for
17:     until $\max|{}^{(i)}\boldsymbol{x} - {}^{(i-1)}\boldsymbol{x}| < \varepsilon_{\text{external}}$
18: end procedure
```

Figure 2.4: Description of the external algorithm.

2.4.2 Internal algorithm

In this section, it is shown how to include the $Q(V)$ and $P(V)$ characteristics directly into the Newton power flow algorithm. During each Newton iteration ν the injected power into bus $k \in \{1, ..., m\}$ is updated according to

$$P_k^\nu = f_{\mathrm{P}k}(V_k^\nu) \tag{2.19a}$$

$$Q_k^\nu = f_{\mathrm{Q}k}(V_k^\nu). \tag{2.19b}$$

As can be seen in (2.8), the power mismatch consists of two voltage dependent terms, namely the injected powers $\underline{S}_k$ and the sum of the branch power flows $\sum_{\ell=1,\,\ell\neq k}^{n} \underline{S}_{k\ell}$. Therefore, the overall Jacobian is a linear combination of the Jacobians of these two terms and can be written as

$$\boldsymbol{J}^\nu = \boldsymbol{J}_{\mathrm{a}}^\nu + \boldsymbol{J}_{\mathrm{b}}^\nu. \tag{2.20}$$

$\boldsymbol{J}_{\mathrm{a}}$ is the Jacobian of the sum of the branch power flows $\underline{S}_{k\ell}$. Its construction can be found in, e.g., [35]. $\boldsymbol{J}_{\mathrm{b}}$ is the Jacobian of the voltage dependent power injection characteristics of the injected powers $\underline{S}_k$. If - besides DGs with voltage dependent power injection - no other voltage dependent loads are present, $\boldsymbol{J}_{\mathrm{b}}$ only exists for the *internal algorithm* and is zero in case of the *external algorithm.* As the injected powers are voltage dependent, the Jacobian $\boldsymbol{J}_{\mathrm{b}}$ may contain nonzero entries. It contains the derivatives of the voltage characteristics:

$$\boldsymbol{J}_{\mathrm{b}}^\nu = \begin{pmatrix} \frac{\partial \boldsymbol{P}}{\partial \boldsymbol{V}} & \frac{\partial \boldsymbol{P}}{\partial \boldsymbol{\delta}} \\ \frac{\partial \boldsymbol{Q}}{\partial \boldsymbol{V}} & \frac{\partial \boldsymbol{Q}}{\partial \boldsymbol{\delta}} \end{pmatrix} = \begin{pmatrix} \boldsymbol{J}_{\mathrm{b}11} & \boldsymbol{J}_{\mathrm{b}12} \\ \boldsymbol{J}_{\mathrm{b}21} & \boldsymbol{J}_{\mathrm{b}22} \end{pmatrix} \tag{2.21}$$

where $\boldsymbol{J}_{\mathrm{b}11}, \boldsymbol{J}_{\mathrm{b}12}, \boldsymbol{J}_{\mathrm{b}21}, \boldsymbol{J}_{\mathrm{b}22} \in \mathbb{R}^{(n-1)\times(n-1)}$. The active and reactive power vectors are described by

$$\boldsymbol{P} = (P_1^\nu, ..., P_{n-1}^\nu)^{\mathrm{T}} \tag{2.22a}$$

$$\boldsymbol{Q} = (Q_1^\nu, ..., Q_{n-1}^\nu)^{\mathrm{T}} \tag{2.22b}$$

where $\boldsymbol{P}, \boldsymbol{Q} \in \mathbb{R}^{n-1}$. Let $g_{\mathrm{P}k}(V_k^\nu)$ and $g_{\mathrm{Q}k}(V_k^\nu)$ be the derivative of the active and reactive power characteristics of the DG connected to bus k according to (2.5), which is a smoothing function of (2.2). The injected active and reactive powers do not depend on the bus voltage angle. It is

$$\boldsymbol{J}_{\mathrm{b}11} = \left(\begin{array}{ccc|c} g_{\mathrm{P}1}(V_1^\nu) & & & \\ & \ddots & & 0 \\ & & g_{\mathrm{P}m}(V_m^\nu) & \\ \hline & 0 & & 0 \end{array}\right) \tag{2.23a}$$

$$\boldsymbol{J}_{\mathrm{b}21} = \left(\begin{array}{ccc|c} g_{\mathrm{Q}1}(V_1^\nu) & & & \\ & \ddots & & 0 \\ & & g_{\mathrm{Q}m}(V_m^\nu) & \\ \hline & 0 & & 0 \end{array}\right) \tag{2.23b}$$

$$\boldsymbol{J}_{\mathrm{b}12} = \boldsymbol{J}_{\mathrm{b}22} = \mathbf{0}. \tag{2.23c}$$

If only $P(V)$ (or $Q(V)$) injections are present, the matrix $\boldsymbol{J}_{\mathrm{b}21}$ (or $\boldsymbol{J}_{\mathrm{b}11}$) becomes zero. If both injections are active, both matrices can have nonzero entries.

According to Section 2.6.1, the nonlinear voltage characteristic can lead to ill-conditioned cases. An explanation of ill-conditioned power flow cases is presented in [20]. For solving those cases robust techniques of the basic Newton's method have been introduced in literature, e.g., [37, 38, 39]. These techniques are mainly based on modifying (2.15). In this, a modified (damped) Newton method, described as bisection method in [20], is used. Following the nomenclature of [20], this type of modified (damped) Newton method will be called bisection Newton method in this work. After the new state vector $\boldsymbol{x}^{\nu+1}$ is calculated, it is tested if the power mismatch $\boldsymbol{F}(\boldsymbol{x}^{\nu+1})$ decreased. If not, then the change in the state vector $\Delta\boldsymbol{x}^{\nu}$ is reduced by a factor α. During the first iteration $\alpha = 1$ is assumed. For an unsolvable case, α will converge towards zero, thus a minimum value of α has to be defined.

The bisection Newton method is similar to the more sophisticated damped Newton-Raphson method presented in [40] which works with a damping multiplier that corresponds to the variable α used in this work. The difference is, that in the damped Newton-Raphson method an optimum value is found for the damping multiplier by approximating the power mismatch function with a quadratic function. This method is suitable for obtaining power flow results in case that the conventional Newton-Raphson is not converging. This is done by obtaining the minimum of the power mismatch. In the modified method used in this work, α is simply decreased (divided by 2) during each iteration if the power mismatch function does not decrease.

Details of the implementation of the *internal algorithm* are shown in Fig. 2.5. The Newton iteration counter ν is initially set to zero (line 2 of Fig. 2.5) and flat start conditions are chosen (line 3). At the beginning of each Newton iteration the injected powers are updated according to the voltage characteristics of the DGs (2.19) (lines 5-8). The Jacobian and the power mismatch function are updated (lines 9-10). In the next step, the modified Newton method is applied (lines 11-16) and the internal iteration counter is increased (line 17). This process is repeated until the change in bus voltages is below the threshold $\varepsilon_{\mathrm{internal}}$ (line 18).

```
procedure Internal Algorithm
    $\nu = 0$
    $\boldsymbol{x}^{\nu} = (1, ..., 1, 0, ..., 0)^{\mathrm{T}}$
    repeat
        for all $k \in \{1, ...m\}$ do
            $P_k^{\nu} = f_{\mathrm{P}k}(V_k^{\nu})$
            $Q_k^{\nu} = f_{\mathrm{Q}k}(V_k^{\nu})$
        end for
        Update Jacobian $\boldsymbol{J}^{\nu}$
        Update $\boldsymbol{F}(\boldsymbol{x}^{\nu})$
        $\alpha = 2$
        repeat
            $\alpha = \alpha/2$
            $\Delta\boldsymbol{x}^{\nu+1} = -\alpha\,(\boldsymbol{J}^{\nu})^{-1}\,\boldsymbol{F}(\boldsymbol{x}^{\nu})$
            $\boldsymbol{x}^{\nu+1} = \boldsymbol{x}^{\nu} + \Delta\boldsymbol{x}^{\nu+1}$
        until $\max|\boldsymbol{F}(\boldsymbol{x}^{\nu+1})| \leq \max|\boldsymbol{F}(\boldsymbol{x}^{\nu})| \vee \alpha < 10^{-2}$
        $\nu = \nu + 1$
    until $\max|\Delta\boldsymbol{x}^{\nu+1}| < \varepsilon_{\mathrm{internal}}$
end procedure
```

Figure 2.5: Description of the internal algorithm.

2.5 MATLAB power flow tool

To investigate the proposed *internal algorithm*, a conventional Newton power flow algorithm without any voltage dependent power injection has been implemented in MATLAB [41]. This implementation of the conventional Newton power flow was vaildated against MATPOWER [42]. Subsequently, the *internal* as well as the *external algorithm* were implemented on top of this basic power flow routine. The resulting MATLAB tool is capable of conduction power flow calculations with or without voltage dependent active or reactive power injection.

2.5.1 Data format

The data format of the power flow tool is based on the MATPOWER data format and uses the static data entries of the data structure of the RMS-framework displayed in Table 3.3. The data for each power flow case is stored in a MATLAB struct with fields for the branch, bus and generator data. On top of that, the parametrization of components with voltage dependent active and reactive power injections is done via an additional field called *PQULoad*. All fields of the struct are shown in Table 2.2.

The description of the data for *PQULoad*, which is given in matrix form, can be seen in Table 2.3. It contains the bus number of the DG and a flag which can be used to turn the DG on and off. Furthermore, it contains the active power injection in normal power flow mode, which is needed for cases in which the DG is simulated without voltage dependent active or reactive power injections. In rows 4-10 the $P(V)$ characteristic is stored and in rows 11-17 the $Q(V)$ characteristic is stored.

Table 2.2: Input data for power flow tool. The data format corresponds to the static portion of the RMS-framework data format described in Table 3.3.

Name	Type	Description
baseMVA	int	Base value for power
Bus	Matrix	Grid buses with loads
Branch	Matrix	List of grid impedances
Gen	Matrix	Generator data
PQULoad	Matrix	List of components with voltage dependent active and reactive power injection

Table 2.3: Field *PQULoad*.

Row	Conents
1	Bus number
2	On or off
3	Active power injection in normal power flow mode
4-10	$P(V)$ characteristics: $[V_1 V_2 V_3 V_1, y_1, y_2, y_3]$ according to (2.1)
11-17	$Q(V)$ characteristics: $[V_1 V_2 V_3 V_1, y_1, y_2, y_3]$ according to (2.1).

2.5.2 Program execution

After the data file is established properly, the MATLAB power flow tool can be executed. The execution call is

$$[V,\text{ res}] = \text{UkPF(mpc, mode, filter, robust)}$$

The input variables are the data mpc file, the calculation mode, the filter value for the external algorithm and a flag, called robust, that turns the robust Newton algorithm on or off. The function returns the bus voltages as well as some additional information stored in the variable res. This information contains, for example, the amount of iterations the algorithms needed to converge or the power mismatch values for each Newton iteration. The power flow tool can be executed in eight different modes. An overview of each mode is given in Table 2.4. In mode 0 the power flow is executed as if the distributed generators stored in the field *PQULoad* were not present in the system. This mode in beneficial if the user wants to obtain a quick overview of the bus voltages without DG infeed. In mode 1, all DGs are considered with their active power infeed stored in third row of the filed *PQULoad* (see Table 2.3). In this mode, the reactive power infeed is always set to zero. In modes 2, 3 and 4 the voltage dependent power injections are considered via the internal algorithm and in modes 5,6 and 7 the voltage dependent power injections are considered via the external algorithm.

Table 2.4: Execution modes of the power flow tool.

Mode	Meaning
0	Basic Power Flow without considering PQLoad
1	Basic Power Flow under consideration of PQLoad
2	Internal algorithm; $Q(V)$ control is active
3	Internal algorithm; $P(V)$ control is active
4	Internal algorithm; $P(V)$ and $Q(V)$ control is active
5	External algorithm; $Q(V)$ control is active
6	External algorithm; $P(V)$ control is active
7	External algorithm; $P(V)$ and $Q(V)$ control is active

2.6 Test cases

To conduct the case studies shown in this section the power flow tool described in Section 2.5 was used. All simulations were performed on an Intel i7-3520M 2.90 GHz processor with 16 GB RAM and on a Windows 7 operating system. The voltage characteristics used in the case studies are based on values used by distribution system operators in practical settings.

2.6.1 Two-bus system

A two-bus system, as shown in Fig. 2.6, is used to compare the convergence properties of the *internal* and the *external algorithm*. It consists of a DG connected to an infinite bus via a resistor and an inductor. Furthermore, the simulation results are validated in the laboratory.

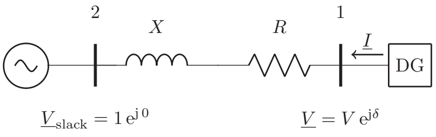
2
X
R
1
$\underline{I}$
DG
$\underline{V}_{\text{slack}} = 1\,\mathrm{e}^{\mathrm{j}\,0}$
$\underline{V} = V\,\mathrm{e}^{\mathrm{j}\delta}$

Figure 2.6: Two-bus system with a distributed generator connected to bus 1.

Convergence properties

The parameters of the line and the $P(V)$ and $Q(V)$ characteristics are given in Tables 2.5 and 2.6. The configuration for the characteristics represent realistic values also used in distribution grids. The operating point of the DG depends on the power injection method and can be found in Table 2.7. Both *internal* and *external algorithm* converge to the same values, therefore only one power flow result is shown in Table 2.7. The voltage at bus 1 is higher than the voltage at bus 2 (slack bus) for all injection strategies. This is due to the fact that in all cases active power is fed into the grid and current is flowing from bus 1 to bus 2.

Table 2.5: Parameters of the simulated two-bus system

Description	Symbol	Value	Unit
Base apparent power	S_{base}	100	[kVA]
Base voltage	V_{base}	230	[V]
Line resistance	R	0.383	[pu]
Line reactance	X	0.190	[pu]

Table 2.6: Voltage characteristic of the simulated two-bus system

Injection method	$[V_1, V_2, V_3 V_4]$ [pu]	$[y_1, y_2, y_3]$ [pu]
$P(V)$	$[1.08, 1.08, 1.08, 1.09]$	$[0.35, 0.35, 0.20]$
$Q(V)$	$[0.93, 0.97, 1.03, 1.07]$	$[0.18, 0.0, -0.18]$

Table 2.7: Power flow results of the simulated two-bus system

Injection strategy	Voltage magnitude [pu]	Voltage angle [degree]	Active power [pu]	Reactive power [pu]
None	1.118	3.392	0.35	0.00
$Q(V)$	1.085	7.161	0.35	-0.18
$P(V)$	1.087	2.477	0.25	0.00
$P(V)$ & $Q(V)$	1.081	7.062	0.34	- 0.18

The injection strategy ”None” means, that all available active power (in this case 35 kW) is fed into the grid by the DG and that there is no voltage dependent active or reactive power injection. During the injection strategy Q(V) the DG is feeding reactive power into bus 1 in order to decrease the voltage. During injection strategy $P(V)$ the DG reduces its active power injection based on the voltage, again, in order to reduce the voltage at bus 1. In the strategy $P(V)$ & $Q(V)$ the DG feeds in reactive power and reduces its active power in order to reduce the voltage at bus 1. Active and reactive power injection takes place depending on the voltage at bus 1 according to the voltage characteristic given in Table 2.6.

A more detailed investigation of the convergence behavior of the *external* and *internal algorithm* is presented for the case of $P(V)$ injection. It is assumed that no reactive power is injected. Fig. 2.7 shows the maximum power mismatch and the voltage magnitude after each iteration of the *external algorithm* for three different filter values. For a filter value of $\zeta = 2$ the voltage magnitude shows an oscillatory behavior and does not converge. The reason is that the injected active power keeps on jumping from its highest (y_1) to its lowest value (y_3). A more detailed explanation and a plot of the injected power can be found in [27]. For $\zeta = 3$ and $\zeta = 4$ the voltage magnitude converge towards the same final value and thus both power mismatches converge towards zero. For $\zeta = 3$ the overall convergence speed is lower and the numerical oscillations are higher than for $\zeta = 4$.

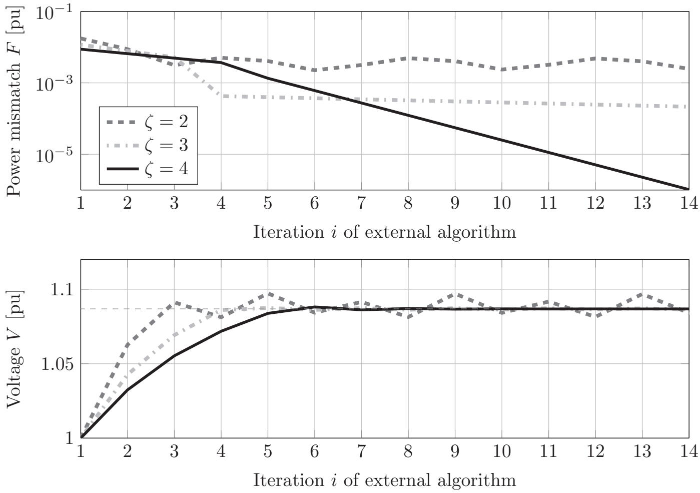

Figure 2.7: Active power mismatch (top) and bus voltage magnitude (bottom) against the power flow iteration i of the external algorithm with $P(V)$ injection for different filter values ζ for the simulated two-bus system.

The convergence behavior of the *internal algorithm* is shown in Fig. 2.8 for both Newton's method and bisection Newton's method. The maximum power mismatch (top) and the voltage magnitude (bottom) are shown for each Newton iteration ν. It can be observed that the bisection method converges and the normal Newton method without bisection algorithm does not converge. It has to be pointed out that the power mismatch is in the order of 10^{-6} after eight Newton iterations. For reaching the same level of power mismatch the *external algorithm* requires about 14 external iterations which corresponds to 30 Newton iterations. Thus, the *internal algorithm* required much less Newton iterations than the *external algorithm* (8 instead of 30) in this case. Furthermore, the filter value needs to be set in the *external algorithm,* which is a crucial disadvantage that our proposed *internal algorithm* does not suffer from. The speedup in terms of actual computational time is not very significant

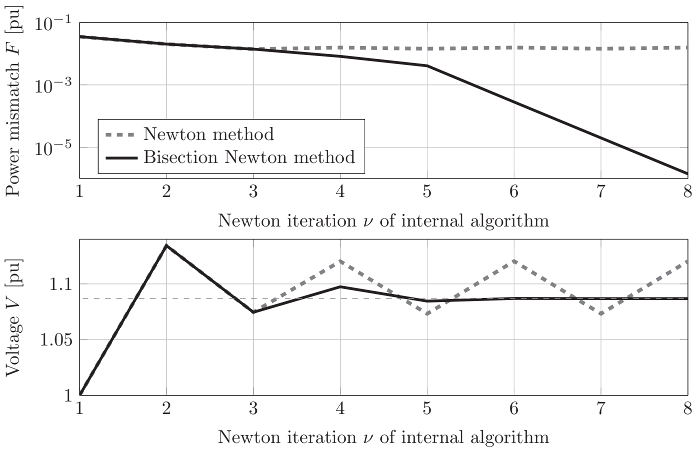

Figure 2.8: Active power mismatch (top) and bus voltage magnitude (bottom) for the internal algorithm of the Newton method and the bisection Newton method for the simulated two-bus system.

for the two-bus system. The *external algorithm* needs about 13 ms and the *internal algorithm* about 5 ms of computational time. The reason is, that for the two-bus system, the Newton step is actually less time consuming than the other parts of the algorithm like, for example, the initialization. As the matrices involved are only of size [2 × 2] for a two-bus system, the benefit in computational time becomes more evident in case of larger grids. This is shown in Section 2.6.2.

Inverse nose curve

In order to illustrate the ill-conditioned power mismatch function for the two-bus system, the inverse nose curve is needed. The inverse nose curve can be calculated based on the single phase complex power consumption at bus 1 in Fig. 2.6. It is

$$\underline{S} = P + \mathrm{j}Q = \underline{V}\,\underline{I}^*. \tag{2.24}$$

The current can be calculated as $\underline{I} = (\underline{V} - \underline{V}_{\text{slack}})\,\underline{Y} = (\underline{V} - 1)\,\underline{Y}$ with $\underline{Y} = (R + \mathrm{j}X)^{-1} = G + \mathrm{j}B$ being the line admittance. The capacitance of the line is neglected. Taking real and imaginary part of (2.24) results in active and reactive powers. After reordering:

$$P - GV^2 = -GV\cos(\delta) - BV\sin(\delta) \tag{2.25a}$$

$$Q + BV^2 = BV\cos(\delta) - GV\sin(\delta). \tag{2.25b}$$

Taking the square of (2.25a) and (2.25b) results in

$$P^2 - 2PGV^2 + G^2V^4 = G^2V^2\cos^2(\delta) + 2GBV^2\cos(\delta)\sin(\delta) + B^2V^2\sin^2(\delta) \tag{2.26a}$$

$$Q^2 + 2QBV^2 + B^2V^4 = B^2V^2\cos^2(\delta) - 2BGV^2\cos(\delta)\sin(\delta) + G^2V^2\sin^2(\delta). \tag{2.26b}$$

Summing them up removes the angle dependency:

$$P^2 - 2PGV^2 + G^2V^4 + Q^2 + 2QBV^2 + B^2V^4 = G^2V^2 + B^2V^2 \tag{2.27}$$

Rearranging leads to a quadratic equation. Solving it for the active power finally leads to the inverse nose curve

$$P(V) = GV^2 \pm \sqrt{(G^2 + B^2 - 2BQ)V^2 - B^2V^4 - Q^2}, \tag{2.28}$$

The nose curve, which was just derived describes the active power injection depending on the voltage magnitude V. The complete nose curve according to (2.28), for zero injected reactive power, is shown in Fig. 2.9. The solid line represents the physical correct solution of (2.28) with a positive sign in front of the square root. The dashed line is the non-physical solution that is present due to the solution with the negative sign in front of the square root of (2.28).

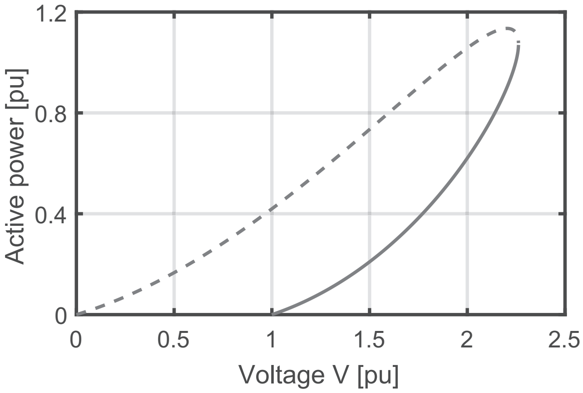

Figure 2.9: Complete inverse nose curve according to 2.28.

Ill-conditioned power mismatch

The operating point of the two-bus system is the intersection between the nose curve and the $P(V)$ characteristics. Both curves are plotted in Fig. 2.10. It can be seen that the intersection coincides with the value in Table 2.7 for the injection strategy $P(V)$. The power mismatch function is the difference between the inverse nose curve and the $P(V)$ characteristic and is shown in Fig. 2.10 (bottom). It can be seen that the power mismatch function is ill-conditioned. The reason is the piecewise linear definition of the $P(V)$ characteristic and its steep decrease relative to the inverse

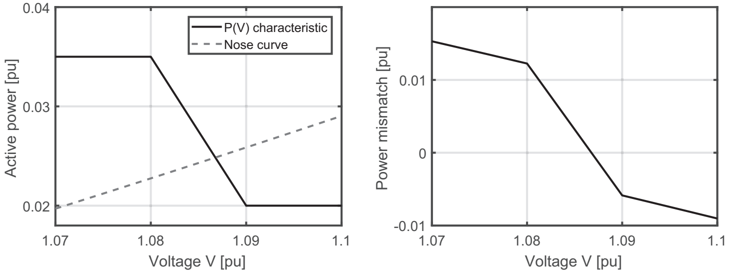

Figure 2.10: Inverse nose curve and $P(V)$ characteristic (left) and resulting active power mismatch function (right) for the simulated two-bus system.

nose curve in the area of 1.08 pu $< V <$ 1.09 pu. Such a system can only be solved by the conventional Newton method if the initial value for the voltage V is located between power flow cases can be found in, e.g., [20]. To guarantee convergence of the *internal algorithm* in those ill-conditioned cases the bisection method as explained in Section 2.4.2 is used.

The iterative process of the *internal* and *external algorithm* is now addressed in detail. Table 2.8 shows the interim results for the *external algorithm* for a filter value of $\zeta = 4$. Note that ${}^{(i)}P_1$ is the injected power of the DG into bus 1. During initialization ($i = 0$) the injected power of the DG is set to ${}^{(0)}P_1 = 0.35/4 = 0.087$ pu. The first power flow calculation ($i = 1$) results in a voltage of $1.0324\angle 0.918°$. With this voltage the new injected power is $f_{P1}(1.0324) = 0.35$. The application of the filter results in ${}^{(1)}P_1 = 0.087 + (0.35 - 0.087)/4 = 0.153$ pu. This injected power leads to a voltage of $1.0553\angle 1.572°$ in the second iteration ($i = 2$). The process is repeated until a steady state is reached in the 12th external iteration.

Table 2.9 shows the iteration results of the *internal algorithm*. P_1^ν is the injected power of the DG into bus 1 and $g_{\mathrm{P1}}(V_1^\nu)$ is the slope of the $P(V)$ characteristic at V_1^ν. During initialization ($\nu = 0$) the injected power is set to $P_1^0 = 0.350$ which

Table 2.8: Interim results for each external iteration i of the *external algorithm* for $P(V)$ characteristic of the simulated 2-bus system

i	V_1^i [pu]	${}^{(i)}P_1$ [pu]	i	V_1^i [pu]	${}^{(i)}P_1$ [pu]
0	$1\angle 0°$	0.087	7	$1.0870\angle 2.485°$	0.248
1	$1.0324\angle 0.918°$	0.153	8	$1.0866\angle 2.474°$	0.249
2	$1.0553\angle 1.572°$	0.202	9	$1.0868\angle 2.479°$	0.248
3	$1.0718\angle 2.045°$	0.239	10	$1.0867\angle 2.477°$	0.249
4	$1.0838\angle 2.392°$	0.253	11	$1.0868\angle 2.478°$	0.248
5	$1.0881\angle 2.516°$	0.247	12	$1.0868\angle 2.477°$	0.249
6	$1.0862\angle 2.4609°$	0.249			

Table 2.9: Interim results for each internal iteration ν of the *internal algorithm* for $P(V)$ characteristic of the simulated 2-bus system

ν	V_1^ν [pu]	P_1^ν [pu]	$g_{\mathrm{P1}}(V_1^\nu)$ [pu]	ν	V_1^ν	P_1^ν	$g_{\mathrm{P1}}(V_1^\nu)$
0	$1\angle 0°$	0.0350	0.0	4	$1.0845\angle 2.407°$	0.0282	-1.50
1	$1.1342\angle 3.791°$	0.0200	0.0	5	$1.0869\angle 2.482°$	0.0246	-1.50
2	$1.0746\angle 2.108°$	0.0350	0.0	6	$1.0868\angle 2.477°$	0.0249	-1.50
3	$1.0974\angle 2.774°$	0.0200	0.0				

is the total power accessible. In the first Newton iteration ($\nu = 1$), the resulting voltage is $1.1342\angle 3.791°$ which is on the far right of the $P(V)$ characteristic and thus the injected power is $P_1^1 = 0.200$. During the next Newton iteration ($\nu = 2$) the voltage drops again to $1.0746\angle 2.108°$ which is left of the point V_3 of the $P(V)$ characteristic according to Table 2.6. Thus the injected power is increased to its maximum value of $P_1^2 = 0.35$. During the third iteration ($\nu = 3$) the voltage is $1.0974\angle 2.774°$ and thus the injected power is set to its minimum value of $P_3^\nu = 0.2$. During these first 3 iterations, the Jacobian $\boldsymbol{J}_b$ is always zero because the voltage was not on the slope of the $P(V)$ characteristic. In the fourth iteration ($\nu = 4$) the voltage is $1.0845\angle 2.407°$ and for the first time, the voltage is such that the operating point is on the slope of the $P(V)$ characteristic. Therefore the injected power is set to $P_1^4 = 0.282$. The Jacobian is thus nonzero. It is

$$\boldsymbol{J}_{\mathrm{b11}} = \left(\begin{array}{c|c} -1.5 & 0 \\ \hline 0 & 0 \end{array}\right), \boldsymbol{J}_{\mathrm{b21}} = \left(\begin{array}{c|c} 0 & 0 \\ \hline 0 & 0 \end{array}\right). \tag{2.29}$$

Finally, the Jacobian due to the DG is

$$\boldsymbol{J}_{\mathrm{b}}^\nu = \left(\begin{array}{cc|cc} -1.5 & 0 & 0 & 0 \\ 0 & 0 & 0 & 0 \\ \hline 0 & 0 & 0 & 0 \\ 0 & 0 & 0 & 0 \end{array}\right). \tag{2.30}$$

The Jacobian $\boldsymbol{J}_{\mathrm{a}}$ of the system is computed as usually during a power flow algorithm. The process is repeated until sufficient accuracy is reached.

Experimental Validation

The algorithm was tested in an experimental setup of the two-bus system as shown in Fig. 2.11. More specific it was validated that the measured voltage at an inverter with voltage dependent power injection corresponds with the voltage that is calculated by the internal algorithm.

For the experiment, a DC source which mimics the properties of a string of solar panels was connected to a 4.6 kW SMA Sunny Boy inverter. The inverter was connected to an AMETEK grid emulator via a cable. The resistance and inductance of the cable was measured as $R = 0.41\,\Omega$ and $L = 672\,\mu$H.

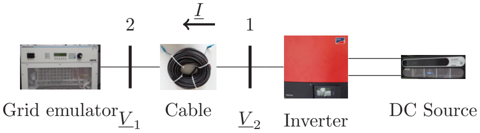

Figure 2.11: Experimental setup of the two-bus system.

The voltage $\underline{V}_1$ was varied. Due to this variation, the $Q(V)$ and $P(V)$ injection of the inverter was activated. The measured $Q(V)$ and $P(V)$ characteristics of the inverter are shown in Fig. 2.12. Fig. 2.13 shows the measurement values and the simulated values of V_1 and V_2. It can be seen that the measured and the simulated values coincide. It is crucial to investigate new inverter capabilities like voltage dependent active and reactive power injection also in a practical lab setup.

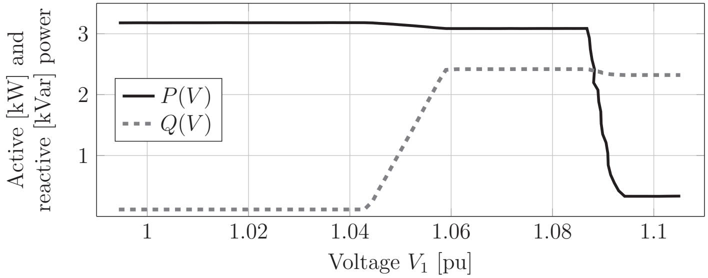

Figure 2.12: Measured $Q(V)$ and $P(V)$ characteristics of the inverter.

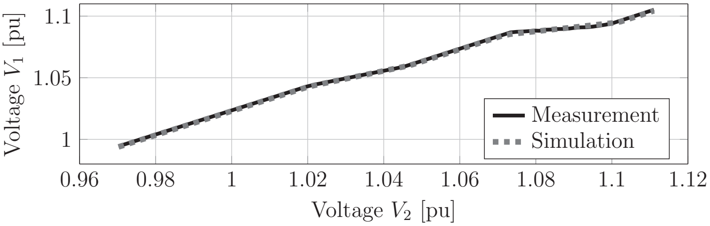

Figure 2.13: Voltage at the point of common coupling at bus 1 against grid voltage at bus 2 for $P(V)$ and $Q(V)$ injection strategies. The base voltage is $230\,V$.

2.6.2 Performance Analysis

A performance analysis of the *internal* and *external algorithm* was done with two test systems.

The first test system is the IEEE 118-bus system which represents a portion of the American Electric Power System. The data of this test system is given in [43]. In this system, 54 synchronous generators with power and voltage control are present. As the goal of the investigation is to test voltage dependent power injections with $P(V)$ and $Q(V)$ characteristics, all synchronous generators were removed and replaced with constant power injections. In the next step, 50 DGs with $P(V)$ and $Q(V)$ characteristics were placed randomly in the grid. The total nominal power of the DGs was chosen to be 10% of the total power of the original generators. This value was chosen in order to obtain significantly high voltages in the range of 1.03 to 1.1 pu, where the voltage characteristics of the DGs have an effect. The description of the voltage characteristics is given in Table 2.10. The table contains the $P(V)$ and $Q(V)$ characteristics for all generators where P_n is the nominal power of the DG and d as well as e are parameters that are specified for each case. By varying these parameters, different characteristics are obtained. The simulations were performed in two setups S1 and S2. In setup S1, all DGs were given the same $P(V)$ and $Q(V)$ characteristics. Specifically $P_n = 0.0875\,\text{pu}$, $d = 0$ and $e = 0$ is chosen. In setup S2 all characteristics are chosen differently in order to investigate the influence of different characteristics on the runtime. We have set $d = 0.02/50 \cdot (i - 1)$ and $e = 0.01/50 \cdot (25.5 - i)$ with $i = 1, ..., 50$ being the index of the DG.

Table 2.10: Voltage characteristics for the performance test of the IEEE 118-bus test system and the real German 234-bus grid.

Injection method	V_1 [pu]	V_2 [pu]	V_3 [pu]	V_4 [pu]	y_1 [pu]	y_2 [pu]	y_3 [pu]
$P(V)$	$1.08 - d$	$1.08 - d$	$1.08 - d$	$1.09 - d$	$P_n + e$	$P_n + e$	$(P_n + e) \cdot 0.2$
$Q(V)$	$0.92 - d$	$0.97 - d$	$1.03 - d$	$1.08 - d$	$(P_n + e) \cdot 0.5$	0.000	$-(P_n + e) \cdot 0.5$

The second test system is a real German 234-bus grid. In this system, 108 DGs with $P(V)$ and $Q(V)$ characteristics are included. Similar to the test with the IEEE 118-bus system, two setups S1 and S2 are investigated. For both setups it is set $P_n = 0.0153\,\text{pu}$. For setup S1, all generators were given the same characteristics, thus $d = 0$ and $e = 0$. For setup S2, different characteristics were selected for all DGs, specifically $d = 0.02/108 \cdot (i - 1)$ and $e = 0.01/108 \cdot (54.5 - i)$ with $i = 1, ..., 108$ being the index of the DG. The values chosen are similar to practical settings that are used by German distribution system operators.

Simulations of each setup where performed for 40 different random locations of DGs. For each setting, ten simulation runs were performed. The average values and variances of all simulation run times were calculated. The results for the complex bus voltages of the *internal* and *external algorithm* were compared to each other after each single power flow calculation. For each bus voltage, the absolute value of the complex voltage difference between *internal* and *external algorithm* was smaller than 10^{-4} pu. Thus, both algorithms converged to the same values. To obtain this, a filter value of $\zeta = 5$ was chosen for the external algorithm. The filter value was chosen such that it was the minimal value for which all simulations still converged. Lower filter values resulted in a significant amount of simulations that did not converge. Higher filter values only increased the computational time. Therefore, the chosen filter value was the best possible choice concerning computational speed and convergence. The results for the run time are displayed in Table 2.11. It shows the average computation time, the total number of Newton iterations and the number of power flows for each algorithm. For example in case of the IEEE 118-bus system the *external algorithm* requires an average number of 44 power flows to converge. This results in an average total number of 102 Newton iterations. This means that on average, a power flow calculation needed 102/44 = 2.3 iterations to converge. The *internal algorithm* needed only one power flow iteration which took an average of 6 Newton iterations. The advantage of the internal algorithm can be found in both the run time and the average total number of Newton iterations. The *internal algorithm* is between 8 and 14 times faster than the *external algorithm* and the *external algorithm* needs between 11 to 17 times more Newton iterations.

Table 2.11: Comparison of external and internal algorithm (average values and variances.

System	Algorithm	Time [ms]	Sum of Newton iterations	Number of Power flows
118 Bus	Ext.	132 ± 72	102 ± 11	44 ± 3
(S1)	Int.	9 ± 1	6 ± 1	1 ± 0
118 Bus	Ext.	136 ± 7	106 ± 58	45 ± 16
(S2)	Int.	10 ± 1	7 ± 2	1 ± 0
234 Bus	Ext.	169 ± 43	93 ± 1	40 ± 1
(S1)	Int.	19 ± 2	8 ± 1	1 ± 0
234 Bus	Ext.	165 ± 8	92 ± 1	41 ± 1
(S2)	Int.	18 ± 1	8 ± 1	1 ± 0

2.7 Conclusion

In this chapter, the *internal algorithm* was presented in which piecewise voltage characteristics of DGs are incorporated directly into the conventional Newton power flow. The *internal algorithm* was compared to the commonly used *external algorithm*. The comparison was done with respect to convergence properties for an ill-conditioned two-bus system and with respect to computational complexity for the IEEE 118-bus test system and for a real German 234-bus network. Furthermore, a laboratory experiment is performed where the voltage measurements of a real inverter with voltage dependent power injections was compared successfully with the results of the simulations with the *internal algorithm*.

It was demonstrated that the *internal algorithm* has major advantages over the *external algorithm*. First of all, the incorporation of the voltage characteristics into the power flow allows the integration of voltage dependent power injection with minimal effort in analyses where the Jacobion matrix is required. A further advantage is the improved robustness compared to the *external algorithm*. The filter ζ of the *external algorithm* needs to be tuned and it is a trade-off between speed and robustness. In case of the *internal algorithm*, ill-conditioned cases can be treated with robust power flow methods and no manual tuning is required. For this, the bisection Newton method was used. Another advantage is the improved computational efficiency. This allows significant speed-ups in cases where thousands of power flows have to be solved, e.g., in power system planning and operation.

With the *internal algorithm*, a broad range of voltage dependent power injections based on (2.1) can be included into the power flow. Future research could focus on implementing power injections of DGs into novel power flow approaches like the Holomorphic Embedding load-flow Method [44].

The efficient power flow routine described in this chapter is used for the initialization process of the RMS-framework presented in Chapter 3 of this thesis.

Chapter 3

Phasor-Framework

3.1 Introduction

Typically, time-domain simulations of power systems with hundreds of buses that are spanning a time range of up to several seconds or minutes are performed in phasor mode (also called phasor) fashion. In a phasor mode simulation the grid is represented with algebraic equations. Transients arising from the grid reactances are neglected. phasor simulations are usually applied to study the positive sequence of balanced systems [20]. Typical topics that can be investigated using phasor simulations are: frequency stability, low-voltage (LV) ride-through, transient stability, short-term voltage stability, long-term voltage stability, unintentional islanding or power system restoration.

In this chapter a phasor-framework is designed and implemented that closes an existing gap amongst state-of-the art simulation tools. The tool is developed on the basis of MATLAB [45] and Simulink [46] and uses the current injection method as a solution method [20, 47]. The chapter is structured as follows: In Section 3.2 a comparison between different phasor simulation tools is given. From this comparison, the gap that exists amoung state-of-the-art phasor simulation tools is deduced. In Section 3.4 an overview of the framework including its properties, data structure and workflow is given. In Section 3.5 and 3.6, the network and component model is described. In Section 3.7 the fault simulation and in Section 3.8 parameter variations are explained. In Section 3.9 a discussion on the developed phasor-framework is given and in Section 3.10 the chapter is concluded.

This chapter is partly based on the publication
D. Fetzer, G. Lammert, A. Ishchenko, L. Tabit, M.Braun,
A Flexible MATLAB/Simulink RMS-Framework for Electrical Power Systems Designed for Research and Education, ISGT 2018

3.2 Comparison of phasor based simulation tools

The goal of this section is to compare software tools for dynamic power system simulation and explain the gap that exists amoung these state-of-the-art tools.

A big challenge in power system simulation is the representation and implementation of both, grid algorithms and component models. For example the implementation of component models that comply to modern grid codes is challenging due to multiple states that the component can adopt. For instance, to model the reconnection process of a photovoltaic system, after disconnecting from the grid, four model states are needed: Normal operation, active power reduction, disconnected and reconnection. For more comprehensive models which, for example, also include, dynamic voltage support, more states have to be added. To adequately model different states of a component, a **state machine modeling approach** is useful [48].

Another important aspect in the model developing process is that the development engineer can focus on the implementation of the physical equations and keep software related issues to a minimum. This can be achieved by **block diagram modeling**. Block diagram modeling means that models do not have to be implemented in plain, written code but can be implemented using block diagrams which are visually easier to grasp. That means that the developer can focus on the implementation of the component models rather than on programming issues. The usage of block diagrams for model development is closely related to rapid prototyping [49], [50] of component models and their controls. All in all, rapid prototyping of component models is faster that to develop the models in pure code.

Therefore, the comparison of power system simulation tools is centered around the issue of component modeling and implementation.

Another important aspect is the amount of pre-implemented standard component models in a **comprehensive model database**. It simplifies the modeling and simulation a lot, if most of the standard models, like asynchronous machines, synchronous machines, excitation systems, governors, photovoltaic systems, wind generators and inverters are available, validated and ready to use.

Also, the distinction between black-box and **non-black-box tools** is essential. Non-black-box tools allow the user to see all implemented equations and the complete source code of both, the grid equations and component models.

Furthermore it is an important feature if a simulation tool is optimized for command line usage or not. If a tool is **focused on command line usage**, it is possible to run the software seamlessly via a command line interface and use scripting in a straight forward way. All of the compared tool offer scripting and command line usage in one or the other way. However, not all tools are really optimized for a command line usage. Especially commercial tools are more focused towards the usage through a graphical user interface (GUI) and the command line usage is only possible through a not very well documented application interface (API). The usage through a command line interface combined with an easy to read data model has the advantage that the simulations can be build up and conducted in a more flexible way.

Therefore, the simulation tools are compared with regard to the following aspects:

- Block diagram component modeling
- State machine component modeling
- Extensive model database
- Non-black-box tool
- Focused onto command line usage

From a birds eye perspective, tools for phasor simulation of electrical power systems can be divided into the following two groups:

- Commercial tools
- Non-commercial, open-source tools

Commercial tools are developed by dedicated companies and distributed against a usage charge. They are optimized for computational speed, efficiency and are well suited for standard, repetitive investigations such as transient stability analyses, short circuit calculation or eigenvalue evaluation [20]. On top of that, commercial tools often feature various amounts of accurate and validated component models that are ready to use. Existing commercial power system simulation tools are, for example, DIgSILENT PowerFactory®[18], Siemens PSS®E [51], PowerWorld Simulator [52] and GE PSLF [53].

On the other hand, non-commercial tools are often available through an open-source license and developed and maintained by research groups or individuals. They are often non-black-box tools, meaning that the complete source code is available. Furthermore, non-commercial simulation tools mostly have a less extensive range of functions then commercial tools. The drawback of a limited set of functionalities comes with the advantage of a simpler software architecture. There are various power system simulation tools available that are based on MATLAB, for example MatPower [42], Power System Analysis Toobox (PSAT) [54], Power System Toolbox (PST) [55], MatDyn [56], Sim Power Systems (SPS) [57] and the Voltage Stability Toolbox (VST) [58]. Well known is also the Python based simulation tool Dome [59].

The comparison of the simulations tools is shown in Table 3.1. It can be seen that block diagram modeling is only possible in PowerFactory, PSS/E and SimPowerSystems (SPS). In all the other tools, custom model development takes place in either a standard programming language like *Python* or in a custom language that is specifically developed for the tool. Component modeling with graphical state machine models is only possible in SimPowerSystems (SPS). In SPS the state machine modeling approach is possible by using a Simulink toolbox called Stateflow®. An extensive model database, with all standard models being pre-implemented, is available in all commercial tools (PowerFactory, PSS/E, PowerWorld and PSLF) and also in PSAT, SPS and Dome. All the commercial tools and SimPowerSystems

Table 3.1: Comparison between MATLAB-based tools

Tool	Block diagram modeling	State machine modeling	Extensive model database	Non-black-box	Focused on command line usage
PowerFactory	✗	no	✗	no	no
PSS/E	✗	no	✗	no	no
PowerWorld	no	no	✗	no	no
GE PSLF	no	no	✗	no	no
PSAT	no	no	✗	✗	✗
PST	no	no	no	✗	✗
MatDyn	no	no	no	✗	✗
SPS	✗	✗	✗	no	no
VST	no	no	no	✗	no
Dome	no	no	✗	✗	✗

are black-box models. That means, that it is not possible to excess all parts of the source code. Optimized for command line usage are PSAT, PST MatDyn and Dome.

Overall, MatDyn does a very good job in overall flexibility because of its very good scripting capability. However, when it comes to integration with Simulink the MatDyn has drawbacks because models are natively developed in plain MATLAB code. On the other hand SimPowerSystems (SPS) is fully integrated into Simulink. Thus, the modeling of components can benefit from the flexible Simulink capabilities like block-diagram modeling and graphical state machine modeling. However, scripting capability is limited in SPS because the data is only given in the Simulink model and no human readable and easy accessible data format exists. Thus, to set up a new test case model, the user has to do a lot of manual work.

From Table 3.1 it can be seen that no tool fulfills all properties. An extensive model database is important if investigations with standard models are needed. This is often the case in industry. However, for research, the component models that are being investigated and used are most of the time developed from scratch anyway. Furthermore, the component models that are typically used for education are very limited. Thus it is acceptable if a phasor-based simulation tool for research and education is not equipped with an extensive model database right from the start. Moreover, the model database can evolve as the tool become more mature and sophisticated.

From the above analysis, the most important requirements for a phasor-based simulation tool that is used in research and education are

- Block diagram modeling
- Graphical state machine modeling
- Non-black-box
- Optimized for command line usage

As no state-of-the-art phasor-simulation tool fulfills all these properties, a phasor-framework is developed that fulfills these properties. Therefore, the developed tool represents a novelty among existing tools.

3.3 Design objectives for phasor-framework

Table 3.2 gives an overview of design goals for the phasor-framework. In order to reach these goals, the decision is made to develop the tool in a combination of MATLAB and Simulink. Simulink is used for the implementation of the algebraic-differential system of equations and MATLAB is used for data management and initialization. The usage of Simulink for component model development ensures that block diagram and state machine modeling is possible. The usage of MATLAB for data management ensures that the phasor-framework is naturally optimized and focused on command line usage. This is also the reason why the tool is build without a graphical network editor and with a graphical user interface. Other important benefits of using MATLAB/Simulink for the phasor-framework are:

1. Simulink offers a straight forward way to implement differential equations.
2. MATLAB is a convenient tool for data parsing, initialization, data analyzing and visualization. Thus, the overall process of dynamic simulation takes place in one environment and becomes very time efficient.
3. Most electrical engineering students are trained in MATLAB/Simulink and can start using the framework right away.

Table 3.2: Properties of phasor-framework

Tool	Block diagram modeling	State machine modeling	Extensive model database	Non-black-box	Focused for command line usage
Phasor-framework	✗	✗	no	✗	✗

Besides these hard facts, the soft design objectives for the phasor-framework are flexibility, vectorization and the fostering of knowledge in power systems and scripting. These soft properties are explained in more detail in the following:

1. **Flexiblity**
   Flexibility means that the user is able to modify all parts of the code in order to customize the simulation environment to his or her needs. Existing component models can be changed and new component models can be added quickly. For example, it is straight forward to create another output variable for a component model. In order to do this, a Simulink bus signal needs to be added to the component model. To give another example for the flexibility objective of the phasor-framework, lets assume that the user wants to simulate a fault with a fault reactances. By default, the phasor-framework will only allow to simulate faults with a fault resistance and does not support fault impedances. However, the user can manually modify the input data format for a fault and adjust the initialization routine accordingly. In research, there is often a need to test new approaches or simulation methods, and therefore the flexibility, as offered by the phasor-framework, is often beneficial.

2. **Vectorization**
   The phasor-framework should make use of the strength of MATLAB/Simulink, which is vectorization. Furthermore, the data structure is build via tables and matrices. For example, adding another component, e.g. a photovoltaic (PV) system, to the power system only consists of adding a new row in a MATLAB table. This new row results in a dimension increase of the output signal of the component in Simulink. This approach makes it possible to handle the data sets in a clear and overseeable way. Another benefit of the data structure is that it can be build up by scripting. Also, one input data set should only consist out of one MATLAB struct that. The MATLAB file should be simulated by executing the initialization routines and the Simulink model. This structure makes it also possible to handle many different scenarios and incorporate parameter variations and keep an overview of the scenarios that are being investigated.

3. **Fostering power system and scripting knowledge**
   It is intended that a user of the developed framework knows the basics of MATLAB/Simulink and has some advanced power system knowledge that is typically acquired in an undergraduate or graduate course on power systems. Whilst using the phasor-framework, the user should work very closely with the model equations and the grid algorithm. Therefore the user becomes familiar with the dynamic simulation methodology. It naturally becomes clear to the user, what the initialization routines does and how it is structured for new or adopted models. Furthermore, if the user wants to test a new model, there is the possibility to start right away with a hard-coded version in a simplified Simulink model. This will be explained in more detail in Section 3.6.1. As the

phasor-framework is completely built in MALTAB/Simulink, it is virtually impossible to perform dynamic Simulations without writing own scripts for data generation and data plotting. If a user needs to perform more complex simulations with parameter variations or place components at different positions in the grid, it becomes necessary to write more sophisticated data management scripts. Therefore the usage of the phasor-framework forsters not only power system knowledge but also knowledge in scripting. If the phasor-framework is used during a Bachelor or Master thesis, a student therefore aquires both of these useful skills.

3.4 Framework overview

In the following, on overview of the phasor-framework is given with respect to the data structure, the generation of input data, the principle simulation workflow, the simulation methodology and how electrical measurements are given.

3.4.1 Data structure

The input and output data is stored in a MATLAB struct. A struct is a MATLAB data type that holds fields of different data types like matrices or tables.

The input data struct contains matrices for the static (grid) data and tables for the dynamic (component) data. Table 3.3 shows all fields of the MATLAB struct for the input data. The data information can be separated into static and dynamic data. The static data is stored in the fields *Base*, *Bus*, *Branch* and *Gen*. These fields adhere to the MATPOWER [42] data format also used for the power flow tool described in Chapter 2 and depicted in Table 2.2. The usage of the MATPOWER data format ensures that MATPOWER test grids can be used if necessary. The field *Config* contains configuration data like the nominal frequency of the power system that is being investigated. For the representation of the dynamic data, tables are used. The dynamic data of a component can be obtained in different ways. One option is to take the data from the data sheet of the component. This is possible, e.g., in case of synchronous generators. Another option is to perform measurements and identify the parameters.

To show another example, the input data for the constant power load with time series is shown in Table 3.4. The first row contains the *bus*, at which the constant power load is connected to. The active and reactive powers are stored in the time series format of MATLAB. These time series objects are read by the Simulink model. The property of vectorization can be illustrated very well by looking at this component. If a power system with multiple time-dependent constant power loads is simulated, the table *Cpl_ts* contains all constant power loads. If, for example, the power system contains 108 constant power loads, then the table *Cpl_ts* has 108 lines. As the time series values are directly stored in MATLAB time-series objects, the values for active and reactive power of the constant power loads can be accessed directly via the MATLAB command line.

Table 3.3: Fields of the input data struct. The data that is needed for the initialization routine is marked with an asterix *.

Name	Type	Description
Static data (grid)		
Config	Table	Configuration data
Base	Table	Base values
* *baseMVA*	int	Base value for power
* *Bus*	Matrix	Grid buses with loads
* *Branch*	Matrix	List of grid impedances
* *Gen*	Matrix	Static generator data
* *PQULoad*	Matrix	List of components with voltage dependent active and reactive power injection
Dynamic data (components)		
SwitchingEvent	Table	User defined switch opening or closing
Fault	Table	User defined fault (example in Table 3.5)
InfiniteBus	Table	Infinite bus
Cpl	Table	Constant power load (example in Table 3.4)
Cpl_ts	Table	Constant power load with time series
Shunt	Table	Shunt element
PV	Table	Photovoltaic system
SG	Table	Synchronous generator
Diesel	Table	Diesel governor

Table 3.4: Input data table for a constant power load with time series.

Row	Unit	Description
bus	-	Bus number at which constant power load is placed
pq	timeseries	Active and reactive power values of the constant power load in the MATLAB time series format

The output data is a MATLAB struct with fields for each component (e.g. synchronous generator, loads, PV system) and for the grid. It contains all relevant data like voltages, currents or rotor speed of the synchronous generator. The data struct is stored in the MATLAB workspace after the time-domain simulation in Simulink is finished. By using scripts, this data struct can be stored and analyzed.

3.4.2 Generation of valid data sets and data parsing

The generation of a valid data set is the most crucial step for a user. It has to be taken great care that all necessary data is fed into the input data structure and that all parameters are correct. To help the user with this task, the phasor-framework contains a raw dataset which defines all possible components and contains sample parameters. For example, default values are given for each parameter of the PV generator. If the user wants to simulate a power system which contains a PV systems, the raw PV data can be taken from the raw dataset, copied into the original input data file and the appropriate parameters can be adjusted. This can all be done by scripting routines which the user can develop based on the specific power system that needs to be investigated. Another beneficial possibility is to generate multiple data sets with different parameters via for-loops. This is helpful in case that parameter variations need to be investigated. Thus, the scripting approach allows to generate a large variety of parameter variations to be investigated. After all input data sets are generated and stored, the phasor-framework can be used to simulate each and every input dataset and store the simulation results onto the hard drive. After that, the simulation results can be plotted by another scripting routing which is usually custom build by the user.

If some of the input data, e.g. line admittances, is not available in the format needed by the phasor-framework, a data parsing routine needs to be written by the user to alter the data format such that it fits into the predefined data structure of the phasor-framework. At the department of Energy Management and Power System Operation at University of Kassel, the open source grid planning tool pandapower [60] is being developed. Data parsing routines that are capable of parsing the grid data from the pandapower data format to the phasor-framework data format are available and have been successfully developed on the basis of a pandapower to MATPOWER converter.

3.4.3 Workflow

The phasor simulation itself is conducted within Simulink. The initialization and data manipulation takes place in MATLAB. The overall workflow of the phasor-framework can be seen in Fig. 3.1. The input data for a time-domain simulation is specified via a MATLAB struct with tables and matrices. This data struct is loaded into the MATLAB workspace. In the next step the initialization takes place.

First, the power flow data is composed - script (a) in Fig. 3.1. In this step the static data of all dynamic components is combined to form the data basis for the subsequent power flow. Oftentimes an inaccurate initialization of the dynamic simulation has its origin in wrong power injections of the power flow calculation. Thus, it is crucial to configure the power flow data correctly in this step.

In the next step, the power flow is conducted - script (b) in Fig. 3.1. For that, an efficient power flow algorithm is used. The development of this algorithm presents a novelty by itself and is presented in Chapter 2. This power flow routine includes voltage dependent active and reactive power injections, also called $P(V)$ and $Q(V)$

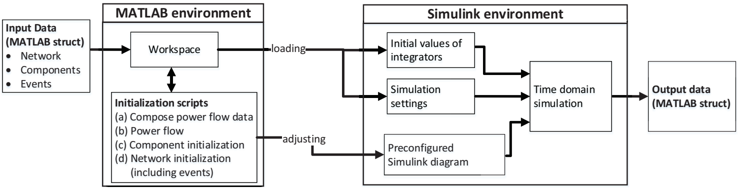

Figure 3.1: Workflow of the phasor-framework.

or local voltage control. Thus, the initialization routine is able to consider local voltage control of distributed generators. The power flow routine works on the static data seen in Table 3.3.

The power flow results (active and reactive power, voltages and currents at the terminals) are used to initialize all components - script (c) in Fig. 3.1. In this step, the preconfigured Simulink model is adjusted so that it fits the input data. For example, new signal connections are drawn and old ones are deleted if necessary.

After that, the grid equations are initialized - script (d) in Fig. 3.1. This includes the construction of the admittance matrix. User defined events usually change the grid impedances. Thus, a new admittance matrix is calculated for each user defined event (e.g. opening of switch) and stored in a lookup table.

After the initialization is done, the initial values for the state variables in Simulink are loaded from the MATLAB workspace. Furthermore, simulation settings like simulation time and time step are loaded. The standard setting is to use the variable step Simulink solver *ode23t* together with a maximum step size of 50 ms. In the next step, the time-domain simulation is executed by solving the system of differential algebraic equations (DAEs) in Simulink. In the end, the results are stored in an output data struct.

3.4.4 Simulation methodology

For conducting the time-domain simulation, the current-injection method is used [20]. An overview is shown in Fig. 3.2. Two types of models, namely current and voltage source models, are used. Current source models read the bus voltage and generate a current injection for that bus. Voltage source models read the bus current and generate a bus voltage. The mixed signal of bus currents and voltages is fed into the grid where bus voltages and currents are calculated.

As an example, a grid with four buses is considered. The grid is furthermore assumed to contain a voltage source, e.g. synchronous generator, at bus 1 and current sources, e.g. loads, at bus 2, 3 and 4. The grid equations would be:

$$\begin{bmatrix} I_1 \\ V_2 \\ V_3 \\ V_4 \end{bmatrix} = \mathbf{f}\left(\begin{bmatrix} V_1 \\ I_2 \\ I_3 \\ I_4 \end{bmatrix}\right) \tag{3.1}$$

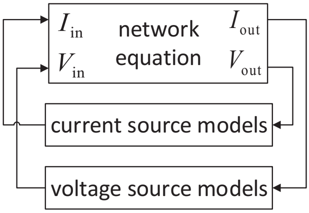

Figure 3.2: Solution method of the phasor-framework.

or

$$\begin{bmatrix} \mathbf{I}_{\text{out}} \\ \mathbf{V}_{\text{out}} \end{bmatrix} = \mathbf{f}\left(\begin{bmatrix} \mathbf{V}_{\text{in}} \\ \mathbf{I}_{\text{in}} \end{bmatrix}\right) \tag{3.2}$$

with $\mathbf{V}_{\text{in}} = \begin{bmatrix} V_1 \end{bmatrix}$, $\mathbf{I}_{\text{in}} = \begin{bmatrix} I_2 \ I_3 \ I_4 \end{bmatrix}^t$, $\mathbf{I}_{\text{out}} = \begin{bmatrix} I_1 \end{bmatrix}$ and $\mathbf{V}_{\text{out}} = \begin{bmatrix} V_2 \ V_3 \ V_4 \end{bmatrix}^t$. The linear function $\mathbf{f}$ is coupling the bus currents and voltages.

The static part of the phasor-framework, namely the network equations, were validated successfully against the MATPOWER [42] toolbox for various test cases. Concerning the dynamic behavior of the models, parts of the PV model were validated successfully against laboratory measurements as described in [61]. The synchronous generator model was validated on a small test system against the work presented in [34].

3.4.5 Measurements

In the Simulink diagram of the grid model and for each component model a measurement output is defined that gives the user access to model specific parameters for analyzing the simulation results. All measurement outputs are brought together into a single Simulink bus diagram and stored in the MATLAB workspace after each simulation run. This can be seen in Fig. 3.3. Each component has an output signal $m1, m2, ...$ They are combined into the bus signal m that is stored into the Workspace and contains time series of all relevant simulation data. For example, the injected active powers at each bus can be accessed via the MATLAB command *m.Grid.P*.

As an example the composition of the measurement signal for the grid is shown in Fig. 3.4. From the complex bus voltage $\underline{V}$ and bus current $\underline{I}$ the injected active P and reactive Q powers and the load angle ϕ are calculated. Finally, these 5 variables are merged into a common bus signal, which is connected to the output m_1 of the grid model.

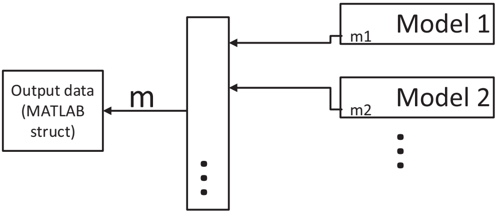

Figure 3.3: Solution method of the phasor-framework.

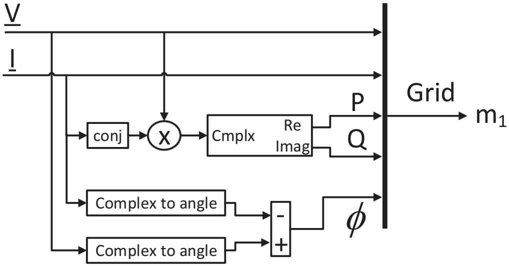

Figure 3.4: Simulink implementation of the measurement block for the grid model.

3.5 Grid model

3.5.1 Grid model equations

Let us assume a grid with n buses in which the buses that are connected to voltage source models have the indices $1, ..., m$ and the buses that are connected to current source models have the indices $m+1, ..., n$, where $m < n$. The admittance matrix $\mathbf{Y}$ couples the bus currents and voltages. A detailed explanation of how to construct the admittance matrix is found in [20, 34, 62]. It is:

$$\mathbf{I} = \mathbf{Y} \cdot \mathbf{V} \tag{3.3}$$

where $\mathbf{V} = \begin{bmatrix} V_1, \ldots, V_n \end{bmatrix}^t$ is the bus voltage vector and $\mathbf{I} = \begin{bmatrix} I_1, \ldots, I_n \end{bmatrix}^t$ is the bus current vector. Following the notation of (3.2), the voltage and current vector can be split into $\mathbf{V} = \begin{bmatrix} \mathbf{V}_{\text{in}} & \mathbf{V}_{\text{out}} \end{bmatrix}^t$ and $\mathbf{I} = \begin{bmatrix} \mathbf{I}_{\text{out}} & \mathbf{I}_{\text{in}} \end{bmatrix}^t$ with $\mathbf{V}_{\text{in}} = \begin{bmatrix} V_1, \ldots, V_m \end{bmatrix}^t$, $\mathbf{V}_{\text{out}} = \begin{bmatrix} V_{m+1}, \ldots, V_n \end{bmatrix}^t$, $\mathbf{I}_{\text{in}} = \begin{bmatrix} I_{m+1}, \ldots, I_n \end{bmatrix}^t$ and $\mathbf{I}_{\text{out}} = \begin{bmatrix} I_1, \ldots, I_m \end{bmatrix}^t$. Furthermore, the admittance matrix is divided into submatrices $\mathbf{Y}_{\text{in}}$, $\mathbf{Y}_{\text{out}}$, $\mathbf{Y}_{\text{in\_out}}$, $\mathbf{Y}_{\text{out\_in}}$ at the

m-th row and at the m-th column. For example the submatrix $\mathbf{Y}_{\text{out}}$ is:

$$\mathbf{Y}_{\text{out}} = \begin{bmatrix} y_{m+1,m+1} & \cdots & y_{m+1,n} \\ \vdots & \ddots & \vdots \\ y_{n,m+1} & \cdots & y_{n,n} \end{bmatrix} \tag{3.4}$$

The submatrices $\mathbf{Y}_{\text{in}}$, $\mathbf{Y}_{\text{in\_out}}$ and $\mathbf{Y}_{\text{out\_in}}$ are constructed such that (3.3) can be written as:

$$\begin{bmatrix} \mathbf{I}_{\text{out}} \\ \mathbf{I}_{\text{in}} \end{bmatrix} = \begin{bmatrix} \mathbf{Y}_{\text{in}} & \mathbf{Y}_{\text{in\_out}} \\ \mathbf{Y}_{\text{out\_in}} & \mathbf{Y}_{\text{out}} \end{bmatrix} \begin{bmatrix} \mathbf{V}_{\text{in}} \\ \mathbf{V}_{\text{out}} \end{bmatrix} \tag{3.5}$$

or

$$\mathbf{I}_{\text{out}} = \mathbf{Y}_{\text{in}}\mathbf{V}_{\text{in}} + \mathbf{Y}_{\text{in\_out}}\mathbf{V}_{\text{out}} \tag{3.6a}$$

$$\mathbf{I}_{\text{in}} = \mathbf{Y}_{\text{out\_in}}\mathbf{V}_{\text{in}} + \mathbf{Y}_{\text{out}}\mathbf{V}_{\text{out}} \tag{3.6b}$$

The unknown voltage $\mathbf{V}_{\text{out}}$ can be calculated with (3.6b):

$$\mathbf{V}_{\text{out}} = \mathbf{Y}_{\text{out}}^{-1}(\mathbf{I}_{\text{in}} - \mathbf{Y}_{\text{out\_in}}\mathbf{V}_{\text{in}}) \tag{3.7}$$

Then, the unknown currents can be calculated with (3.6a).

3.5.2 Grid model implementation

In the grid equations of the phasor-framework, the voltages of the voltage source models and the currents of the current source models are fed into (3.7) to calculate the bus voltages of the current sources. In the next step, (3.6a) is used to obtain the currents of the voltage source models. The admittance matrix and its inverse are precalculated during initialization to save computational time during the simulation. All passive components of the grid are incorporated into the admittance matrix. For example, a shunt element at bus i changes the self admittance of that bus, namely the entry (i, i) of the admittance matrix.

A switching event or a fault changes the topology and thus the admittance matrix. For example, a switching event at time $t = t_1$ will result in a different admittance matrix in the grid equations when the simulation time reaches t_1. To incorporate this into the Simulink model, the different admittance matrices $\mathbf{Y}_{\text{in}}$, $\mathbf{Y}_{\text{out}}$, $\mathbf{Y}_{\text{in\_out}}$, $\mathbf{Y}_{\text{out\_in}}$ are precalculated during initialization and stored in lookup tables. Thus, the grid equations are updated at each time a topology change happens. The topology variations that happen during a simulation run are determined by in the input data. In Simulink, this procedure is realized via a time dependent index that selects the appropriate matrix from a lookup table.

3.6 Component models

In the following paragraph the modeling approach for a component is explained. Further details can be found in the Appendix A.1 and A.2. The implementation of a diesel generator with droop control, a synchronous generator and a small-scale PV Systems is described in Chapter 4.

3.6.1 Modeling approach

As described in Section 3.5, two basic types of models exist in the phasor-framework. These are voltage source models and current source models. Current source models feed in a certain amount of current into the point of common coupling based on the bus voltage. Voltage source models are capable of modeling components that are able to control the voltage to a certain set point due to their reactive power capabilities. As in Section 3.5, a power system with n buses, m voltage source models and $n - m$ current source models is assumed in this section in order to explain the basic implementation strategy for voltage and current source model within the phasor-framework.

An overview of the implementation of current source models is given in Fig. 3.5. This figure is a more detailed version of the current source models block in Fig. 3.2. As can be seen from Fig. 3.2, the input to all current source models is the voltage vector V_{out}. V_{out} has the dimension $[(n-m)\times 1]$ because the amount of current source components is $n - m$. As explained in Section 3.5.1 it is $\mathbf{V}_{\text{out}} = \left[V_{m+1}, \ldots, V_n\right]^t$. In Fig. 3.5, two current source models CS1 and CS2 are shown. They could, e.g., represent constant power loads (CS1) and PV systems (CS2). More models could be added which is represented by the dots. Each current source model can be connected to multiple buses. In Fig. 3.5 the current source model CS1 occurs k_1 times in the network and CS2 occurs k_2 times in the network. This would mean that in the complete network k_1 constant power loads (CS1) and k_2 PV systems are present. The selector selects the relevant bus voltages for each current source model out of the full voltage output vector $\mathbf{V}_{\text{out}}$. Thus, behind the selector, a voltage vector V_{CS1} with the dimension of $[k_1]$ is fed into the actual model equations of CS1. The model equations of the component CS1 are applied to all current sources of type CS1 simultaneously during a simulation run. The output of the model equations of CS1 is a current injection vector I_{CS1} with dimension $[k_1]$. After that, a Simulink assignment block is used to a create larger vector $I_{\text{CS1,full}}$ with dimension $[(n-m)]$ by filling up zeros at the appropriate places. The full current vectors of all components $I_{\text{CS2,full}}$,$I_{\text{CS2,full}}$,... are finally added to form the vector I_{in} with dimension $[(n - m)]$. I_{in} is fed into the grid model as displayed in Fig. 3.2.

An overview of the implementation of voltage source models is given in Fig. 3.6. This figure is a more detailed version of the voltage source models block in Fig. 3.2. The input to all voltage source models is the bus current vector I_{out} which has the dimension $[m \times 1]$. The implementation of voltage source components as displayed in Fig. 3.6 is in principle the same as the implementation of current source models displayed in Fig. 3.5. The key difference is the dimension of the input and output vector. The input vector of all voltage source models is I_{out} which has a dimension of $[m]$ because it is assumed that m voltage sources are present in the system. The amount of voltage sources that behave according the the voltage source model VS_i is p_i. It is $\sum_i p_i = m$.

An example for the internal vectors of VSI and CSI can be found in the Appendix A.1. In the Appendix A.2 the process of adding a new component model to the RMS-framework is described.

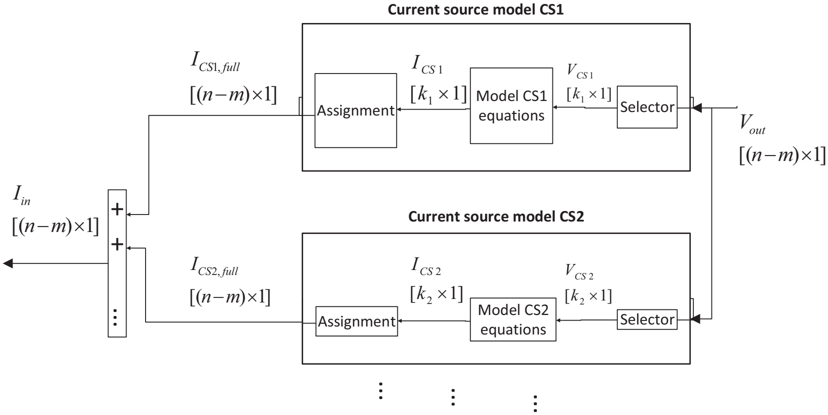

Figure 3.5: Simulink implementation of the current source models. This is a detailed version of the current source models block in Fig. 3.2.

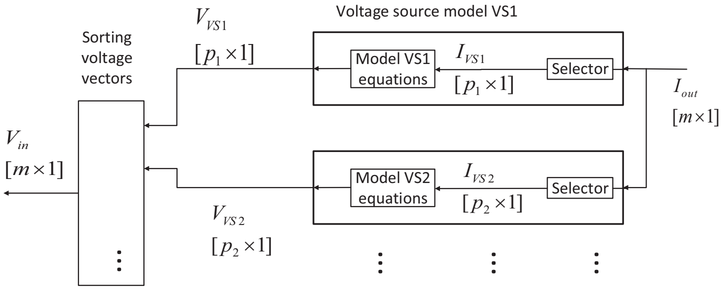

Figure 3.6: Simulink implementation of the voltage source models. This is a detailed version of the voltage source models block in Fig. 3.2.

3.7 Fault simulation

With the rms-framework it is possible to simualate three phase faults. The input data set for a fault is depicted in Table 3.5. This data is stored in the overall MATLAB struct in a table format. This table contains all relevant information that is needed by the phasor-framework to incorporate a fault into the simulation. In the field *bus*, the bus number is given at which the fault should happen. In the phasor-framework, faults are modeled by a fault impedance (or resistance). This is done by adding the appropriate impedance values to the admittance matrix. In the next two rows, the time t at which the fault is happening and its *duration* in seconds is given. After that, the fault resistance r is given. A useful option of the fault model implemented in the phasor-framework is line clearing. If the line clearing option is set to yes, then the line that is affected by the fault is switched off after the fault occurred. To precisely identify the line that is being switched of, the beginning and end of the line as denoted with the *from* and the *to* option.

The behavior of the synchronous machine (implementation described in Chapter 4) in response to a fault was verified. Therefore, the single machine infinite bus (SMIB) test system proposed by Kundur in [34] and displayed in Fig. 3.7, was implemented into the phasor-framework.

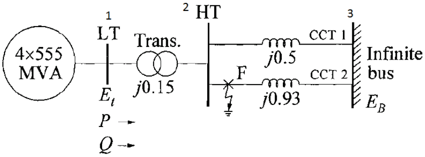

Figure 3.7: Kundur single machine infinite bus system [34].

For the verification of the static working points, the voltages at each bus as computed by the phasor-framework were compared to the voltages provided by [34]. The results are shown in Table 3.6 and it can be seen that the values match.

Table 3.5: Input data table for definition of a fault.

Row	Unit	Description
bus	-	Bus number at which fault is taking place
t	s	Time at which the fault is happening
duration	s	Duration of the fault
r	Ω	Fault resistance
line_clearing	yes/no	Is the line cleared or not
from	-	Line which will be cleared (from bus)
to	-	Line which will be cleared (to bus)

A three phase fault at bus 2 is applied at $t = 12\,\mathrm{s}$. The input data for this type of fault for the case $t_c = 0.7\,\mathrm{s}$ is displayed in Table 3.7. The response of the rotor angle, as computed by the phasor-framework, can be seen in Fig. 3.8. This response corresponds well to the response shown in the book of Kundur [34] and shown in Fig. 3.9. Even though the modeling of transient rotor angle responses to faults are not in the focus of this thesis, this section shows very well the general capability of the phasor-framework for this type of application.

Table 3.6: Comparison of initial voltage values for fault simulation of SMIB.

Bus	V_1	V_2	V_3
phasor-framework	$1.0\angle 28.34°$	$0.944\angle 20.124°$	$0.901\angle 0°$
Kundur	$1.0\angle 28.34°$	NA	$0.90081\angle 0°$

Table 3.7: Input data for parameterizing the fault in the SMIB system.

Bus	t_s	duration	r_{pu}	line_clearing	from	to
2	12	0.07	1e-05	'yes'	2	3

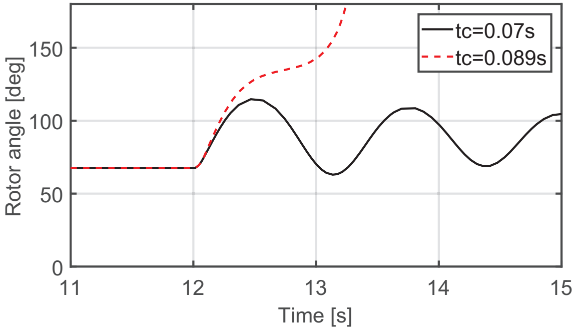

Figure 3.8: Plot of the rotor angle in the Kundur single machine infinite bus system for two different fault clearing times t_c.

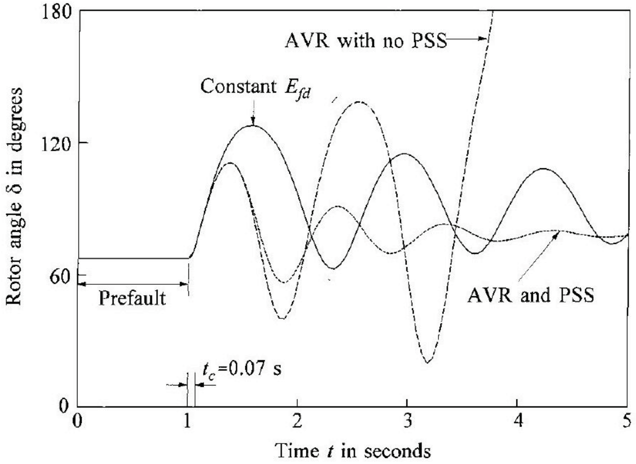

Figure 3.9: Result from Kundur [34]. The most important part of the plot is the line with constant E_{fd}. This line corresponds well with the result for the clearing time $t_c = 0.07$ in Fig. 3.8.

3.8 Parameter variation

With the phasor-framework it is very convenient to implement parameter variations. Fig. 3.10 shows the principle scheme of doing that. The basis is a wrapper script which loads different input data structs from a MATLAB cell array, performs a time-domain simulation and returns an output cell array. This output cell array contains structs of output data. The different input data structs can be build conveniently by using MATLAB scripts. In order to save memory it is also be possible to create a wrapper script that works with the same input data file and only changes one parameter at a time.

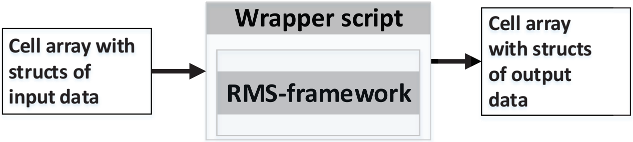
Cell array with structs of input data
Wrapper script
RMS-framework
Cell array with structs of output data

Figure 3.10: Simulating parameter variation with the help of a wrapper script.

3.9 Discussion on phasor-framework

University courses on electrical power systems can be greatly enhanced by integrating easy-to-understand and flexible simulation tools [63, 64, 65]. Thus, for dynamic power system simulations in an academic environment, it is important that the model development process is fast and with as little software overhead as possible. Furthermore, it is beneficial in a University environment if a power system simulation tool is not a black box model. In this way, students and researchers can modify and also understand the complete internal structure of the tool. The phasor-framework developed in this work features both, rapid prototyping and a non-black-box approach. Therefore it is a suitable tool for usage in research and education.

The phasor-framework is now discussed with respect to the simulation method, the component modeling, the usability and data analysis. Furthermore, benefits are discussed if the framework is used in education and in research. The section concludes with a brief discussion on the main drawback of the phasor-framework.

Simulation method

For the phasor-framework all simulation methods (RMS, power flow) need to be implemented and validated from scratch. This is very time consuming and is furthermore a challenging task from a software as well as from an engineering point of view. In commercial off-the-shelf products, most state-of-the-art simulation methods are already implemented in the purchased product. Thus, the user only needs to become familiar with the working environment and can start right away with simulation. This shortens the time that is needed to produce first results. However, as commercial tools mostly incorporate several of the state-of-the-art simulation methods, the interface and internal program structure is rather complex. In the phasor-framework only the simulation methods that are needed for the current problem are implemented and thus the program structure and data format is more simple. Furthermore, the simulation method is open to the user and the user has full access to all calculation steps. A commercial tool, on the other hand, is a black-box concerning the simulation method and the user relies on the product documentation if he wants to comprehend the internal calculation steps.

Component modeling

In the phasor-framework all models need to be build from scratch which is a lot of work. This downside has the advantage that the complete internal model structure and its interface to the grid is known. In a commercial tool oftentime various models are already implemented and are ready to be used. However, in practical applications and especially in a research environment, custom models are needed anyway which also have to be build from scratch. Thus one can conclude that for research applications the necessity to develop custom models is existing anyway. Thus, the advantage of pre-implemented models within commercial tools is limited.

Usability and data analysis

The phasor-framework is script based and therefore very flexible with respect to composing and simulating different simulation scenarios as well as analyzing the results. For example, plotting can be done directly in MATLAB. On the other hand, commercial tools are mostly oriented towards a graphical user interface (GUI), as e.g. PowerFactory®[18] and Siemens PSS®E . This is user friendly but less flexible. Oftentimes an interface to a scripting language exists but the interface is most of the time not very easy to handle. Within most commercial tools, simple plots can be generated. However, for producing customized plots, most of the time, the results have to be stored to a text file and plotted with a second tool like Python or MATLAB. Another important feature of the MATLAB environment is the possibility of debugging. As this feature comes natively with the MATLAB environment, the self developed phasor-framework can, of course, be debugged which helps resolving programming errors. On the other hand, debugging is often not possible or very limited in commercial tools which can make error searching very difficult. Last but not least, a large MATLAB user community exists. Thus, programming issues can be solved with the help of a huge knowledge base. The user community of most commercial tools is limited to a few big companies. Thus, the existence of online help is limited and the user is dependent on the customer support.

Benefits for education

The field of power system dynamics is very broad. To understand the fundamental concepts, students need to be familiar with basics in electrical machines, the admittance matrix, power flow calculation, phasor and time-domain representation of electrical signals as well as basics in control theory. From this foundation, the students can be introduced into the topic of power system dynamics and stability which includes the modeling of components like the synchronous generator and stability analyzes like small-signal stability, voltage stability, transient stability and frequency stability. This knowledge is both, challenging and highly interesting from the theoretical point of view. Thus a thorough education in the theoretical aspects is crucial for university level courses on power system dynamics. If this is combined with knowledge about modeling, simulation and implementation of power system dynamic problems, the students are furthermore able to gain an insight into possible ways to solve real world dynamic problems. The phasor-framework developed within this PhD thesis presents a good option to introduce students to the practical way of dynamic power system simulation. The phasor-framework can, for example, be used in exercises that accompany a lecture about power system dynamics or the framework can be used as a main tool in a lecture about modeling and simulation of power systems. One of the main benefits of using the phasor-framework in education is that the students gain an insight into the, often hidden, core functionalities and functioning of professional power system simulation tools that are used by grid operators. Thus, this type of education will also help them to use these professional tools later on because they have a grasp of what kind of algorithms lays beneath the surface.

Benefits for research
A very important part for targeting research questions in power system dynamics lays in a flexible approach for modeling and simulation of power systems. Furthermore, it is essential that the researcher knows what is going on inside the simulation tool that is being used. Both requirements are fulfilled with the phasor-framework. Its flexibility towards the development and implementation of new component models allows for fast prototyping. Furthermore, the full modeling potential of Simulink can be used. For example the incorporation of state diagrams is possible within the phasor-framework. This is, to the knowledge of the author, not possible in state-of-the-art commercial power system simulation tools.

Main drawback of phasor-framework
From Table 3.2, the main drawback of the phasor-framework becomes clear. The phasor-framework does not have a comprehensive database of pre-implemented component models. As discussed before, most components that are used in a research environment are non-standard models anyway, this drawback can be overcome by implementing the models on the fly as they are needed. The main benefit of the phasor-framework is the model development process which can be done with state machines. Even though SimPowerSystem (SPS) offers the same feature, it has to be noted that SPS is mainly oriented towards EMT simulation and is not the most suitable tool for phasor-simulations of larger grids. However, the lack of a comprehensive model database within the phasor-framework clearly represents a limitation to the usage of the tool.

3.10 Conclusion

A flexible phasor-framework was presented in this chapter. The main targeted user group of the framework are researchers and students. Due to its flexibility, it is straight forward to include new component models or to change existing models to fulfill individual requirements. The phasor-framework allows block diagram and state machine modeling in a graphical way. Furthermore it is a non-black-box tool and optimized for command line usage.

All these features combined make it a novel tool for dynamic phasor-mode simulations for electrical power systems. A phasor simulation environment that is as flexible, and at the same time as simple as the framework presented is not known to the authors. Furthermore, users become familiar with dynamic grid equations by using the phasor-framework. Therefore, the authors are convinced that by using the presented phasor-framework in a teaching environment, practical power system knowledge can be delivered to the students.

Future work could include an efficient implementation of (3.7). This would involve LU-factorization of $\mathbf{Y}_{\mathrm{out}}$ to exploit its sparse nature and to avoid the direct calculation of the inverse of $\mathbf{Y}_{\mathrm{out}}$. With $\mathbf{Y}_{\mathrm{out}} = \mathbf{L}{\cdot}\mathbf{U}$ and $\mathbf{B} = \mathbf{I}_{\mathrm{in}} - \mathbf{Y}_{\mathrm{out\_in}}\mathbf{V}_{\mathrm{in}}$ equation (3.6b) is $\mathbf{B} = \mathbf{L}{\cdot}\mathbf{U}{\cdot}\mathbf{V}_{\mathrm{out}}$. With $\mathbf{x} = \mathbf{U}{\cdot}\mathbf{V}_{\mathrm{out}}$, the solution of $\mathbf{L}{\cdot}\mathbf{x} = \mathbf{B}$ is obtained for $\mathbf{x}$, and then the solution $\mathbf{U} \cdot \mathbf{V}_{\text{out}} = \mathbf{x}$ for $\mathbf{V}_{\text{out}}$ can be calculated. Furthermore, the structure of the grid model could be adapted to support the simulation of multiple grid areas. This would enable the investigation of the synchronization of two grid areas. Future work could also include the development of more component models like tap changing transformers, wind turbines, batteries, voltage source inverters, governor models like gas turbines and IEEE standard excitation systems. Furthermore, the network model could be improved to allow the simulation of electrically separated grids.

Chapter 4

Model development

4.1 Introduction

The phasor-framework presented in chapter 3 is a software framework for the conduction of RMS-simulations of power systems. In order to use the phasor-framework for a specific real-world problem it needs to be equipped with realistic models suitable for tackling the problem. Thus, model development has to take place after the problem is defined. In case of this work, the problem that needs to be tackled is the investigation of the reconnection behavior of photovoltaic systems in a low-voltage island grid. This study is presented in chapter 5. Thus, a photovoltaic system model needs to be developed that includes a model for reconnection behavior. Another requirement for the photovoltaic model is the correct modeling of the dynamic behavior of the voltage dependent active and reactive power injection. The fidelity of the synchronous generator model used in an RMS-simulation depends on the problem that is investigated. For the simulation of the reconnection behavior of photovoltaic systems in a low-voltage island grid it is sufficient to use a third order synchronous generator model with damper winding neglected. This is because the time constants of the damper windings are clearly below one second and the simulation time of the investigation is in the range of seconds up to minutes.

This chapter is structured as follows. In section 4.2 the synchronous generator model and its implementation is described in detail. In section 4.3 the diesel generator model that is used as a governor for the case study in chapter 5 is presented briefly. In section 4.4 the development and implementation of the photovoltaic system is described in detail. This section contains novelties in two areas. In the area of simulation, the novelty is the usage of a state diagram for modeling of the different states that the photovoltaic system is in. In state-of-the-art simulation tools (e.g. PowerFactory), state diagrams need to be implemented in plain code which can become cumbersome and often the code becomes elusive. The usage of Simulink state diagrams opens up new possibilities concerning code comprehension and fast model development. In the area of model development, the photovoltaic model includes a dynamic model of the voltage dependent active and reactive power injection which is validated with laboratory measurements. Such a validated model adds useful knowledge to the research community in which there is always a need for model descriptions that are closely linked to real measurement. As section 4.4 is such an integral part of this thesis, there is a separate introduction to the topic of photovoltaic system modeling in Subsection 4.4.1.

This chapter is partly based on the publications

D. Fetzer, G. Lammert, K. Fischbach, M. Nuhn, J. Weide, D. Lafferte, T. Paschedag, M. Braun, *Modelling of Small-Scale Photovoltaic Systems with Active and Reactive Power Control for Dynamic Studies, 6th Solar Integration Workshop (published in the workshop's proceedings)*, Vienna, Austria, November 14-15, 2016.

D. Fetzer, G. Lammert, T. Paschedag, D. Lafferte, K. Fischbar, M. Nuhn, C. Jaehner, H. Becker, L.R. Roose, M. Braun, *Reconnection of Photovoltaic Systems in Low-Voltage Diesel-Powered Microgrids*, 1st International Conference on Large-Scale Grid Integration of Renewable Energy in India, New Delhi, September 6-8 2017 (published in the conference's proceedings)

4.2 Synchronous generator

The synchronous generator model, implemented in the phasor-framework, is a simplified model with damper windings neglected. It is based on the equations presented in [34]. In this model, the transformer voltages $\frac{d}{dt}\psi_{\mathrm{d}} = 0$ and $\frac{d}{dt}\psi_{\mathrm{q}} = 0$, that occur due to a flux change in time, are neglected. Furthermore, the rotor speed variations in the stator voltage equations are neglected by assuming $\omega_r = 1$. This counterbalances the effect of neglecting the transformer voltages for small perturbations as is shown in [34].
An overview of the implementation of the synchronous generator is shown in Fig. 4.1. The model consists of the synchronous generator, the governor and the voltage regulator. The inputs of the synchronous generator are the complex injected terminal current $\underline{I_{\mathrm{t}}}$, the speed of the reference generator $\omega_{\mathrm{ref,gen}}$, the excitation voltage e_{fd} and the mechanical torque T_{m}. All values are in per unit. The output is the complex terminal voltage phasor $\underline{E_{\mathrm{t}}}$ and the rotor speed ω_{r}. The inputs of the governor are the rotor speed of the synchronous generator ω_{r} and the reference speed of the governor $\omega_{\mathrm{gov,ref}}$. The output is the mechanical torque. The inputs of the voltage regulator are the reference voltage magnitude V_{ref} and the terminal voltage magnitude E_{t}. The output is the field voltage e_{fd}. The reference speed of the governor $\omega_{\mathrm{gov,ref}}$ is used for the speed control for the governor. It is different from the speed of the reference generator $\omega_{\mathrm{ref,gen}}$. If there is only one machine in the system, then $\omega_{\mathrm{ref,gen}} = \omega_{\mathrm{r}}$.

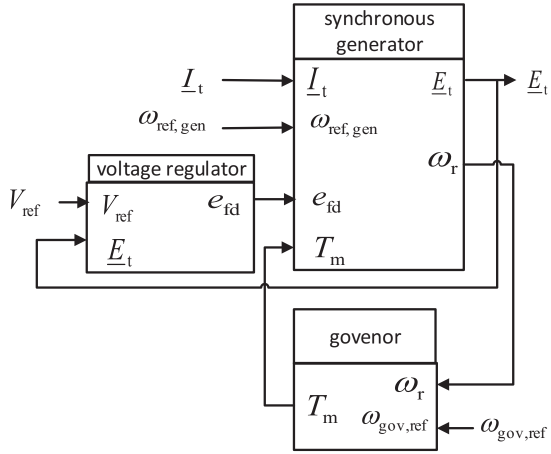

Figure 4.1: Overview of synchronous generator model.

4.2.1 Electrical equations

The stator voltage equations are:

$$e_{\mathrm{d}} = -\psi_{\mathrm{q}} - R_{\mathrm{a}} i_{\mathrm{d}} \tag{4.1a}$$
$$e_{\mathrm{q}} = \psi_{\mathrm{d}} - R_{\mathrm{a}} i_{\mathrm{q}} \tag{4.1b}$$

The flux linkage equations are:

$$\psi_{\mathrm{d}} = -L_{\mathrm{d}} i_{\mathrm{d}} + L_{\mathrm{ad}} i_{\mathrm{fd}} \tag{4.2a}$$
$$\psi_{\mathrm{q}} = -L_{\mathrm{q}} i_{\mathrm{q}} \tag{4.2b}$$
$$\psi_{\mathrm{fd}} = -L_{\mathrm{ad}} i_{\mathrm{d}} + L_{\mathrm{ffd}} i_{\mathrm{fd}} \tag{4.2c}$$

The rotor voltage equation is:

$$e_{\mathrm{fd}} = \frac{1}{\omega_{\mathrm{base}}} \frac{d\psi_{\mathrm{fd}}}{dt} + R_{\mathrm{fd}} i_{\mathrm{fd}} \tag{4.3}$$

Equations (4.1), (4.2) and (4.3) form the basis of the electrical model of the simplified synchronous generator model. From this point on, there are many choices for implementation. For the phasor-framework, the synchronous generator is implemented as a voltage source model, thus the terminal currents i_d and i_q are input variable. Furthermore, the excitation voltage is chosen to be an input variable. Therefore, the stator and rotor voltage equations and the flux linkage equations are rearranged such that the vector $\begin{bmatrix} i_{\mathrm{d}} & i_{\mathrm{q}} & \psi_{\mathrm{fd}} \end{bmatrix}^t$ is an input. Inserting (4.2b) into (4.1a) results in

$$e_{\mathrm{d}} = L_{\mathrm{q}} i_{\mathrm{q}} - R_{\mathrm{a}} i_{\mathrm{d}} = \begin{bmatrix} -R_{\mathrm{a}} & L_{\mathrm{q}} & 0 \end{bmatrix} \cdot \begin{bmatrix} i_{\mathrm{d}} \\ i_{\mathrm{q}} \\ \psi_{\mathrm{fd}} \end{bmatrix} \tag{4.4}$$

Inserting (4.2a) into (4.1b) results in

$$e_{\mathrm{q}} = -L_{\mathrm{d}} i_{\mathrm{d}} + L_{\mathrm{ad}} i_{\mathrm{fd}} - R_{\mathrm{a}} i_{\mathrm{q}} \tag{4.5}$$

Rearranging (4.2c) results in

$$i_{\mathrm{fd}} = \frac{\psi_{\mathrm{fd}} + L_{\mathrm{ad}} i_{\mathrm{d}}}{L_{\mathrm{ffd}}} = \begin{bmatrix} \frac{L_{\mathrm{ad}}}{L_{\mathrm{ffd}}} & 0 & \frac{0}{L_{\mathrm{ffd}}} \end{bmatrix} \cdot \begin{bmatrix} i_{\mathrm{d}} \\ i_{\mathrm{q}} \\ \psi_{\mathrm{fd}} \end{bmatrix} \tag{4.6}$$

Inserting (4.6) into (4.5) yields

$$e_{\mathrm{q}} = -L_{\mathrm{d}} i_{\mathrm{d}} + L_{\mathrm{ad}} \left(\frac{\psi_{\mathrm{fd}} + L_{\mathrm{ad}} i_{\mathrm{d}}}{L_{\mathrm{ffd}}} \right) - R_{\mathrm{a}} i_{\mathrm{q}} \tag{4.7}$$

and in vector form

$$e_{\mathrm{q}} = \begin{bmatrix} L_{\mathrm{ad}}^2 / L_{\mathrm{ffd}} - L_{\mathrm{d}} & -R_{\mathrm{a}} & L_{\mathrm{ad}} / L_{\mathrm{ffd}} \end{bmatrix} \cdot \begin{bmatrix} i_{\mathrm{d}} \\ i_{\mathrm{q}} \\ \psi_{\mathrm{fd}} \end{bmatrix} \tag{4.8}$$

From (4.4), (4.8) and (4.6) the model equations can be written in matrix form:

$$\begin{bmatrix} e_{\mathrm{d}} \\ e_{\mathrm{q}} \\ i_{\mathrm{fd}} \end{bmatrix} = \begin{bmatrix} -R_{\mathrm{a}} & L_{\mathrm{q}} & 0 \\ L_{\mathrm{ad}}^2 / L_{\mathrm{ffd}} - L_{\mathrm{d}} & -R_{\mathrm{a}} & L_{\mathrm{ad}} / L_{\mathrm{ffd}} \\ L_{\mathrm{ad}} / L_{\mathrm{ffd}} & 0 & 1 / L_{\mathrm{ffd}} \end{bmatrix} \cdot \begin{bmatrix} i_{\mathrm{d}} \\ i_{\mathrm{q}} \\ \psi_{\mathrm{fd}} \end{bmatrix} \tag{4.9a}$$

$$\frac{d\psi_{\mathrm{fd}}}{dt} = \omega_{\mathrm{base}} \left(e_{\mathrm{fd}} - R_{\mathrm{fd}} i_{\mathrm{fd}} \right) \tag{4.9b}$$

The electrical torque in per unit is calculated as:

$$T_{\mathrm{e}} = \psi_{\mathrm{d}} i_{\mathrm{q}} - \psi_{\mathrm{q}} i_{\mathrm{d}} \tag{4.10}$$

The implementation of the electrical synchronous generator equations is shown in Fig. 4.2. The complex terminal current $\underline{I_t}$ is transformed into the dq-frame via (4.15). After that, (4.9a) is used to calculate the e_{d}, e_{q} and i_{fd}. The complex terminal voltage $\underline{E}_{\mathrm{t}}$ is calculated via (4.15). The field current i_{fd} is used as an input for the flux equation (4.9b).

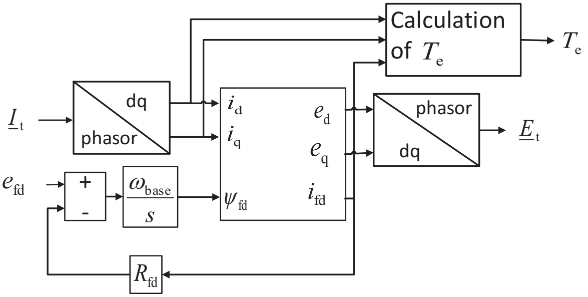

Figure 4.2: Implementation of electrical synchronous generator equations.

4.2.2 Mechanical equations

The basic mechanical equation in per unit formulation is:

$$\frac{d\omega_r}{dt} = \frac{T_m - T_e - K_D(\omega_r - \omega_{ref,gen})}{2H} \tag{4.11}$$

where T_e and T_m are the electrical and mechanical torque, K_D the damping coefficient, ω_r the mechanical speed of the rotor, $\omega_{ref,gen}$ the mechanical speed of the reference machine of the grid in per unit. The term $K_D(\omega_r - \omega_{ref,gen})$ represents the damping torque. It is proportional to the deviation of the rotor speed to the reference speed. The inertia time constant H is defined as:

$$H = \frac{1}{2}\frac{J\omega_{0m}^2}{\mathrm{VA_{base}}} \tag{4.12}$$

with the rated angular velocity of the rotor ω_{0m} in mechanical radians per second, the rated apparent power of the synchronous generator $\mathrm{VA_{base}}$ in VA and the inertia constant J of the rotor in kg·m^2.

The rotor angle of the synchronous generator can be calculated as the difference between the position of the rotor of the reference machine and the position of the rotor of the synchronous generator. This is done by integrating both, the speed of the reference generator and the speed of the synchronous generator in absolute values. Thus it is:

$$\delta = \int_0^t \omega_{0m}(\omega_r - \omega_{ref,gen}) \tag{4.13}$$

The implementation of the mechanical equations is shown in Fig. 4.3. The mechanical torque is obtained from the governor, and the electrical torque is obtained from the electrical equations. The speed of the rotor is calculated via (4.11), and the rotor angle is determined with (4.13).

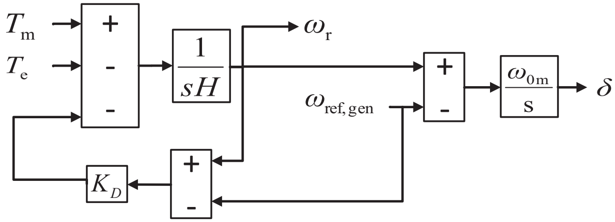

Figure 4.3: Implementation of mechanical synchronous generator equations.

4.2.3 dq-transformation

If the voltage at the component terminal is expressed as:

$$\underline{E_t} = E_t e^{j\alpha} \tag{4.14}$$

where E_t is the magnitude and α the angle in radians of the voltage phasor, then the dq-components e_d and e_q of the voltage are:

$$e_d + je_q = \underline{E_t} \cdot e^{-j\delta} \tag{4.15}$$

where δ is the rotor angle as defined in (4.13). This can also be expressed as $e_d = E_t \cos(\alpha - \delta)$ and $e_q = E_t \sin(\alpha - \delta)$. The reverse transformation from dq-domain into the complex phasor domain is:

$$\underline{E_t} = (e_d + je_q) \cdot e^{j\delta} \tag{4.16}$$

The implementation of the dq-transformation from phasor-domain to dq-domain is shown in Fig. 4.4. The phasor, in this case the bus voltage $\underline{E_t}$, is first separated into its magnitude E_t and phase α. With the help of the rotor angle δ the dq-components e_d and e_q are obtained.

Even though the formula and implementation of the dq-transformation is by itself rather simple, a correct implementation is very crucial for a proper functioning of the whole phasor-framework. In literature there are some variations for the definition of the rotor angle. Furthermore, great care has to be taken with respect to the sign of the dq-transformation. Thus, the information about the implementation of the dq-transformation given in Fig. 4.4 might seem obvious, but it is crucial for the overall phasor-framework.

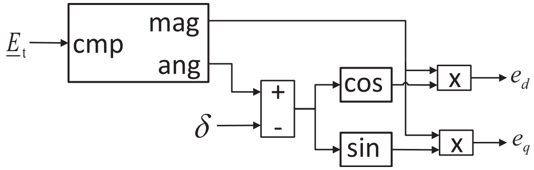

Figure 4.4: Implementation of the dq-transformation.

4.2.4 Conversion of standard into fundamental parameters

The input data for the synchronous generator is given in Table 4.1. It contains the most common machine parameters, also called standard parameters. These include synchronous, transient and subtransient reactances, open and short circuit time constants as well as leakage inductance and stator resistance. Not all of these parameters are needed for the synchronous generator model currently implemented in the phasor-framework. However, the data format gives the option to extend the synchronous generator model in the future without the need for modifying the data format.

The synchronous generator model implemented in this framework needs to be fed with so called fundamental parameters that are different from the standard parameters. The fundamental parameters are the physical parameters that are deduced from a physical modeling of the internal processes within the generator. The standard parameters are a combination of basic machine data like to the nominal power and parameters that are derived from measurement results. Therefore, the standard parameters, that are given as input parameters to the model, need to be converted into the fundamental parameters. For this, the calculations based on [34] are used. There are various methods on how to compute the fundamental parameters from the standard parameters. Therefore, the formulation of this dependence used in the synchronous generator model implemented in the phasor-framework is shown in the following paragraph.

First of all, the rated angular velocity of the rotor $\omega_{0\mathrm{m}}$ in mechanical radians per second is calculated as

$$w_{0\mathrm{m}} = 2\pi \frac{n_{\mathrm{base}}}{60} \tag{4.17}$$

The rated angular velocity of the rotor ω_{base} in electrical radians per second is

$$w_{\mathrm{base}} = 2\pi \frac{n_{\mathrm{base}}}{60} p \tag{4.18}$$

As the per unit speed of the machine is 1, the leakage reactance and leakage inductance are equal, thus

$$l_\ell = x_\ell \tag{4.19}$$

The mutual unsaturated inductances are

$$l_{\mathrm{adu}} = x_{\mathrm{d}} - x_\ell \tag{4.20}$$

$$l_{\mathrm{aqu}} = x_{\mathrm{q}} - x_\ell \tag{4.21}$$

Table 4.1: Input data format for synchronous generator (SG). OC=open circuit, SC=short curcuit

Name	Unit	Description	Name	Unit	Description
Bus		Bus number SG is connected to	t'_{d0}	s	OC d-axis transient time constant
VA_{base}	MVA	Base power of SG parameters	t'_{q0}	s	OC q-axis transient time constant
V_{base}	kV	Base voltage of SG parameters	t''_{d0}	s	OC d-axis subtransient time constant
n_{base}	rev/min	Base speed	t''_{q0}	s	OC q-axis subtransient time constant
V_{ini}	pu	Initial voltage at SG terminal	t'_{d}	s	SC d-axis transient time constant
p		Number of pole pairs	t'_{q}	s	SC q-axis transient time constant
sat	%	Saturation in %	t''_{d}	s	SC d-axis subtransient time constant
x_{d}	pu	Synchronous d-axis reactance	t''_{q}	s	SC d-axis subtransient time constant
x_{q}	pu	Synchronous q-axis reactance	r_{a}	pu	Resistance of the stator
x'_{d}	pu	Transient d-axis reactance	x_{ℓ}	pu	Leakage inductance of stator
x'_{q}	pu	Transient q-axis reactance	k_{D}		Damping
x''_{d}	pu	Subtransient d-axis reactance	H	s	Inertia constant
x''_{q}	pu	Subtransient q-axis reactance	J	kgm^2	Moment of inertia (optional because it depends of H)

From this the saturated values are calculated

$$l_{\mathrm{ad}} = l_{\mathrm{adu}} \cdot sat \tag{4.22}$$
$$l_{\mathrm{aq}} = l_{\mathrm{aqu}} \cdot sat \tag{4.23}$$

With this, the d- and q-axis inductances are

$$l_{\mathrm{d}} = l_{\mathrm{ad}} + l_{\ell} \tag{4.24}$$
$$l_{\mathrm{q}} = l_{\mathrm{aq}} + l_{\ell} \tag{4.25}$$

Again, the reactance equal the inductances because the per unit speed is 1, thus

$$X_{\mathrm{d}} = l_{\mathrm{d}} \tag{4.26}$$
$$X_{\mathrm{q}} = l_{\mathrm{q}} \tag{4.27}$$
$$X_{\mathrm{ad}} = l_{\mathrm{ad}} \tag{4.28}$$

The rotor circuit per unit leakage inductances are

$$l_{\mathrm{fd}} = 1/(l_{\mathrm{ad}}/(x'_{\mathrm{d}} - x_{\ell}) - 1) \cdot l_{\mathrm{ad}} \tag{4.29}$$
$$l_{\mathrm{1q}} = 1/(l_{\mathrm{aq}}/(x'_{\mathrm{q}} - x_{\ell}) - 1) \cdot l_{\mathrm{aq}} \tag{4.30}$$
$$l_{\mathrm{1d}} = 1/(l_{\mathrm{ad}} \cdot lfd/(x''_{\mathrm{d}} - x_{\ell}) - l_{\mathrm{fd}} - l_{\mathrm{ad}}) \cdot l_{\mathrm{ad}} \cdot l_{\mathrm{fd}} \tag{4.31}$$
$$l_{\mathrm{2q}} = 1/(l_{\mathrm{aq}} \cdot l_{\mathrm{1q}}/(x''_{\mathrm{q}} - x_{\ell}) - l_{\mathrm{1q}} - l_{\mathrm{aq}}) \cdot l_{\mathrm{aq}} \cdot l_{\mathrm{1q}} \tag{4.32}$$

From this the leakage inductances can be calculated

$$l_{\mathrm{11d}} = l_{\mathrm{ad}} + l_{\mathrm{1d}} \tag{4.33}$$
$$l_{\mathrm{11q}} = l_{\mathrm{aq}} + l_{\mathrm{1q}} \tag{4.34}$$
$$l_{\mathrm{ffd}} = l_{\mathrm{ad}} + l_{\mathrm{fd}} \tag{4.35}$$

The rotor resistances are

$$r_{\mathrm{fd}} = (l_{\mathrm{ad}} + l_{\mathrm{fd}})/(t'_{\mathrm{d0}} \cdot w_{\mathrm{base}}) \tag{4.36}$$
$$r_{\mathrm{1d}} = 1/(t''_{\mathrm{d0}} \cdot w_{\mathrm{base}}) \cdot (l_{\mathrm{1d}} + l_{\mathrm{ad}} \cdot l_{\mathrm{fd}}/(l_{\mathrm{ad}} + l_{\mathrm{fd}})) \tag{4.37}$$
$$r_{\mathrm{1q}} = (l_{\mathrm{aq}} + l_{\mathrm{1q}})/(t'_{\mathrm{q0}} \cdot w_{\mathrm{base}}) \tag{4.38}$$
$$r_{\mathrm{2q}} = 1/(t''_{\mathrm{q0}} \cdot w_{\mathrm{base}}) \cdot (l_{\mathrm{2q}} + l_{\mathrm{aq}} \cdot l_{\mathrm{1q}}/(l_{\mathrm{aq}} + l_{\mathrm{1q}})) \tag{4.39}$$

4.2.5 Initialization

In the pre power flow initialization routine, the generator data stored in mpc.SG is transferred to the static input data in mpc.gen. With this the power flow can be conducted and the terminal voltage $\underline{E}_{\mathrm{t}}$, the terminal current $\underline{I}_{\mathrm{t}}$, terminal active power P_{t} and terminal reactive power Q_{t} are obtained. With the help of these power flow results, the integrators of the mechanical and electrical blocks are initialized. The calculation procedure that is necessary for that is implemented in the post power flow routine and briefly explained in the following paragraph. The procedure is based on [34]. This description is intended to give the reader a comprehensible step by step guidance on the approach used within the initialization routine in the phasor-framework. Furthermore, the implemented and presented initialization routine is also applicable to higher order synchronous generator models and helps a future component developer to implement a higher order synchronous generator model.

In the post power flow initialization routine, the base value of the torque in Nm is calculated first. Therefore, the general physical relationship $P = \omega T$ between power P, speed ω and torque T is used to calculate the base torque. It is

$$T_{\text{base}} = \frac{\text{VA}_{\text{base}} \cdot 10^6}{\omega_{0\text{m}}} \tag{4.40}$$

where it is considered that the unit of the base power is MW. The RMS line-to-neutral base voltage in kV is

$$E_{\text{s, base}} = V_{\text{base}}/\sqrt{3}; \tag{4.41}$$

The line-to-neutral peak voltage in kV is

$$e_{\text{s, base}} = V_{\text{base}}\sqrt{2/3}; \tag{4.42}$$

The line-to-neutral base current is

$$I_{\text{s, base}} = VA_{\text{base}}/(3E_{\text{s, base}}); \tag{4.43}$$

and its peak values is

$$i_{\text{s, base}} = I_{\text{s, base}}\sqrt{2}; \tag{4.44}$$

From this, the load angle at the terminal is

$$\varphi = \angle \underline{E}_{\text{t}} - \angle \underline{I}_{\text{t}} \tag{4.45}$$

The internal rotor angle can be calculated as

$$\delta_i = \arctan\left(\frac{X_{\text{q}} I_{\text{t}} \cos(\varphi) - r_a I_{\text{t}} \sin(\varphi)}{E_{\text{t}} + r_a I_{\text{t}} \cos(\varphi) + I_{\text{t}} X_{\text{q}} \sin(\varphi)}\right) \tag{4.46}$$

The dq components of the initial terminal voltage and current are calculated from the RMS terminal current and voltage and from the rotor angle.

$$e_{\text{d}} = E_{\text{t}} \sin(\delta_i) \tag{4.47}$$

$$e_{\text{q}} = E_{\text{t}} \cos(\delta_i) \tag{4.48}$$

$$i_{\text{d}} = E_{\text{t}} \sin(\delta_i + \varphi) \tag{4.49}$$

$$i_{\text{q}} = E_{\text{t}} \cos(\delta_i + \varphi) \tag{4.50}$$

The current i_{fd} and voltage e_{fd} at the field winding is

$$i_{\text{fd}} = \frac{e_{\text{q}} + r_{\text{a}} i_{\text{q}} + X_{\text{d}} i_{\text{d}}}{X_{\text{ad}}} \tag{4.51}$$

$$e_{\text{fd}} = r_{\text{fd}} i_{\text{fd}} \tag{4.52}$$

From this, the flux linkages can be calculated

$$\psi_{\text{fd}} = (l_{\text{ad}} + l_{\text{fd}}) i_{\text{fd}} - l_{\text{ad}} i_{\text{d}} \tag{4.53}$$

$$\psi_{1\text{d}} = l_{\text{ad}}(i_{\text{fd}} - i_{\text{d}}) \tag{4.54}$$

$$\psi_{1\mathrm{q}} = -l_{\mathrm{aq}} i_{\mathrm{q}} \tag{4.55}$$

$$\psi_{2\mathrm{q}} = \psi_{1\mathrm{q}} \tag{4.56}$$

The flux linkages are needed for initializing the electrical synchronous generator equations. Thus, ψ_{fd} calculated in (4.53) is the initial vale for the integrator in Fig. 4.2. The other flux linkages are not needed for the synchronous generator model currently implemented in the phasor-framework. However, the equations are shown in order to give the guidance for initializing a higher order synchronous generator model. The damping currents are zero at steady state

$$i_{1\mathrm{d}} = 0 \tag{4.57}$$

$$i_{1\mathrm{q}} = 0 \tag{4.58}$$

$$i_{2\mathrm{q}} = 0 \tag{4.59}$$

The electrical torque in per unit quantities that is applied at the initial state is

$$T_{\mathrm{e}} = P_{\mathrm{t}} + I_{\mathrm{t}}^2 \cdot r_{\mathrm{a}} \tag{4.60}$$

and the torque in absolute values, nameley in 10^6N m is

$$T_{\mathrm{e,\ abs}} = T_{\mathrm{e}} \cdot T_{\mathrm{base}} \tag{4.61}$$

The rotor angle δ is computed in as shown in Fig. 4.3 as the output of an integrator. Its initial value $\delta_{i,0}$ is

$$\delta_{i,0} = \alpha - \frac{\pi}{2} + \delta_i \tag{4.62}$$

with α being the electrical angle of the terminal voltage phasor

$$\alpha = \angle \underline{E}_{\mathrm{t}} \tag{4.63}$$

The speed ω_r is also the output of an integrator as shown in Fig. 4.3. The initial value of this integrator therefore determined by the initial speed of the machine. This initial mechanical machine speed can be set by the user as needed.

4.3 Diesel generator

The diesel generator is, as of now, the only governor model that is implemented in the RMS-Framework. The diesel model was implemented because the study that is done in chapter 5 is based on a diesel governor as grid forming unit. However, the phasor-framework is designed in such a way, that other governor models can be implemented as well.

The model of the diesel generator implemented in the phasor-framework is displayed in Fig. 4.5. It is based on the model used in [66, 67, 68] and is complemented with a frequency control option. The main part of the model (upper part of Fig. 4.5) consists of an electric control box, an actuator model and an engine model. The parameters used in this work can be found in Table 4.2.

The frequency control (lower part of Fig. 4.5), which is referred to as f(P) control, is designed according to Fig. 4.6. This design is already adjusted to the case study performed in Chapter 5. For different case studies it can, of course, be adjusted. The f(P) characteristic implemented in the current model (Fig. 4.5) works as follows: If the mechanical output power $\omega_N T_m$ is above a threshold P_{set}, the boolean signal (orange, dashed and dotted line) is zero and $\Delta f_{\text{ref}} = 0$. Thus, the reference frequency f_{ref} is not changed. If $\omega_N T_m \leq P_{\text{set}}$, the boolean signal (orange, dashed-dotted line) is one and the reference frequency f_{ref} is changed by the value

$$\Delta f_{\text{ref}} = (\omega_N T_m - P_{\text{set}}) \cdot \text{Droop}. \tag{4.64}$$

where T_m, P_{set}, Droop and Δf_{ref} are expressed in per unit. T_m is the mechanical output torque of the diesel generator, f the frequency at the point of common coupling and Δf_{ref} is the deviation from the reference speed of the diesel generator.

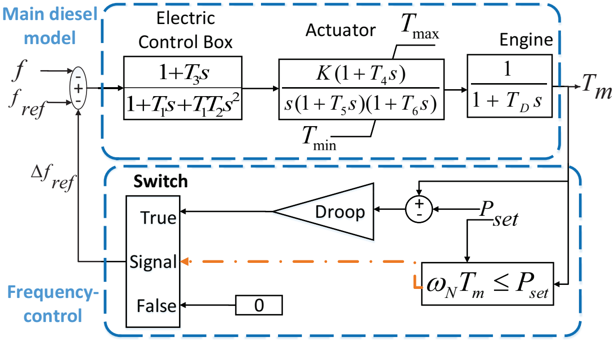

Figure 4.5: Block diagram of diesel generator. Note that all variables are in per unit.

Table 4.2: Parameters of the diesel generator

Parameter	Value	Parameter	Value
T_1	0.2 s	K	0.01
T_2	0.1 s	T_D	0.01 s
T_3	0.5 s	$T_{\min}$	0 pu
T_4	1 s	$T_{\max}$	1.1 pu
T_5	0.1 s	Droop	−0.0375 Hz/kW
T_6	0.2 s		

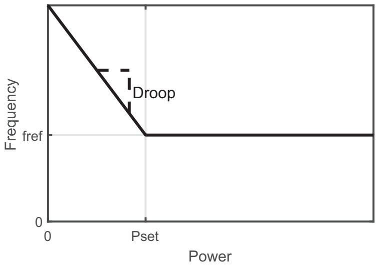

Figure 4.6: Diesel generator droop characteristics.

By defining P_{set} and Droop accordingly, the desired f(P) behavior can be chosen. Here, ω_N is the nominal rotational speed of the synchronous generator shaft in per unit. As the rotational speed of the generator shaft is $\omega \approx 1$ under normal operating conditions, the error that is made for the calculation of the mechanical output power is negligible. It has to be noted that the model is therefore not suitable for rotational speeds that deviate significantly from the nominal speed.

4.4 Photovoltaic system

4.4.1 Introduction to photovoltaic system modeling

In recent years the complexity of medium and low-voltage power grids increased significantly due to a rise of distributed generation such as wind and solar power [69]. Photovoltaic (PV) systems have a large share of the total installed capacity. The worldwide installed photovoltaic capacity has reached 300 GW in 2016 [70]. Small residential photovoltaic systems represent a major portion of the total installed capacity in Europe [71]. For example, in Germany, about 65 % of the installed photovoltaic capacity is located in the low-voltage grid [72]. The installed photovoltaic capacity is expected to increase in the future due to photovoltaic cost reduction [71]. An investigation on the improved grid integration of photovoltaic systems in Germany can be found in [73]. A techno-economic assessment of $Q(V)$ and $P(V)$ control can be found in [74]. An approach for the static simulation of photovoltaic systems can be found in [75]. The dynamic behavior of the voltage dependent reactive power injection of photovoltaic inverters according to different $Q(V)$ characteristics has been thoroughly investigated, e.g., in [76] and [77].

Because of the increasing presence of photovoltaic systems in the low-voltage level, it becomes important to study the dynamic behavior of photovoltaic systems at the low-voltage level. Dedicated photovoltaic models are required for dynamic studies.

The goal of this section is to develop a model of a small-scale photovoltaic inverter suited for stability studies in a time range of several seconds up to minutes. The focus of this work lays on the modeling of the dynamic $Q(V)$ behavior and on the modeling of the dynamic $P(V)$ behavior, even though the $P(V)$ functionality is not yet part of low-voltage grid codes in Germany. The $P(V)$ and $Q(V)$ behaviors are implemented in a vectorized fashion in Simulink. Furthermore the photovoltaic model includes a dynamic $P(f)$ behavior. The underlying $P(f)$ dynamics that are implemented are mostly based on requirements defined in the German LV grid code VDE 4105 [78]. Thus, the photovoltaic model lowers its output power, according to a P(f) characteristics, if the frequency rises above 50.2 Hz. The implementation of the P(f) characteristic is done with a Stateflow® diagram. The usage of Stateflow is a very nice way to simplify model development. Furthermore, the integration of Stateflow models within the phasor-framework is a good example for the flexibility of the phasor-framework.

A lab experiment is done in which the behavior of a real off-the-shelf inverter is compared with the MATLAB/Simulink model. Furthermore, the scalability of the developed model is shown with a dynamic study of a real German low-voltage network with several photovoltaic systems.

The section is structured as follows: In Section 4.4.2 the generic WECC model is briefly introduced as it serves as a basic foundation for the photovoltaic model developed within this thesis. Furthermore the changes and extensions that are incorporated, based on the WECC model, are explained. An overview of all blocks that are contained in the developed photovoltaic model are presented in Section 4.4.3. The frequency dependent active power injection is descibed in Section 4.4.4. The initialization of the PV model is described in section 4.4.5. A laboratory validation is conducted in Section 4.4.6 .

4.4.2 Model basis - the generic WECC model

Various photovoltaic system models can be found in, e.g., [76], [77] and [28]. The simulation model developed in this work is based on the generic model for distributed and small photovoltaic systems provided by the Western Electricity Coordinating Council (WECC) Renewable Energy Modeling Task Force [79].

The advantages of such generic models are: They are independent of the manufacturer and the vendor, they are compatible with grid codes, their model structure is open source and the model itself is simulation platform independent [80]. Note that WECC has also developed a model that is suited for large-scale photovoltaic systems. This model is more detailed but due to the complex control not of interest in this work. A DIgSILENT PowerFactory® implementation of a large-scale photovoltaic system model can be found in [81].

The model structure of the generic model for distributed and small photovoltaic systems provided by WECC was specifically developed to represent photovoltaic systems which are connected to the distribution grid. Its two main features that are of interest in this work, are:

- It consists of an average model (two first order delays) for representing the dynamics of inverter currents I_p and I_q. The rise time for a standard inverter is usually in the range of 20 ms.

- Furthermore, the model contains a voltage dependent reactive power characteristic for volt/var control, also called $Q(V)$ characteristics. Typical parameters for $Q(V)$ characteristics in the high voltage level can be found in dedicated grid codes, e.g., in [82]. For the low-voltage level, rules are also discussed in the draft from 2017 for the German low-voltage grid code [83].

The small-scale photovoltaic model of WECC lacks some functionalities that are of interest in this work. Therefore, the following capabilities have been added to the model:

1. A ramp rate limiter for the power output is added. In state-of-the-art inverters these rate limiters can be configured via a web interface of the real inverter. Therefore, it is important to include this feature in the model.

2. As voltage dependent reduction of active power injection (volt/watt control or $P(V)$) could be beneficial in the future [84], this feature is added to the PV system model. In case of a high voltage at the grid coupling point, a $P(V)$ characteristic allows to reduce the injected active power with regard to the terminal voltage. A typical $P(V)$ characteristic was already given in 3.1g. 2.3a. The reduction in injected active power is realized in the inverter by leaving the Maximum Power Point (MPP).

3. A representation of the voltage measurement is added. The measurement takes place in the time range of up to 5 cycles.

4. A detailed representation of the dynamics of the frequency dependent active power injection $P(f)$ with different model states. This functionality will be explained in detail in section 4.4.4.

4.4.3 Model overview

The most important WECC functionalities for the investigations in this work, as introduced in section 4.4.2 are implemented as a basis for the photovoltaic model. After that, the four additional capabilities mentioned in Section 4.4.2 are added.

The structure of the complete photovoltaic model is displayed in Fig. 4.7. It is implemented in MATLAB/Simulink and included in the phasor-framework. The inputs are the complex bus voltage $\underline{V}$ and the system frequency f. The output is the injected complex bus current $\underline{I}$. Furthermore, the model contains an input for a time series of available photovoltaic power P_{avail}.

The main parts of the model are an emulation of the voltage and frequency measurement, a dynamic model of voltage dependent active and reactive power injection, a dynamic model of the frequency dependent active power injection and a simplified model of the physical inverter.

The data format for the photovoltaic model is displayed in Table 4.3. The variables are stored in a table in the field mpc.PV.

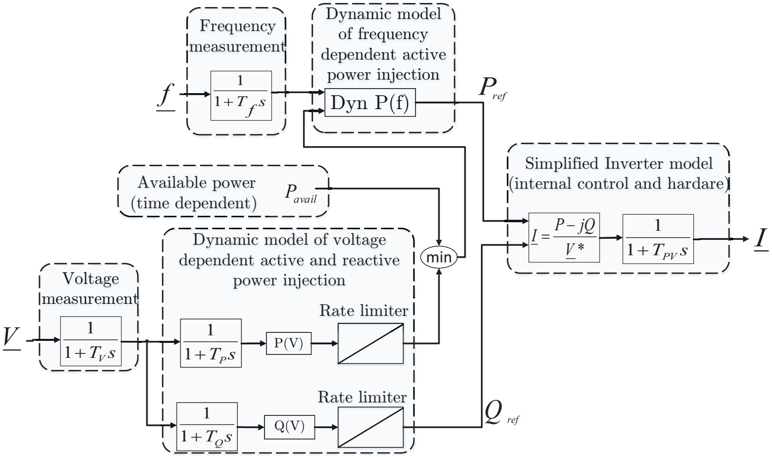
Frequency measurement
$\frac{1}{1+T_f s}$
f
Dynamic model of frequency dependent active power injection
Dyn P(f)
P_{ref}
Simplified Inverter model (internal control and hardare)
$\underline{I} = \frac{P-jQ}{\underline{V}^*}$
$\frac{1}{1+T_{PV} s}$
$\underline{I}$
Available power (time dependent)
P_{avail}
min
Dynamic model of voltage dependent active and reactive power injection
Voltage measurement
$\frac{1}{1+T_V s}$
$\underline{V}$
Rate limiter
$\frac{1}{1+T_P s}$
P(V)
Rate limiter
$\frac{1}{1+T_Q s}$
Q(V)
Q_{ref}

Figure 4.7: Overview of the developed small-scale photovoltaic model for low-voltage grids which is implemented in the phasor-framework.

The frequency is measurement is emulated with a first order transfer function with a rise time of 20 ms which can be configured via T_f. This is a low-pass filter that is applied to the frequency of the reference generator. Local differences of the frequency are not considered. This could, however, be modified in the future if a RMS model of a phase-locked loop (PLL) is implemented.

The model of the voltage measurement consists of a first order time delay. The first order time delay emulates the calculation of the moving RMS value. In recent photovoltaic inverters, five grid periods are used for calculation of the RMS value. As a 50 Hz system is considered, a rise time of 100 ms is chosen in this work.

The measured voltage is fed into the dynamic model of the voltage dependent active and reactive power injection. Based on the voltage, active and reactive power setpoints are calculated. These setpoints are delayed by T_P and T_Q which are also called set-up times. T_P represents the set-up time of the voltage dependent active power and T_Q represents the set-up time of the voltage dependent reactive power. These parameters determine how fast the inverter changes its active and reactive power injection setpoint after a change of the terminal voltage occurs. These time delays are typically manually configured in the web interface of a state-of-the-art inverter. They are typically set in the range of few seconds up to minutes. After the first order time delays, the $P(V)$ and $Q(V)$ characteristics are placed. Examples for these characteristics were already shown in Fig 2.3a and Fig 2.3b in chapter 2. In the photovoltaic model for the phasor-framework, a vectorized implementation of (2.1) is used. For example, the $Q(V)$ characteristic is implemented as a vectorized version of

$$Q(V) = \begin{cases} Q_1, & V \leq V_1 \\ \frac{Q_2-Q_1}{V_2-V_1}V + Q_2 - V_2\frac{Q_2-Q_1}{V_2-V_1}, & V_1 < V < V_2 \\ Q_2, & V_2 \leq V \leq V_3 \\ \frac{Q_3-Q_2}{V_4-V_3}V + Q_3 - V_4\frac{Q_3-Q_2}{V_4-V_3}, & V_3 < V < V_4 \\ Q_3, & V_4 \leq V. \end{cases} \tag{4.65}$$

Table 4.3: Input data format for photovoltaic model.

Name	Unit	Description
Bus	/	Bus number photovoltaic system is connected to
Pn	pu	Nominal power
Radiation	%	Radiation
		Initialization
p_ini	pu	Initial active power injection
q_ini	pu	Initial reactive power injection
		Measurements
T_V	s	Time constant for voltage measurement
T_f	s	Time constant for frequency measurement
		Voltage dependent active and reactive power
PV_enable	/	Activation (1) or deactivation (0) of voltage dependent active power injection
T_P	s	Time constant for dynamic $P(V)$ injection
p_chara_v	pu	Voltage values [V1 V2 V3 V4] of P(V) according to Fig. 2.1
p_chara_p	pu	Active power values [P1 P2 P3] of P(V)according to Fig. 2.1
RateLimRise_p	pu	Positive rate of change limit for active power setpoint
RateLimFall_p	pu	Negative rate of change limit for active power setpoint
QV_enable	/	Activation (1) or deactivation (0) of voltage dependent reactive power injection
T_Q	s	Time constant for dynamic $Q(V)$ injection
q_chara_v	pu	Voltage values [V1 V2 V3 V4] of Q(V) according to Fig. 2.1
q_chara_q	pu	Reactive power values [P1 P2 P3] of Q(V) according to Fig. 2.1
RateLimChara_q	pu	Positive rate of change limit for active power setpoint
RateLim_q	pu	Negative rate of change limit for reactive power setpoint
maxCosPhi		Maximum cos(phi)
		Frequency dependent active power
P_f_behavior	/	Behavior of frequency dependent active power injection. Possible are settings ’VDE_4105’ or fixed frequency settings like ’50.2’ or ’50.3’ (see Section 4.4.4)
		Inverter
T_PV	s	Inverter time constant

The model of the voltage dependent active and reactive power injection also include rate limiters. These limit the positive and negative rate of change of the active and reactive powers and can also be configured in the web interface of the inverter. Thus, they are also part of the photovoltaic models input data.

The reactive power setpoint is fed straight forward into the inverter. It is assumed, that the rating of the inverter is such that all reactive power setpoints that are calculated by the $Q(V)$ characteristic can be reached by the inverter. For that, the parametrization of the $Q(V)$ characteristics has to be done in accordance with the inverter's power rating.

The output of the $P(V)$ characteristics is purely dependent on the voltage and does not consider the available active power. Thus, it may be higher than the available power. Therefore, the output of the $P(V)$ characteristic is compared to the available active power P_{avail}. The minimum of both values is fed into the *Dyn P(f)* block. In this block, the active power setpoint P_{ref} for the inverter is calculated based on the frequency.

The inverter controls the output current such that the active and reactive power setpoints are met. First of all the current setpoint is calculated based on the active and reactive power setpoints. The physical inverter is modeled according to an average model with a first order transfer function with time constant $T_{\mathbf{PV}}$. As stated, e.g., in [85], this time constant can be estimated to be around 20 ms. A more detailed inverter model, based on EMT, would for example include a pulse width modulation. However, such detailed description is not necessary here as they are not relevant for the timescale of the dynamic studies in this work, which are in the range of seconds up to minutes.

It has to be noted that the developed photovoltaic model is suited for RMS simulations in the range of seconds up to minutes. It does not include effects of electromagnetic transients (EMT), such as inverter switching. Furthermore, this model does not include LV fault ride-through behavior as it is not mandatory for LV connected photovoltaic systems yet [86]. However, this could be included in a future version of the model.

4.4.4 Frequency dependent active power injection

Included in the dyn. P(f) block in Fig. 4.7, is a model for the frequency dependent active power reduction of photovoltaic systems as well as a model for the reconnection behavior. The active power reduction and reconnection behavior were implemented such that two options can be chosen. One option is to choose a behavior according to VDE 4105 from 2011 [78] (new system). For photovoltaic systems that went into operation prior to 2011, a modified behavior can be chosen (old systems). From now on, these two types of photovoltaic system models are referred as new and old photovoltaic systems.

New photovoltaic systems

The behavior of new photovoltaic systems is described in [78]. In the following list, the properties, relevant for the studies conducted in this work, are described:

- The photovoltaic system is reconnected if the frequency is in the range $47.5\,\text{Hz} \leq f \leq 50.05\,\text{Hz}$ for a duration of 60 s.
- During the first 10 min of the reconnection process, the output power is limited. The limit is time varying according to

$$P_{\text{lim,new}} = \frac{10\,\%P_n}{\text{min}} \cdot t \tag{4.66}$$

  where P_n is the nominal inverter power.

- At the instant $\tilde{t}$, at which the frequency exceeds 50.2 Hz, the present active power output is stored in the variable $P_M = P_{\text{ref}}(\tilde{t})$. If the frequency rises above 50.2 Hz, the output power is limited as displayed in Fig. 4.8. This can be expressed via a power limit $P_{\text{lim,new}}$ that varies with the frequency according to

$$P_{\text{lim,new}} = P_M - \frac{0.4}{\text{Hz}} \cdot P_M\,(f - 50.2\,\text{Hz}) \tag{4.67}$$

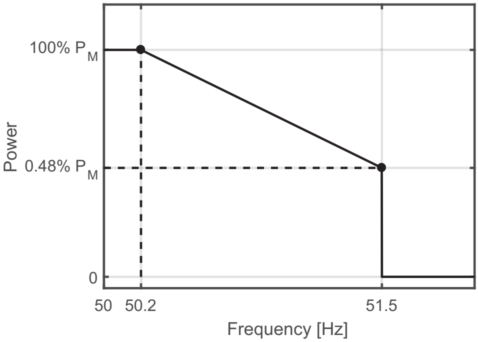

Figure 4.8: Frequency dependent active power limitation of photovoltaic systems according to [78]. P_M is the output power of the photovoltaic system at the instant, at which the frequency exceeds 50.2 Hz. The upper limit of the output power is reduced by 40 % P_M/Hz. The output power of the photovoltaic system is limited as long as the frequency is above 50.2 Hz.

- If the frequency falls again below 50.2 Hz, and the available power is above P_M, the maximum allowable output power of the photovoltaic system can only increase with $^{10\,\%P_n}/_{\mathrm{min}}$ until the available power is reached.
- The P(f) behavior according to [78] is implemented in the simulation via a Stateflow® diagram in Simulink, as illustrated in Fig. 4.9. The implementation consists of the four states Normal operation, Active power reduction, Disconnected and Reconnection. A transition from one state to another is triggered as soon as a transition condition is fulfilled. For example, a transition from the state Reconnection to the state Disconnected occurs if the frequency exceeds 51.5 Hz.

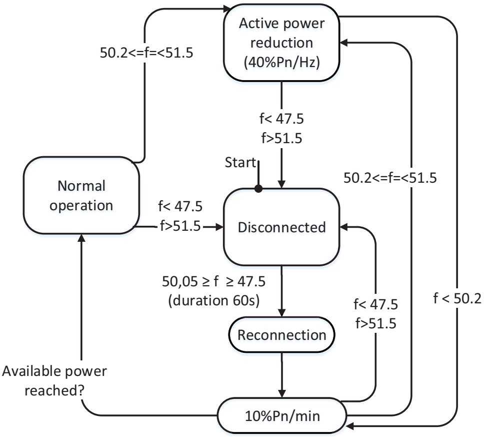

Figure 4.9: State diagram of the P(f) portion of the model of a new photovoltaic system.

Old photovoltaic systems

The behavior of inverter coupled systems in LV grids is not well defined for systems that are older than 2011. For example the German grid code VDEW [87] from 2001 defines no behavior for active power reduction in case of over frequency. Also, no reconnection behavior is defined. PV systems that were larger then 10 kWp and started operating after September 2005 have mostly been retrofitted such that they disconnect within 20 ms if the frequency is above 50.2 Hz. More recently another retrofit took place in which the cut-off frequencies of older photovoltaic systems was updated such that the disconnection of all installed photovoltaic systems in Germany occurs equally distributed between 50.2 Hz and 51.5 Hz. The cut-off frequency of all three types of old photovoltaic systems can be modeled with the PV system model developed in this thesis. This is done by a variable cut-off frequency that can be adjusted in the data input of the model.

Furthermore, the reconnection behavior of old PV systems was modeled based on information from industry experts, which resulted in the following assumed behaviors:

- After disconnection of the photovoltaic system, the system is allowed to reconnect to the network whenever the frequency is in the range of $47.5 \leq f \leq 50.05\,\text{Hz}$ for 40 s.

- After reconnection, the output power is limited with a time varying maximum power of
$$P_{\text{lim,old}} = \frac{25\,\% P_n}{\text{s}} \cdot t \tag{4.68}$$
for the first 4 seconds. Thus, the full photovoltaic infeed is reached after 4 s.

- The implementation of the P(f) behavior of photovoltaic systems produced before year 2011 is displayed in Fig. 4.10. The main difference to Fig. 4.9 is the lack of the state Active power reduction. Instead of that, the model changes its state from Normal operation to Disconnected if the frequency increases above a configurable cut-off frequency $f_{\text{cut-off}}$.

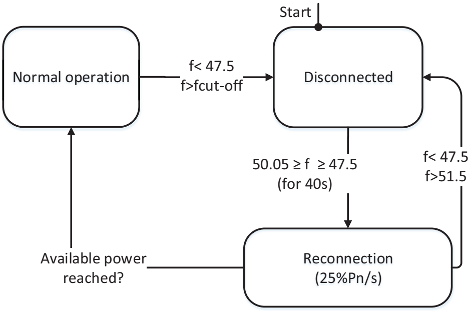

Figure 4.10: State diagram of the P(f) portion of the model of an old photovoltaic system.

4.4.5 Initialization

During the pre-power-flow initialization routine (script (b) in Fig. 3.1), the data from the photovoltaic model is processed such that the photovoltaic model is taken into account during the power flow. Therefore, the settings from the $P(V)$ and $Q(V)$ characteristic are transferred to the static portion of the input data of the phasor-framework, namely into the field mpc.PQULoad. The input data structure was displayed in Table 3.3.

In the post-power-flow initialization routine the initial active and reactive power injections of each photovoltaic system are copied to the initial values of the integrators of the photovoltaic model and to the initial values of the $P(V)$ and $Q(V)$ part of the model (Fig. 4.7 for model overview).

4.4.6 Model testing against real-life inverter

The voltage dependent active and reactive power injection functionality of the developed photovoltaic model was tested against a specific setting in a real-world inverter. For this, a lab setup was established in which the response of the inverter to different voltage variations was measured. In the following section a system overview is given. After that, the steady state working point is validated with the simulation model. After that, the dynamic $Q(V)$ and $P(V)$ behavior of the real inverter is compared with the simulation model. The lab setup was modeled within the phasor-framework and the simulations were performed with the photovoltaic model described in the previous sections.

System overview

Fig. 4.11 shows the general laboratory setup. It consists of a photovoltaic system, a cable and a voltage source, which represents a slack bus. The photovoltaic inverter is connected to two emulators of solar strings shown in Fig. 4.12a. The inverter is connected to a programmable AC voltage source, shown in Fig. 4.12b, via a cable.

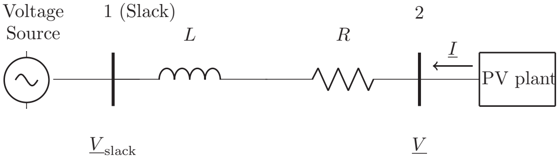

Figure 4.11: Laboratory setup for testing the small-scale photovoltaic system model.

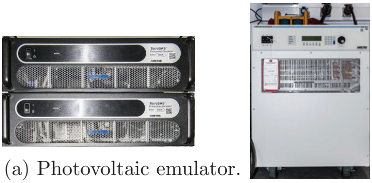

(a) Photovoltaic emulator.

(b) AC source

Figure 4.12: Devices used for the laboratory setup.

Due to the cable, grid feedback occurs. That means, that the output current of the inverter influences the terminal voltage at of the inverter.

Another option for a lab setup would have been to omit the cable and directly connect the voltage source to the inverter. In this case, the voltage at the inverter terminal would have been dictated by the voltage source and no grid feedback would have occurred. For the simulation this would have meant that no grid simulation would have been necessary for the validation of the photovoltaic model. However, to have the cable within the lab setup makes the whole system more realistic and gives the opportunity to also validate grid equations of the phasor-framework with a real setup.

The AC voltage source is capable of performing voltage steps within the grid period after the voltage command is issued. This can be seen in Fig. 4.13, were a voltage step command from $V \approx 247\,\mathrm{V}$ to $V \approx 262\,\mathrm{V}$ is given to the voltage source at $t \approx 35\,\mathrm{ms}$. It can be seen that the new voltage setpoint is already reached in the first half cycle after the command was issued.

The inverter used within this laboratory experiment has a nominal power of 5000 VA. It has a convenient configurable web interface through which various parameters can be configured. The cable, that connects the inverter and the grid emulator, has an inductance of $L = 2.63\,\mathrm{mH}$ and a resistance between $R = 700\,\mathrm{m\Omega}$ and $R = 1200\,\mathrm{m\Omega}$, depending on its temperature. To have a valid resistor value, the resistor was measured before each experiment. In this way, it was not necessary to measure the temperature of the caple. The resistance corresponds to an R/X ration between 0.85 and 1.45 which is also a realistic for low-voltage grids.

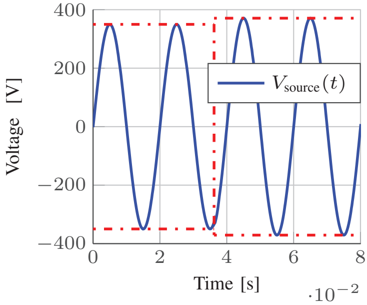

Figure 4.13: AC source performing a voltage step

Steady state

To perform a steady state comparison of the photovoltaic system model, the simulation results of the phasor-framework are compared to measurement results from the laboratory setup. The investigation is done in two parts.

In the first part, $Q(V)$ and $P(V)$ characteristics are configured into the web interface of the inverter and compared to measurement results. Theoretically, the measured characteristics should correspond the the characteristics configured in the inverter. However, this was not the case and therefore, an adjustment had to be made in the simulation model. The reason for the difference between the measured and configured characteristic is unclear. As only one inverter was tested it could not be found out if other inverters have this difference as well. The $Q(V)$ and $P(V)$ characteristics shown in the first and second line of Table 4.4 are configured into the inverter. The voltage values V_1, V_2, V_3, V_4 correspond to the voltage values given in Fig. 2.1. The active power values P_1, P_2, P_3 and the reactive power values Q_1, Q_2, Q_3 correspond the variables y_1, y_2, y_3 in Fig. 2.1. With these values a $P(V)$ and $Q(V)$ characteristic is obtained. These parameters are entered into the configurable web interface of the inverter. For the laboratory investigation the inverter is directly connected to the voltage source and the voltage output at the voltage source is varied. In order to validate the steady state behavior of the inverter, the $P(V)$ and $Q(V)$ characteristics have been measured and compared to the configured characteristic. Hence, the inverter's injected active and reactive powers have been measured for various terminal voltages. Fig. 4.14a shows the measured and configured reactive power injection $Q(V)$ of the inverter against the terminal voltage magnitude. It can be seen that there is a small offset between both curves. As the simulation model needs to emulate the correct steady state behavior, the settings for the $Q(V)$ characteristic were adjusted in the photovoltaic model to match the measured values. Fig. 4.14b shows the adjusted characteristic together with the measured characteristic. It can be seen that they coincide. The same procedure is done for the $P(V)$ characteristic. The adjusted parameters used in the simulation model for both, $Q(V)$ and $P(V)$ characteristic are shown in the third and fourth line of Table 4.4 .

In the next step, the steady state operation points of the inverter are compared with the simulation model after the $P(V)$ and $Q(V)$ characteristics were adjusted according to Table 4.4. For that the setup as described above and seen in Fig. 4.11

Table 4.4: Original and adjusted setpoints of the active and reactive power characteristics

Configured in	$\begin{bmatrix}V_1 & V_2 & V_3 & V_4\end{bmatrix}$	$=$	$\begin{bmatrix}0.960 & 0.980 & 1.020 & 1.040\end{bmatrix}$ pu
Inverter $Q(V)$	$\begin{bmatrix}Q_1 & Q_2 & Q_3\end{bmatrix}$	$=$	$\begin{bmatrix}-2.5 & 0 & 2.5\end{bmatrix}$ kVar
Configured in	$\begin{bmatrix}V_1 & V_2 & V_3 & V_4\end{bmatrix}$	$=$	$\begin{bmatrix}0.964 & 0.985 & 1.024 & 1.045\end{bmatrix}$ pu
Inverter $P(V)$	$\begin{bmatrix}Q_1 & Q_2 & Q_3\end{bmatrix}$	$=$	$\begin{bmatrix}-2.337 & -0.05 & 2.21\end{bmatrix}$ kVar
Adjusted in	$\begin{bmatrix}V_1 & V_2 & V_3 & V_4\end{bmatrix}$	$=$	$\begin{bmatrix}0.964 & 0.985 & 1.024 & 1.045\end{bmatrix}$ pu
Simulation $Q(V)$	$\begin{bmatrix}Q_1 & Q_2 & Q_3\end{bmatrix}$	$=$	$\begin{bmatrix}-2.337 & -0.05 & 2.21\end{bmatrix}$ kVar
Adjusted in	$\begin{bmatrix}V_1 & V_2 & V_3 & V_4\end{bmatrix}$	$=$	$\begin{bmatrix}1.085 & 1.085 & 1.085 & 1.103\end{bmatrix}$ pu
Simulation $P(V)$	$\begin{bmatrix}P_1 & P_2 & P_3\end{bmatrix}$	$=$	$\begin{bmatrix}2.8 & 2.8 & 0.8\end{bmatrix}$ kW

is used. The voltage at the slack bus (bus 1, AC voltage source) is varied across a broad voltage range from below 1pu to above 1.1pu. As only the steady state working point is compared in this investigation, the voltage variation is done in a quasi static fashion, meaning that it is done much slower than any internal inverter dynamics. This is done in order to eliminate the effect of the dynamic behavior of the active and reactive power injection. The voltage at the inverter terminal is measured and compared to simulation results. Fig. 4.15 shows the measurement and simulation results for a 50 s sweep of the the slack bus voltage (black line). It can be seen that the measured and simulated voltage at the inverter terminal coincide. Furthermore it can be seen that both, the $Q(V)$ and $P(V)$ characteristics are active. Thus, the steady state behavior of the photovoltaic model is successfully validated against a real inverter at voltages above 1 pu. This is the basis for the validation of the dynamic behavior of the voltage dependent active and reactive power injection.

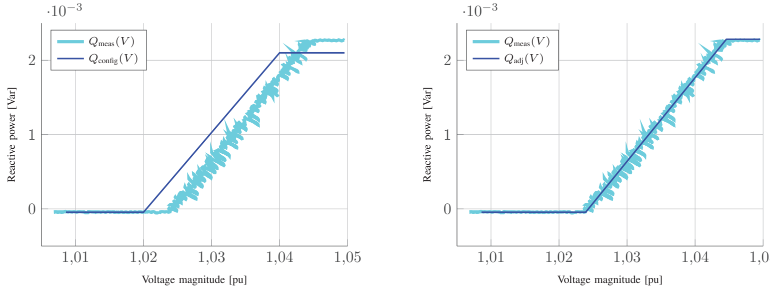

(a) Comparison of the $Q(V)$ characteristic configured in the inverter (Q_{config}) and the measured characteristic (Q_{meas}).

(b) Comparison of the $Q(V)$ adjusted characteristic (Q_{adj}) used in the simulation and the measured characteristic (Q_{meas}).

Figure 4.14: Steady state investigation of the inverter's $Q(V)$ characteristic.

Test setup for dynamic measurements

The dynamic $Q(V)$ and $P(V)$ behavior of the inverter in the laboratory is compared to the behavior of the photovoltaic model in the phasor-framework. Therefore, the response of the inverter to voltage steps at the slack bus (bus 1 in Fig. 4.11) is investigated. The voltage steps are chosen such that the operating point of the inverter shifts from one section of the $Q(V)$ or $P(V)$ characteristic to another. To refer to the different sections of the characteristics, they are divided into eight segments as seen in Fig. 4.16.

During the tests, the setup times of the $Q(V)$ and $P(V)$ characteristics are varied by configuring the web interface of the inverter. A configured setup time of $t_{\text{setup}} = 20\,\text{s}$ in the inverter corresponds to a time constant $T = \frac{t_{\text{setup}}}{3}$ in the photovoltaic model. This is due to the fact that during a step response, the output of a first order delay $\frac{1}{1+Ts}$ reaches a value of 95% of its input within a time of $t = 3T$.

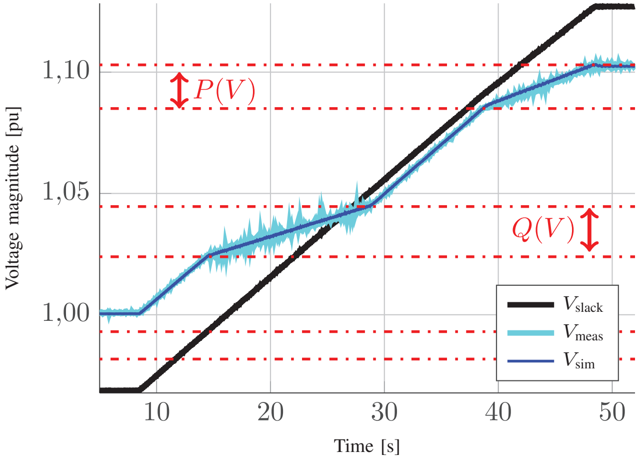

Figure 4.15: Bus voltage at the inverter terminals after a quasi static variation of the slack bus voltage. The adjusted $Q(V)$ and $P(V)$ characteristics are used.

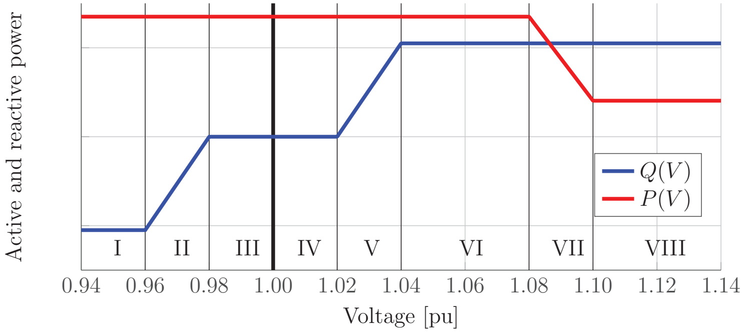

Figure 4.16: Division of the $Q(V)$ and $P(V)$ characteristics into eight sections.

In this thesis, laboratory measurements and simulations are shown for set-up times of 5 s and 20 s for the $Q(V)$ and $P(V)$ characteristic. However, more measurement were performed in oder to further verify the behavior for different setup times.

The $P(V)$ and $Q(V)$ characteristics according to the first and second line of Table 4.4 are configured in the inverter and ,as explained before, the $P(V)$ and $Q(V)$ characteristics of the photovoltaic model in the phasor-framework are parameterized according to the third and fourth line of Table 4.4.

Validation of dynamic behavior of voltage dependent active and reactive power injection

For validating the dynamic inverter behavior of the $Q(V)$ characteristic, a step of the slack bus voltage is applied. Its magnitude is chosen such that the terminal voltage of the inverter jumps from section IV to section V as described in Fig. 4.16. The relation between slack bus voltage $\underline{V}_{\text{slack}}$ and inverter terminal voltage $\underline{V}$ can be derived from Fig. 4.11. It is

$$\underline{V} = \underline{V}_{\text{slack}} + (R + jX) \cdot \underline{I} \tag{4.69}$$

with R and X representing the line parameters and $\underline{I}$ is the terminal output current of the inverter.

Fig. 4.17 and Fig. 4.18 show measurement and simulation results for a setup time of 5 s and 20 s. Both figures are divided into two parts. The left part shows the slack bus voltage $\underline{V}_{\text{slack}}$ as well as the measured and simulated terminal voltages $\underline{V}_{\text{PV, meas}}$ and $\underline{V}_{\text{PV, sim}}$ of the inverter. The right part shows the measured and simulated injected active and reactive power at the the inverter terminal, namely $P_{\text{PV, meas}}$, $P_{\text{PV, sim}}$, $Q_{\text{PV, meas}}$ and $Q_{\text{PV, sim}}$. In both cases, a voltage step at $t = 0$ s is performed such that the operating point moves from section IV to section V as described in Fig. 4.16.

In the measurement results in Fig. 4.17, it can be seen that the injection of reactive power starts with a short time delay of about 0.4 s after the voltage step occurs. Furthermore, it can be seen that the measured and simulated responses match. In the measurement results in Fig. 4.18 it can be seen that, similar to Fig. 4.17, the injection of reactive power starts with a time delay after the voltage step occurs. The delay is approximately 1.4 s.

In both cases (setup time 5 s and 20 s) the simulation and the experimental results match. Furthermore it can be seen that a delay occurs after the step of the slack bus voltage. As mentioned, the delay varies in its length. The root cause for the delay

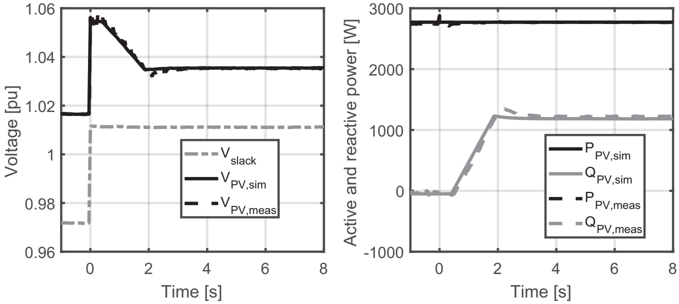

Figure 4.17: Response of the voltage dependent reactive power injection $Q(V)$ to a step of the slack bus voltage for a setup time of 5 s.

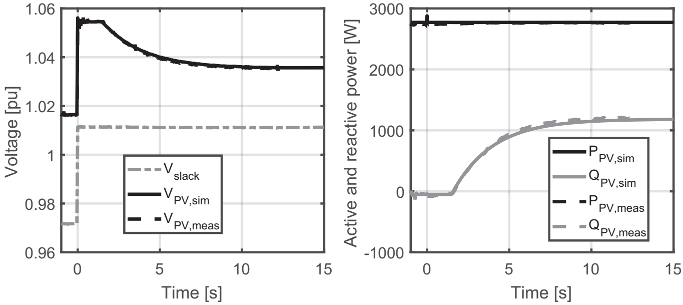

Figure 4.18: Response of the voltage dependent reactive power injection $Q(V)$ to a step of the slack bus voltage for a setup time of 20 s.

is the fact that the first order system is located in front of the $Q(V)$ characteristic. A more detailed explanation is possible by looking at the dynamic model of voltage dependent active and reactive power injection of photovoltaic model in Fig. 4.7, more specifically at the part of the reactive power injection. This part is depicted in Fig. 4.19a. The voltage signal that is entering the first order transfer function is called V_t, the voltage signal that leave the transfer function and enters into the $Q(V)$ characteristic is called V_{delay} and the reference signal for the reactive power is called Q_{ref}. Fig. 4.19b shows these three signals for the case of a setup time of 20 s, thus it is based on the same simulation data as Fig. 4.18. It can be seen that the reactive power starts to increase at time $t = 1.42$ s. Before that, the voltage V_{delay} is below 1.024 pu, which is the value of V_3 for the $Q(V)$ characteristics from Table 4.4 that was configured in the photovoltaic model in the phasor-framework. With Fig. 4.19a and Fig. 4.19b it becomes clear that the delay that occurs during the step in the slack bus voltage and the reaction of the inverter is due to the fact that the voltage signal that enters the $Q(V)$ characteristic is delayed by the first order system $\frac{1}{1+T_{\text{Q}}}$. The duration of the delays depends on two basic variables. First, on the time constant T_{Q}. Secondly, it depends on the initial and final steady state value of the terminal voltage. If, for example, the initial terminal voltage V_t was below 1.01 pu, the delay would have been longer because the time that the voltage V_{delay} needed until it reached 1.024 pu would have been longer.

In order to also verify the dynamic behavior of the active power injection, steps of the slack bus voltage are applied such that the terminal voltage of the inverter jumps from section VI to section VII as described in Fig. 4.16. The simulated and measured results for a setup time of 5 s and 20 s are displayed Fig. 4.20 and Fig. 4.21. It can be seen that also in case for the active power injection a delay happens. The reason for the delay is the same as for the reactive power injection explained above. The measurement and simulation results match well.

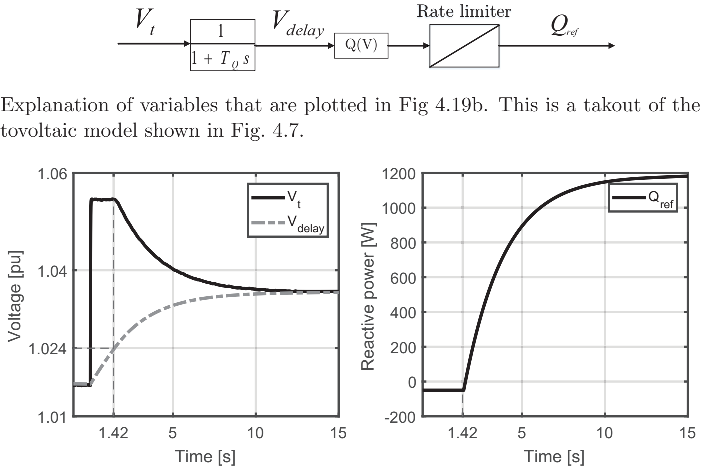

(a) Explanation of variables that are plotted in Fig 4.19b. This is a takout of the overall photovoltaic model shown in Fig. 4.7.

(b) Terminal voltage before and after the first order system (left) and reference reactive power (right) for a setup time of 20 s. See Fig. 4.19a for explanation of variables.

Figure 4.19: Illustration of the reason for the delay of the reactive power injection after a voltage step at the slack bus. The reactive power is injected after the voltage V_{delay} increases above 1.024 pu which is value V_3 in line three of Table 4.4.

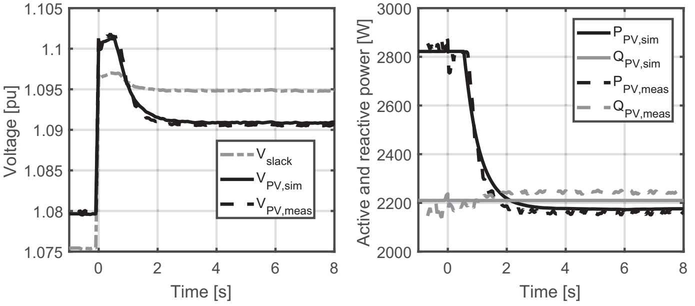

Figure 4.20: Comparison of simulated and measured response of the voltage dependent active power injection $P(V)$ to a step of the slack bus voltage for a setup time of 5 s.

Discussion of measurement results

The $P(V)$ and $Q(V)$ characteristics configured in the inverter have a slight offset, compared to the measurements. The offset is smaller than 0.005 pu. However, the

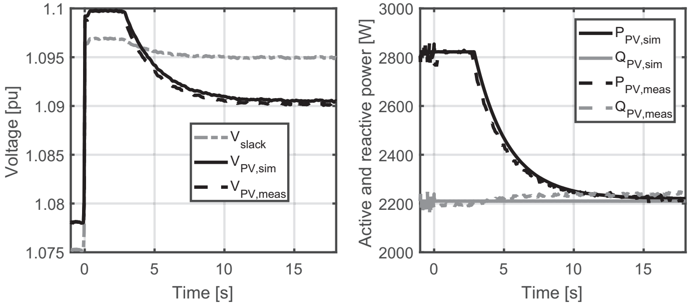

Figure 4.21: Comparison of simulated and measured response of the voltage dependent active power injection $P(V)$ to a step of the slack bus voltage for a setup time of 20 s.

effect of this offset onto the dynamic performance was canceled out by using adapted parameters for the simulation. The most important result from the measurements is that the dynamic behavior of the active and reactive power injection could be modeled correctly with the photovoltaic model developed in this thesis. However, it has to be noted that the correctness of measurement and simulation strongly depends on the implementation of the controls by the manufacturer, the model type of the inverter and the manufacturing date. Thus, a close collaboration with manufacturers is a strong benefit whilst developing such models for research purposes.

All in all the developed photovoltaic model is a valid representation of the inverter investigated. As the implementation of the $Q(V)$ and $P(V)$ control is done differently by each manufacturer it is virtually impossible to create a generic model. Generic models could only be generated if all controls of all manufacturers are implemented and then selected with various types of selectors. However, variations of this model can easily be adopted within the phasor-framework. For that, only the existing model needs to be duplicated and adjusted. Due to the rapid prototyping capability of the phasor-framework, this is possible with minimal effort.

Chapter 5

Diesel-PV Microgrid Study

5.1 Introduction

In this chapter, the capabilities of the developed phasor-framework are shown by performing a study of the reconnection behavior of photovoltaic (PV) systems in low-voltage (LV) microgrids that are powered by a diesel generator as main source of power supply. All the functionalities presented in this work are used in this chapter. The efficient power flow routine developed in chapter 2 is used as an initialization routine for the phasor-framework developed in chapter 3. Futhermore, the developed models for the synchronous generator, the diesel unit and the PV system presented in chapter 4 are also used in this study. Thus, all simulation results presented in this chapter are based on self coded models as well as grid algorithms and the chapter shows the capability of the developed phasor-framework to perform a microgrid analysis.

There are situations in which a diesel generator is used to supply a LV grid with residential loads.

- During maintenance of the medium-voltage (MV) to LV transformer, mobile emergency diesel generators can be used to ensure the power supply of the LV grid. In Germany, the standard procedure during MV/LV transformer maintenance is to operate a diesel unit with a higher frequency set-point in order to disconnect all PV systems from the grid due to their over-frequency protection. Thus, the diesel generator is usually operated in frequency control mode.

- Furthermore, emergency diesel generators are used to supply LV networks during system outages at the MV level, which is especially important for LV grids with sensitive infrastructure, e.g. hospitals and nursing homes [88].

- Moreover, the power supply of LV grids in remote areas, which are not connected to a transmission system, is often realized by diesel generators. For example, a high number of island and micro grids which are also powered by diesel units are most likely going to be installed in India [89].

In all of the above situations, PV systems can be used to relieve diesel units and save fuel [90]. The installed capacity of PV systems that these networks can handle needs to be addressed. Furthermore, it needs to be determined which behavior - regarding frequency control - for these PV systems is optimal to guarantee system stability and allow optimal economic grid operation. One choice would be to use the same behavior as for grid connected systems. Other choice would be to define grid codes, which are specific adapted to the needs of PV-diesel island systems.

Applications for industrial LV microgrids based on diesel generators and PV systems have already been implemented by various companies and institutions [91, 92]. In these settings, the PV systems are usually of substantial size, exceeding the capacity of PV rooftop systems connected to residential LV grids. Furthermore, in research projects or practical applications, the frequency control often relies on communication between diesel generator and the distributed energy resource [93, 94].

The contribution of this chapter, in addition to showing the capability of the developed phasor-framework, is the investigation of the reconnection behavior of small-scale PV systems in a German residential LV network without the presence of communication. The focus is on PV systems that adhere to the German LV grid code VDE 4105 [78] from 2011 (here called new PV systems) and on PV systems that were built prior to 2011 (here called old PV systems). Furthermore, the goal of this study is to investigate the reconnection of a mix of old and new PV systems in a diesel powered residential LV network considering the impact of different grid code requirements.

This chapter is structured as follows: In Section 5.2 the network model and the frequency control strategy of the diesel generator is explained. In Section 5.3 and 5.4 the reconnection of new and old PV systems is investigated, respectively. In Section 5.5 the reconnection of a mix of new and old PV systems is investigated. A conclusion is presented in Section 5.6.

This chapter is partly based on the publication

D. Fetzer, G. Lammert, T. Paschedag, D. Lafferte, K. Fischbar, M. Nuhn, C. Jaehner, H. Becker, L.R. Roose, M. Braun, *Reconnection of Photovoltaic Systems in Low-Voltage Diesel-Powered Microgrids*, 1st International Conference on Large-Scale Grid Integration of Renewable Energy in India, New Delhi, September 6-8 2017 (published in the conference's proceedings)

5.2 Modelling

The investigations are performed with a 3-bus network and a 120-bus LV grid, provided by a German grid operator. In both grids, the diesel is connected to the LV side of the MV/LV transformer. The frequency control of the diesel is designed for a successful interaction with the PV systems.

5.2.1 Networks

The 3-bus grid is displayed in Fig. 5.1a. The diesel generator is connected to a PV system and to a load via two NAYY 4x150 cables of length 100 m.

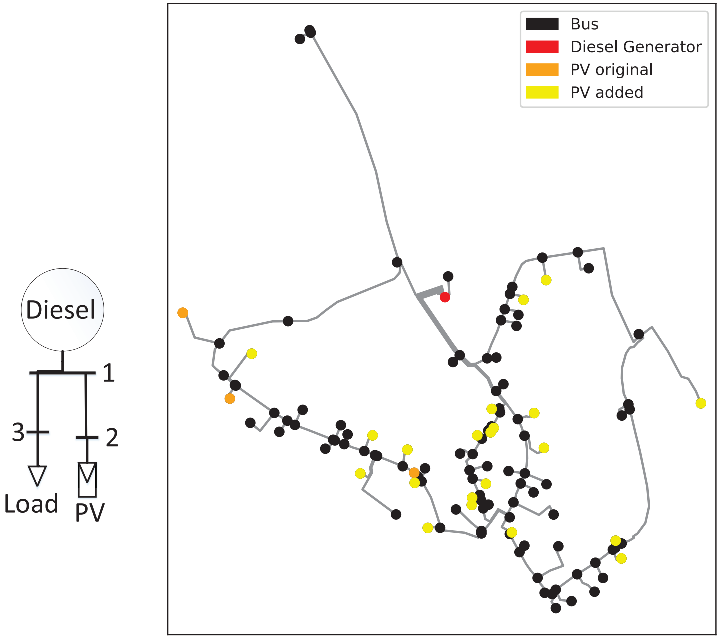

(a) 3-bus network.

(b) 120-bus LV grid (original PV systems in orange, PV systems added for this study in yellow).

Figure 5.1: Network topologies for the study.

The 120-node network is shown in Fig. 5.1b. In its basic configuration, it has a maximum load of 230 kVA, distributed among 150 households and 3 PV systems with a total installed power of 90 kVA. In the configuration with increased presence of PV systems, there are 21 PV units installed. They have a total nominal power of 210 kVA (10 kVA each).

5.2.2 Diesel frequency control

The diesel generator used for this study has a nominal power of $P_{\mathrm{n,diesel}} = 250\,\mathrm{kW}$. The minimal permanent load of a diesel generator is typically 30 % of the nominal power [95], which is $P_{\mathrm{min}} = 75\,\mathrm{kW}$ for this engine. If the output power falls below

$P_{\min}$ for longer time periods, e.g. for many hours, the maintenance requirement of the diesel generator is increased and its lifetime is compromised.

There are two main design goals for the f(P) control of the diesel generator:

1. The f(P) control of the diesel generator should be attuned to the P(f) behavior of the PV systems such that the infeed of PV power is as high as possible.

2. The f(P) control should reduce the time in which the diesel generator is operating below its minimal power $P_{\min}$.

For obtaining a reasonable engineering compromise between the two goals, the operation of the diesel generator in the range from 40 kW to 75 kW is assumed to be acceptable for about half an hour but not for long-term operation [95].

The f(P) control characteristics chosen for the investigation in this study is shown in Fig. 5.2. The diesel generator is operated in isochronous control mode for output power above 80 kW and in droop control mode if the output power is below 80 kW. The droop is chosen in such a way, that the output frequency is 50.2 Hz at an output power of 75 kW. This value is chosen because new PV plants, that adhere to VDE 4105 [78], start to reduce their output power at frequencies above 50.2 Hz. Furthermore, the frequency is controlled to 51.5 Hz at an output power of 40 kW. Above 51.5 Hz, all PV systems disconnect from the system. It can be assumed that the operation in the region of 40 kW to 75 kW is indeed temporary, meaning not longer than a couple of hours. This assumption is reasonable if the minimal load demand of the grid is well above $P_{\min}$ during night, when no PV in-feed is present and all load is covered by the diesel generator. This is the case for the 120-node LV grid investigated in this study.

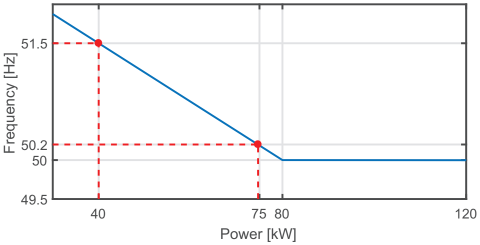

Figure 5.2: Above an output power of 80 kW, the diesel generator works in isochronous control mode (at 50 Hz) and below an output power of 80 kW the diesel generator works in droop control mode with a droop of 0.0375 Hz/kW.

5.3 Reconnection of new PV systems

In this section, the reconnection of new PV systems is investigated. The PV systems are modelled according to VDE 4105 as described in Section 4.4. For this investigation, the 3-bus system introduced in Section 5.2 and displayed in Fig. 5.1a is used.

The PV system at bus 2 and the load at bus 3 are modelled as aggregated elements. Furthermore, the following steps are assumed for the investigation:

1. The LV network is not supplied with power from the MV grid, for example due to a blackout.
2. An emergency diesel generator is connected to the LV side of the MV/LV transformer to resupply the LV system and form an island grid. The diesel generator is initially operated at 50.1 Hz in isochronous control mode. This control mode is maintained until the cold-load pickup phenomenon decayed.
3. The frequency control mode of the diesel generator is switched from isochronous control mode (50.1 Hz) to the f(P) control scheme explained in Section 5.2.2 and displayed in Fig. 5.2. This third step marks the start of the investigation. As the cold load pickup phenomenon is not part of this investigation, the first two steps will not be presented and discussed here as they are presented in [96].

Three scenarios are investigated. In the first scenario, the available power of the aggregated PV system is smaller than the entire load. In the second scenario, the available PV power is larger than the load consumption. In the third scenario, the total load is below the minimal power P_{min} of the diesel generator. During all scenarios, it is assumed that the available PV power P_{avail} is equal to the nominal power of the PV inverters. This corresponds to a weather situation on a sunny day during noon.

5.3.1 Available PV power smaller than load

In this scenario, the reconnection of PV systems is analyzed for the case in which the consumption is $P_{\mathrm{Load}} = 200\,\mathrm{kW}$ and the nominal power of the PV inverter is $P_n = 100\,\mathrm{kW}$. The simulation results can be seen in Fig. 5.3. In the first seconds, the frequency control mode of the diesel generator is switched from isochronous operation at 50.1 Hz to the f(P) control mode. Once the frequency is controlled to 50 Hz and the reconnection condition is fulfilled, the PV system is reconnected and the feed-in PV power is ramped up. Furthermore, it can be seen that the power infeed of the PV is limited by a gradient of 10 % of the nominal inverter power per minute, which is $^{10\,\mathrm{kW}}/_{\mathrm{min}}$. Thus, it takes 10 min until the maximum power is reached. The output power of the diesel unit does not drop below 80 kW and therefore an increase of the frequency set-point is not dones according to the f(P) curve of the diesel generator.

5.3.2 Available PV power larger than load

In this scenario, the PV plant has a nominal and available power of $P_{\mathrm{n}} = P_{\mathrm{avail}} = 300\,\mathrm{kW}$. The simulation results are shown in Fig. 5.4. It can be seen that the PV power increases until the frequency reaches 50.2 Hz. At this point, the current PV power is frozen at a value $P_M = 131\,\mathrm{kW}$ and kept constant. It has to be noted that

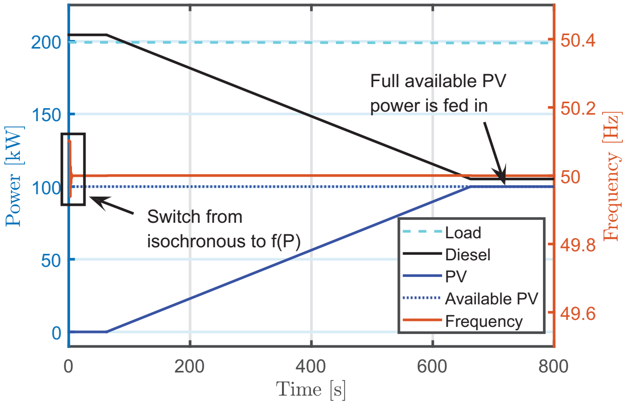

Figure 5.3: PV reconnection for the case $P_{\text{Load}} = 200\,\text{kW}$ and $P_{\text{avail}} = 100\,\text{kW}$ (new PV system).

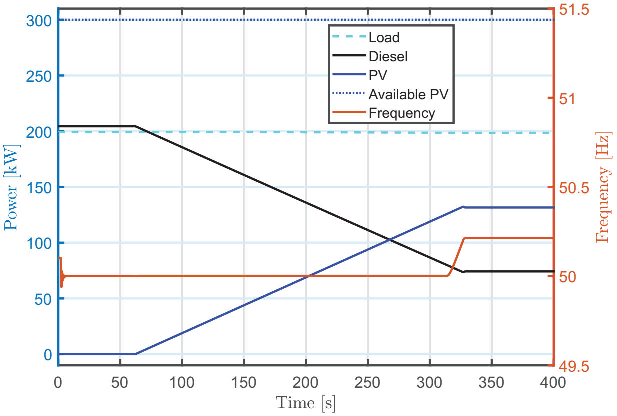

Figure 5.4: PV reconnection for the case $P_{\text{Load}} = 200\,\text{kW}$ and $P_{\text{avail}} = 300\,\text{kW}$ (new PV system).

freezing the output power of the PV system is the key factor to assure a successful reconnection. If the power was not frozen, the PV power would continue to increase. Eventually the diesel generator would rise its frequency due to the f(P) control until $f = 51.5\,\text{Hz}$ and the PV system would disconnect. This occurs in case of old PV systems as will be presented in Section 5.4.

5.3.3 Load smaller than minimum load of diesel unit

In this scenario, the reconnection of new PV systems with $P_\mathrm{n} = P_\mathrm{avail} = 100\,\mathrm{kW}$ is investigated for the case in which the load is less than the minimal power of the diesel generator, namely $P_\mathrm{Load} = 50\,\mathrm{kW}$. The simulation results are displayed in Fig. 5.5. It can be observed that the f(P) control of the diesel generator shifts its frequency to a value above 50.05 Hz. Thus the reconnection condition of the PV system is not fulfilled and the PV system does not reconnect.

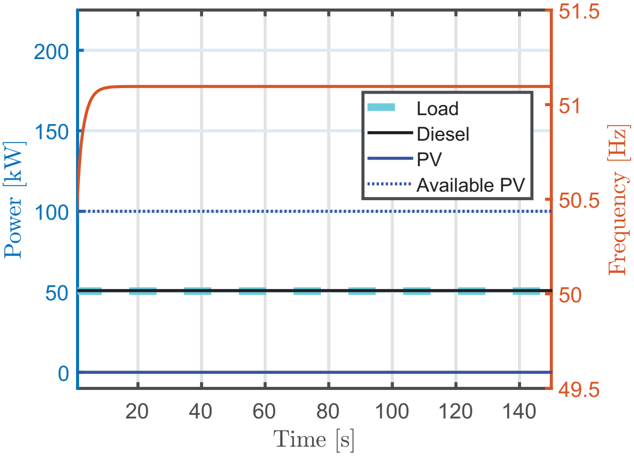

Figure 5.5: PV reconnection for the case $P_\mathrm{Load} = 50\,\mathrm{kW}$ and $P_\mathrm{avail} = 100\,\mathrm{kW}$ (new PV system).

5.4 Reconnection of old PV systems

In this section, the reconnection of old PV systems is investigated. The modelling of old PV systems was described in Section 4.4.4. This analysis uses the same three steps, as already used in Section 5.3 and is conducted with the 3-bus system displayed in Fig. 5.1a. Two scenarios are investigated. In the first scenario, the available PV power is smaller than the consumption. In the second scenario, the PV power injection and the consumption are identical. In both cases an old PV system that was updated is used. Updated PV systems switch off between 50.2 Hz and 51.5 Hz. In this scenario a cut-off frequency of 50.6 Hz is used.

5.4.1 Available PV power smaller than load

In this scenario, the nominal and available PV power is $P_{\mathrm{n}} = P_{\mathrm{avail}} = 100\,\mathrm{kW}$ and the load is $P_{\mathrm{Load}} = 200\,\mathrm{kW}$. It is expected that the PV systems can reconnect without any problem because the diesel generator will supply the difference between the load and the PV power, which is over 100 kW. Thus, the frequency will stay at 50 Hz. The system behavior can be seen in Fig. 5.6. At about $t = 40\,\mathrm{s}$ the PV system increases its output power with a gradient of 25 % of the nominal power per second according to (4.68). At the same time, a slight frequency rise occurs due to the fast increase of the PV infeed. The short frequency increase is due to the response of the spinning reserve to the excess of electric power in the system due to the increase in PV power. However, as the diesel generator has a very fast response time, the governor system is able to reduce the mechanical torque of the diesel generator within a few seconds and restore the frequency to an operation at 50 Hz. Altogether, the reconnection process is successful in this situation and after about 45 s the available PV infeed is reached.

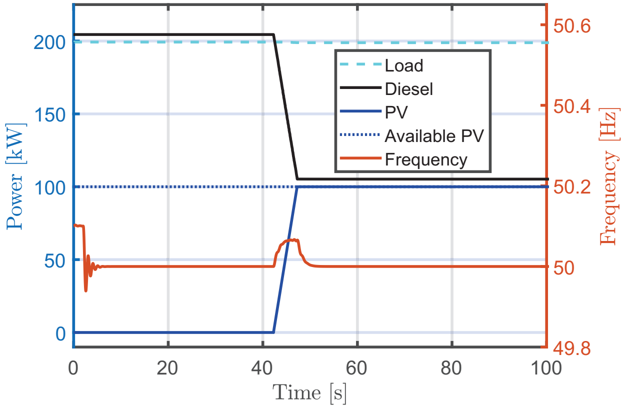

Figure 5.6: PV reconnection for the case $P_{\mathrm{Load}} = 200\,\mathrm{kW}$ and $P_{\mathrm{avail}} = 100\,\mathrm{kW}$ (old PV system with cut-off frequency of 50.6 Hz).

5.4.2 Available PV power identical to load

The simulation results for $P_{\mathrm{n}} = P_{\mathrm{avail}} = 100\,\mathrm{kW}$ and $P_{\mathrm{Load}} = 100\,\mathrm{kW}$ are shown in Fig. 5.7. The cut-off frequency of the PV system is 50.6 Hz. With the increase of PV power injection, the diesel unit reduces its output power. Due to the f(P) characteristic, the diesel generator increases the system frequency to 50.6 Hz (at about $t = 44\,\mathrm{s}$). Therefore, the PV system disconnects from the network, the diesel generator takes over the entire load and restores the original frequency of 50 Hz. At

$t \approx 55\,$s, the same operating condition is present in the system as before the reconnection of the PV system. The process of reconnection and immediate disconnection of the PV system can be seen in more detail in Fig. 5.8. Furthermore, the PV system reconnects once again (at about 85 s) and the whole procedure repeats. Hence, a periodic process of reconnection and disconnection of the PV system occurs. This is a oscillatory instability and needs to be avoided if possible.

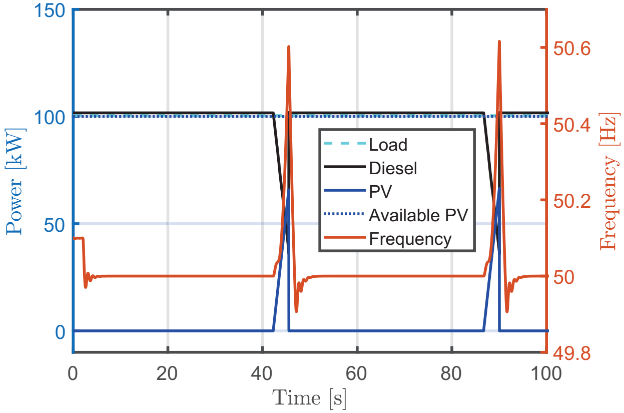

Figure 5.7: PV reconnection for the case $P_{\text{Load}} = 100\,\text{kW}$ and $P_{\text{avail}} = 100\,\text{kW}$ (old PV system with cut-off frequency of 50.6 Hz).

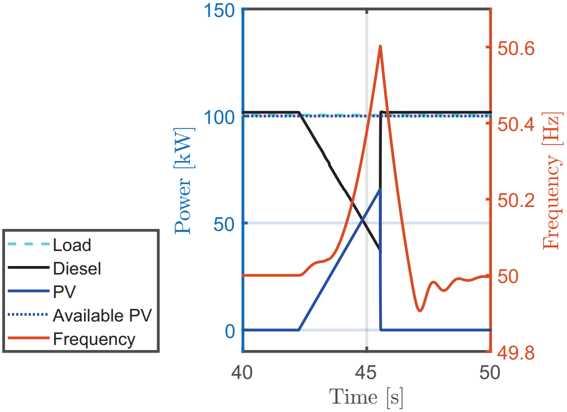

Figure 5.8: Zoom of Fig. 5.7.

5.5 Reconnection of a mix of old and new PV systems

The reconnection of new and old PV systems was investigated in a 3-bus system in sections 5.3 and 5.4, respectively. In real LV grids, both types of PV systems are present. Therefore, the connection of a mix of old and new PV systems is now investigated. For this case study, the 120-bus LV grid, based on real grid data and described in Section 5.2.1 is used. Two scenarios are shown. In the first scenario, 12 new and 8 old PV systems are present in the network. In the second scenario, 3 new and 17 old PV systems are present in the network. Each PV system has a nominal power of 10 kW. The load is $P_{\text{Load}} = 175\,\text{kW}$ in each case. The cut-off frequencies of the old PV systems are distributed in a range between 50.2 Hz and 51.5 Hz. For the reconnection behavior, a worst case assumption is made in which all old PV systems reconnect after 40 s with a time varying maximum power as described in (4.68).

5.5.1 12 new and 8 old PV systems

In this scenario, the 8 old PV systems have cut-off frequencies of f=[51.1, 50.8, 51.4, 50.3, 51.2, 50.9, 50.4, 51.0] Hz. The simulation results are displayed in Fig. 5.9. At about 45 s an increase in PV power is observed. This is due to the rapid reconnection

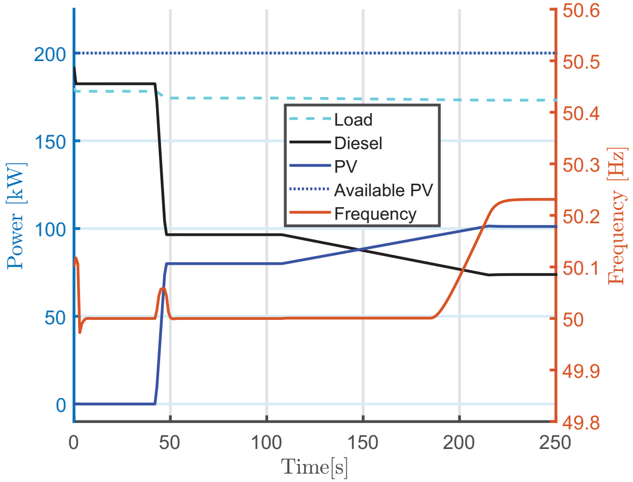

Figure 5.9: PV reconnection in a 120-bus LV network with 12 new and 8 old PV systems. Each PV system has a nominal power of 10 kW. The load is $P_{\text{Load}} = 175\,\text{kW}$. Displayed is the accumulated PV power injection and the consumption.

of the old PV systems which causes a temporary frequency increase as explained in Section 5.4. Because of this frequency increase, the new PV systems wait another 60 s until they also reconnect at time $t = 108$ s. As the power of the diesel generator drops below 75 kW, the frequency is increased to a value above 50.2 Hz and the output power of the new PV systems is frozen. A detailed view on the infeed of each PV system can be seen in Fig. 5.10. All old PV systems with a fixed cut-off frequency connect with their full power of 10 kW. Furthermore, all new PV systems, that behave according to VDE 4105, freeze their output power at about 2 kW. The reconnection process is successful for this configuration. The main reason for this is that the total available power of all old PV systems is low enough such that the diesel generator still feeds in more than its minimal power P_{min}. Due to that the diesel unit does not increase its frequency above the cut-off frequencies of any old PV system.

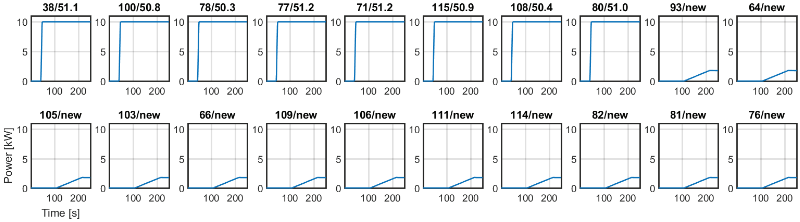

Figure 5.10: Detailed plot of PV infeed powers for the scenario of 8 old and 12 new PV systems. Displayed is the output power of each PV system. The title of each graph displays the bus number of the PV system and the P(f) behavior in a format X/Y in which X is the bus number and Y is the P(f) behavior. The P(f) behavior is either a fixed cut-off frequency (e.g. 50.8 Hz at bus 100; old systems) or according to VDE 4105 (new PV system).

5.5.2 3 new and 17 old PV systems

In this scenario, the total available power of the old PV systems is 170 kW which corresponds to 17 old PV units. This 17 old PV systems have cut-off frequencies of f=[51.1, 50.8, 51.4, 50.3, 51.2, 50.9, 50.4, 51.0, 50.6, 50.4, 50.5, 51.4, 50.3, 50.5, 50,3 50.8] Hz.

As the total load is only 175 kW, a periodic connection and disconnection of the old PV system occurs. This can be seen in Fig. 5.11. At $t = 42$ s the old PV systems reconnect to the system. Shortly after, the output power of the diesel generator is below its minimum output power P_{out} and the frequency is increased. As the cut-off frequency of some of the old PV systems is reached, they disconnect and the frequency drops again to 50 Hz. This procedure is then repeated periodically. The new PV systems do not connect during this scenario because the condition for reconnection (frequency between 47.5 Hz and 50.05 Hz for 60 s), as shown in Fig. 4.9, is never fulfilled. A detailed plot of the power output of each PV system is shown in Fig. 5.12. It can be seen, that most of the old PV systems have an oscillatory behavior. Only the old PV systems with cut-off frequencies of at least 50.6 Hz stay connected.

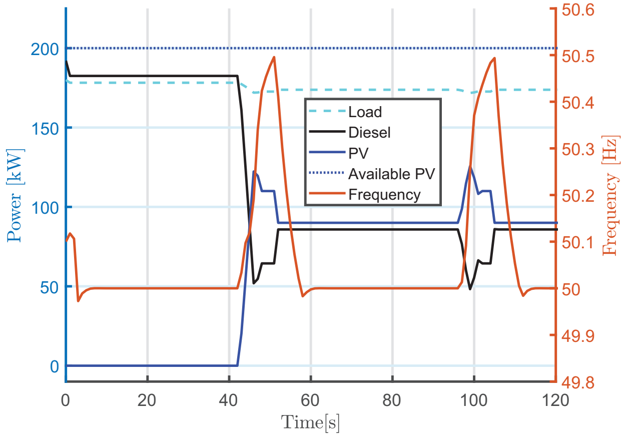

Figure 5.11: PV reconnection in a 120-bus LV network with 3 new and 17 old PV systems. Each PV system has a nominal power of 10 kW. The load is $P_{\text{Load}} = 175\,\text{kW}$. Displayed is the accumulated PV power injection and the consumption.

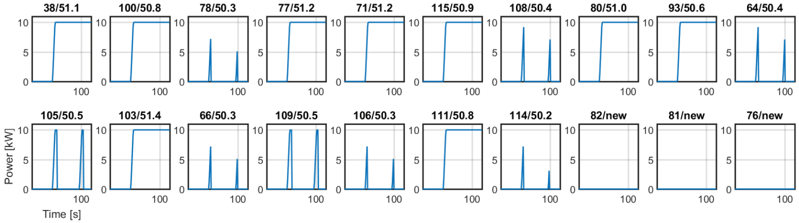

Figure 5.12: Detailed plot of PV infeed powers for the scenario of 17 old and 3 new PV systems. The structure of the plots is the same as in Fig. 5.10.

5.6 Conclusion

In this chapter a case study of the reconnection behavior of PV systems in a low-voltage PV-diesel island network was performed. The case study focused on the reconnection of old and new PV systems with regard to power balance and frequency control. The reconnection of new PV systems was successful in all cases due to their power freezing functionality when the frequency exceeds 50.2 Hz. Moreover, the reconnection of old PV systems can lead to a periodic reconnection and disconnection behavior during the grid restoration process. This can occur if the power infeed of the old PV systems leads to a reduction of the infeed of the diesel generator below its minimum load P_{min} and consequently to a frequency increase above the cut-off frequency of the old PV systems.

The main finding of this chapter is that the power curtailment in case of over-frequency for PV systems, as described in LV grid codes, is also beneficial in microgrids where no communication is present. Thus, grid codes for microgrids should contain a freezing of PV power in case of over-frequency and an active power reduction according to a P(f) characteristics. The optimal slope for active power reduction is a topic for further investigations.

A general rule of thump can be deduced from the case studies conducted in this chapter: The reconnection process of PV systems in a LV network is (under the considered f(P) control presented in this chapter) successful, if the output power of the diesel generator stays above its minimum load under consideration of a full infeed of the available power of all old PV systems. The available power of new PV systems does not need to be considered due to the freezing of their power and their slower reconnection. This can be stated as

$$P_{\text{diesel}} = P_{\text{Load}} + P_{\text{loss}} - P_{\text{avail, old}} > P_{\text{min}} \tag{5.1}$$

where P_{diesel} is the current power infeed of the diesel generator, P_{loss} is the loss power in the network, $P_{\text{avail, old}}$ the available power of the old PV systems and P_{min} the minimal power of the diesel generator. Therefore, a rough estimation of the allowed upper limit for total available power of old PV systems can be deduced:

$$P_{\text{avail,old}} < P_{\text{Load}} + P_{\text{loss}} - P_{\text{min}} \tag{5.2}$$

To increase the security margin and to cover most times of the year, worst case assumptions can be made for the load and the PV infeed. Thus, P_{Load} can be assumed as the minimal load of the LV grid during the year. The calculated $P_{\text{avail,old}}$ is than the maximum value of the nominal power of old PV systems, with which a reconnection would work safely.

As state-of-the-art inverters are all expected to have the freezing functionality, it is expected that the amount of old PV inverters will decrease over time. This is due to the replacement of old or damaged inverters with new equipment. Thus, the problem will become less severe during the next years.

As this chapter only investigated the reconnection behavior, studies concerning the operational behavior are required as well. These are in progress in current research projects at the University of Kassel but not part of this thesis. These studies consider step responses to a change in load and PV generation. Additionally, investigation with realistic time series values for consumption and PV generation are possible.

Chapter 6

Conclusion

6.1 Novelties

Voltage dependent active power injections, also called $P(V)$ and $Q(V)$, were implemented directly into the Newton-Raphson algorithm. In the conventional, state-of-the-art approach, voltage dependent active and reactive power injections are considered via an external loop. With the approach developed in this work, a speed-up of up to one magnitude of computational time, compared to the state of the art approach, could be obtained. Also, the developed power flow algorithm has better convergence properties compared to the state-of-the-art. Furthermore, the developed internal algorithm inherently integrates the $P(V)$ and $Q(V)$ characteristics into the Jacobian matrix and makes the manual tuning of the prefilter in the state-of-the-art external algorithm unnecessary. Therefore, the internal algorithm allows the incorporation of $Q(V)$ and $P(V)$ into static voltage stability analysis investigations and optimal power flow calculations in which the Jacobian is needed.

A dynamic simulation tool, the phasor-framework, was developed during this work. The framework is a dynamic simulation environment that fosters power system and scripting knowledge which is especially useful for research and education. The novelty of the phasor-framework, developed in this thesis, is the combination of four aspects in one single power system simulation tool: Block diagram model development; State-flow integration into the model development; non-black-box property and the focus onto command line usage. This novelty could be reached by using the advantages of a high level, well known and well documented scripting language (MATLAB/Simulink) for dynamic power system simulation. In commercial tools like, e.g., DIgSILENT PowerFactory][18], the model description takes often place in vendor specific languages which are only used by a small user community. Therefore, the user of the tool is often dependent on the support offered by the company. For example, the languages used for model description in DIgSILENT PowerFactory are called DSL and DPL and are only used for the product PowerFactory. Compared to MATLAB/Simulink, DSL and DPL are only used by a tiny user community and the ressources available online are very limited. In the phasor-framework, the user has access to all equations and also access directly to the code. Therefore, the system is no black box. Compared to a commercial tool like DIgSILENT PowerFactory this is a huge benefit. In PowerFactory the user is not able to see the details of the solver and has no option to include his own solution algorithm.

Furthermore, the user can modify or change the components as well as the grid equations in the phasor-framework if necessary. Moreover, data analyzing and visualizing is time efficient with the phasor-framework because the build-in visualization functions of MATLAB/Simulink can be used. In comparison to that, the visualization options in commercial tools are often limited. To create publication grade figures, the user often ends up with exporting the resulting data to a text file and uses a data plotting tool, e.g. MATLAB, which requires additional time. Furthermore, the phasor-framework makes use of vectorization which is a strength of MATLAB. That means that grid and model equations are represented in matrix or vector form. The data format of the phasor-framework is rather simple. That enables test cases to be built up by scripting routines which allows for a fast construction of simulation cases. Thus, the setup of new scenarios and parameter variations is time efficient. In comparison to that, commercial tools frequently rely on a graphical user interface (GUI) for the construction of test cases. On the one hand, a GUI is beneficial for users that are not familiar with scripting. On the other hand, if the user is familiar with scripting, it is oftentimes much faster to use a scripting approach then to drag and drop each and every element by hand on a GUI interface. Following from that, the next benefit of the phasor-framework is that the user acquires power system and scripting knowledge just by using the tool. This is due to the fact that the user has to use scripting and has, to a certain degree, be familiar with power system simulation knowledge. Whilst using the phasor-framework, both of these skills are improved.

Another novelty that is presented in this thesis is the usage of state diagrams directly in the component model development process. Thus, state diagrams do not need to be programmed manually within the model but the Simulink tool *Stateflow* can be used. This makes the model development process very time efficient and, to the knowledge of the author, there is no dynamic power system simulation tool available in which this is possible. This feature is demonstrated during the development of the PV system model by modeling the low-voltage grid code behavior of PV systems for the reconnection process.

Another novelty is the development of a PV model that adheres to the current grid code standard and is validated in the laboratory against an off-the-shelf inverter with the help of time-domain simulations.

Another novelty in this thesis is the investigation of the reconnection behavior of many distributed small PV systems within a diesel-powered island grid in which no communication link is present. The PV systems were modeled according to new and old grid code standards. In state-of-the-art microgrid applications, there are typically only a few PV systems and a communication between the PV and the diesel generator exists. To the knowledge of the author, a reconnection study of multiple

PV systems in a real low-voltage grid has not been performed with validated models that behave according to new grid code standards. The main finding was that the active power curtailment, currently required in grid codes, helps the system to maintain a stable frequency even in cases in which the available PV power exceeds the load. This can be assured by designing the $f(P)$ droop characteristics of the grid forming unit, in this case a diesel generator, in an appropriate way. Through this study, the ability of the phasor-framework is demonstrated to simulated a microgrid system with a significant amount of DER.

6.2 Outlook

The results obtained in this work enables further research activities. Future research could move towards four main areas.

1. On the level of tool development, the phasor-framework could be improved such that the simulation of unconnected grid areas and their synchronization becomes possible. This would enable the simulation of the resynchronization process of two microgrids with each other. Furthermore, the phasor-framework could be adapted in order to be used in Co-simulation tools currently developed, like e.g. OpSim [97]. Moreover, the framework could be expanded for unbalanced, three phase systems. The possible investigations that could be performed in the future with the phasor-framework range from short-term voltage stability to angle and frequency stability.

2. The implementation of the model equations are described in detail in this work. This can serve as a basis to reproduce the results or conduct dynamic grid studies. Furthermore, in future research projects it would be beneficial to validate the P(f) behavior of an off-the-shelf inverter. Moreover, a more detailed synchronous generator model with damper windings could be implemented, in order to simulate faults more accurately. Currently, a phasor-model for a voltage source inverter that serves as a grid forming unit is developed within the phasor-framework.

3. The transformation towards a decentralized electrical energy production will require grid studies with a lot of variables. Through its script based design, the phasor-framework can be used for such dynamic studies which include a lot of parameter variations. Furthermore, the phasor-framework is a very useful tool for usage in undergraduate or graduate courses in power system dynamics to teach practical power system simulation knowledge. The phasor-framework has already been used during Bachelor and Master thesis projects at the University of Kassel with great benefit for the students.

4. The efficient power flow routine developed in this thesis enables the incorporation of voltage dependent active and reactive power injections in applications like voltage stability which needs to have the active and reactive power characteristics within the the Jacobian matrix. Another possible application is

grid planning which often requires the calculation of many power flow cases. Thus, it is impractical to consider voltage dependent power injections with the state-of-the-art external algorithm due to the high computational time. The internal algorithm makes it possible to take active and reactive power characteristics into account during the process of grid planning with only a minimal increase in computational time.

Appendix A

Modeling approach

A.1 Example: Internal VSI and CSI vectors

To give an example for the sizes of the vectors within the phasor-framework, consider a power system with $n = 10$ nodes and $m = 2$ voltage sources. Listing all internal vectors will give a good impression of what is happening within the Simulink model. For this example it is assumed that a slack bus, a synchronous generator, 5 constant power loads and 3 PV systems are present. The slack bus and the synchronous generator are modeled as voltage sources and would be represented by VS1 and VS2 in Fig. 3.6. The constant power loads and the PV system are represented by CS1 and CS2 in Fig. 3.5. Furthermore we assume that the constant power loads (CS1) are connected to the buses $\{3, 4, 5, 8, 9, 10\}$ and that the 3 PV systems (CS2) are connected to buses $\{4, 8, 9\}$. Also it is assumed that the slack bus (VS1) is connected to bus $\{2\}$ and the synchronous generator (VS2) is connected to bus $\{5\}$. A combined overview of the buses and the connected models is also given in Table A.1. In (A.1a) and (A.1b) the internal vectors of the current source models are shown.

Table A.1: Overview of example with two voltage source types and two current source types.

Bus	1	2	3	4	5	6	7	8	9	10
Component	CS1	VS1	CS1	CS2	VS2	CS1	CS1	CS2	CS2	CS1

$$V_{\text{out}} = \begin{bmatrix} V_1 \\ V_3 \\ V_4 \\ V_6 \\ V_7 \\ V_8 \\ V_9 \\ V_{10} \end{bmatrix}, V_{\text{CS1}} = \begin{bmatrix} V_1 \\ V_3 \\ V_6 \\ V_7 \\ V_{10} \end{bmatrix}, V_{\text{CS2}} = \begin{bmatrix} V_4 \\ V_8 \\ V_9 \end{bmatrix}, \tag{A.1a}$$

$$I_{\text{CS1}} = \begin{bmatrix} I_1 \\ I_3 \\ I_6 \\ I_7 \\ I_{10} \end{bmatrix}, I_{\text{CS2}} = \begin{bmatrix} I_4 \\ I_8 \\ I_9 \end{bmatrix}, I_{\text{CS1,full}} = \begin{bmatrix} I_1 \\ I_3 \\ 0 \\ I_6 \\ I_7 \\ 0 \\ 0 \\ I_{10} \end{bmatrix}, I_{\text{CS2,full}} = \begin{bmatrix} 0 \\ 0 \\ I_4 \\ 0 \\ 0 \\ I_8 \\ I_9 \\ 0 \end{bmatrix}, I_{\text{in}} = \begin{bmatrix} I_1 \\ I_3 \\ I_4 \\ I_6 \\ I_7 \\ I_8 \\ I_9 \\ I_{10} \end{bmatrix} \tag{A.1b}$$

It can be seen that the input vector V_{CS1} to CS1 has 5 entries. This is due to the fact that 5 constant power loads are connected to the system. The overall current vector I_{in} is composed of $I_{\text{CS1,full}}$ and $I_{\text{CS2,full}}$. The vector I_{in} is used in the grid equations in (3.6b) and (3.7). The internal vectors of the voltage source models are

$$I_{\text{out}} = \begin{bmatrix} I_2 \\ I_5 \end{bmatrix}, I_{\text{VS1}} = \begin{bmatrix} V_2 \end{bmatrix}, I_{\text{VS2}} = \begin{bmatrix} V_5 \end{bmatrix}, \tag{A.2a}$$

$$V_{\text{VS1}} = \begin{bmatrix} V_2 \end{bmatrix}, V_{\text{VS2}} = \begin{bmatrix} V_5 \end{bmatrix}, V_{\text{in}} = \begin{bmatrix} V_2 \\ V_5 \end{bmatrix} \tag{A.2b}$$

It can be seen that the dimensions of the internal vectors is one and that the output dimension is two. This is expected as each voltage source only occurs at one point in the grid. The results voltage vector V_{in} is then fed back into the grid equation (3.6b) and (3.7).

A.2 Adding new components

An overview of the process of developing and adding new components to the phasor-framework is shown in Fig. A.1. The process consists of the following 6 steps.

Step 1 The model equations need to implemented into a Simulink model. That can be done in a separate stand-alone Simulink diagram. The focus of this step is to obtain a mathematically correct implementation of the model equations. The input signals to the model can be a fixed complex current or voltage in order to test the general behavior of the model.

Step 2 After that, the component can be implemented manually into the phasor-framework and the model behavior can be tested in a grid connected situation, preferably in a two bus setting. It is important to notice that this step, out of simplicity reasons, does not include the automatic initialization routines because the focus lays on the test of the grid connected behavior of the model.

Step 3 After the first two steps are completed successfully and a proper functioning of the model is assured, the model can be added to the phasor-framework. For that, the component is first added to the general input data structure.

Step 4 Thereafter, the Simulink model is adjusted in order to be valid for multiple components. This includes testing of all signals of the model as well as testing the model for different inputs and output signals. Furthermore it has to be checked if the relevant model data can be loaded properly from the input data structure of the component.

Step 5 After that, two initialization routines need to be written for the new component. The purpose of the pre-power-flow initializations script is to obtain a valid power flow result. For that, the new component has to be taken into account during the composition of the power flow data. This is done in the scripts summarized in group (a) in Fig. 3.1. The purpose of the post-power-flow initializations script is to initialize the new Simulink component model. Besides initializing the components state variables, the task of this script is (if required) to make automated modifications of the Simulink block diagram in order to ensure that the model works smoothly together with the phasor-framework. This is done by the scripts in summarized in group (c) in Fig. 3.1.

Step 6 Finally, the new component model is tested within the phasor-framework including automatic initialization. This includes testing of various application cases.

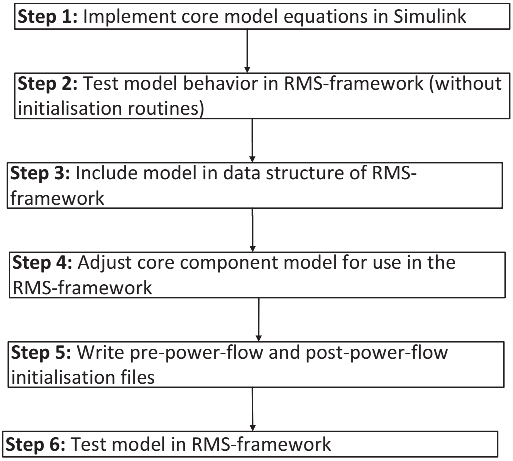
Step 1: Implement core model equations in Simulink
Step 2: Test model behavior in RMS-framework (without initialisation routines)
Step 3: Include model in data structure of RMS-framework
Step 4: Adjust core component model for use in the RMS-framework
Step 5: Write pre-power-flow and post-power-flow initialisation files
Step 6: Test model in RMS-framework

Figure A.1: Overview of the process of developing and adding a new component to the phasor-framework.

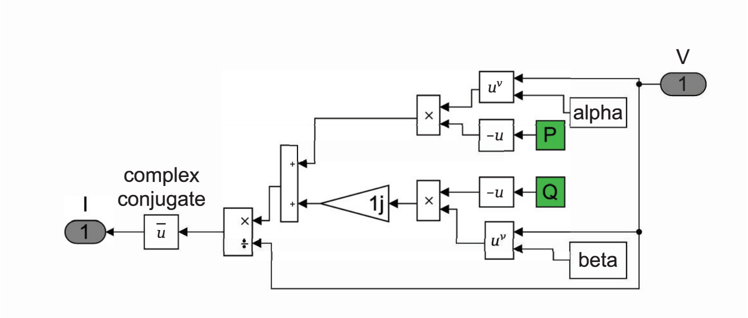

Figure A.2: Fist step of model development of a constant power load: Stand alone Simulink model of the basic equations.

Example: Adding constant power load model

As an example, the steps needed to add a constant power load with timeseries, named Cpl_ts in the phasor-framework are explained. This simple example practically demonstrates all necessary steps that need to be done during the process of adding a new component to the phasor-framework.

Step 1 The constant power load is modeled with a voltage dependency, thus the basic equation for this model is

$$\underline{I} = \text{conj}\left(\frac{PV^{\alpha} + jQV^{\beta}}{\underline{V}}\right) \tag{A.3}$$

The model equations are added in a stand-alone Simulink block. This can be seen in Fig. A.2. In this diagram an input output relationship for a single constant power load is modeled according to (A.3). Furthermore, tests of the input-output relationship are conducted until it is clear that the implementation of (A.3) is correct.

Step 2 The constant power load model is implemented in a two-bus system in the phasor-framework. Only a single load is used and the model is not added to the input data format yet. Instead of this, the component is added manually as a current source model and the general interaction in grid connected mode is tested.

Step 3 The model is included into the data structure of the phasor-framework. Listing A.1 shows the MATLAB code that is used to do that. The components data structure consists of a table *mpc.cpl_ts* which has four columns. The bus, which the constant power load is connected to, is stored in the first column. The timeseries with active and reactive power values is stored in the second column. The sample component is connected to bus -1. This means that this component has no effect in the phasor-simulation as all components that are connected to negative buses are ignored. For incorporating a realistic constant power load into a data structure, the table *mpc.cpl_ts* can be edited. The parameters α and β are set to 0.62 and 0.96 as default values that are typical for a European power grid [98].

Step 4 Following the construction of the data structure of the model, the core component model is adjusted such that the model can be included into the phasor-framework. Figure A.3 shows the Simulink block diagram of the adjusted Simulink model for the *cpl_ts* model. It can be seen that an input data processing and an output data processing part is added to the model. In the input data processing part, a struct with all timeseries values of all constant power loads is converted into a bus signal. This part is crucial as it is a Simulink programming issue and needs special attention in the second initialization script. After that the signals are ordered in the correct way and multidimensional signals of active and reactive power are fed into the core model equations party already explained above. The multidimensional bus current signal is then fed into and assignment block which takes care of ordering the current signals in a proper way such that it fits to the grid model. Furthermore, a measurement block converts complex bus voltages and currents of all components into a Simulink bus signal which contains active and reactive powers and the load angle. Basically, the final model is a composition of the models core equations and data processing.

Step 5 After that, two initialization files are written. In the pre-power flow initialization script, the active and reactive powers of the constant power load at time $t = 0$ from the table *mpc.cpl_ts* are added to the matrix *mpc.bus* in which die active and reactive powers for the power flow calculation are stored. Listing A.2 shows the code that is used for that. In the post-power-flow routine the

Listing A.1: Adding the component to the input data structure.

```
 bus=-1;       % bus number
 P=0;          % active power
 Q=0;          % reactive power
 t=1;          % time
 alpha=0.62; % active power dependency
 beta=0.96;  % reactive power dependency
 ts=timeseries([P; Q],t);         % creating
    timeseries
% zero-order hold interpolation method
 ts=setinterpmethod(ts, 'zoh');
% create table with sample data
 ts = setinterpmethod(ts, 'zoh');
mpc.cpl_ts=cell2table({bus, ts,alpha, beta},...
'VariableNames',{'Bus', 'PQ','alpha', 'beta'});
```

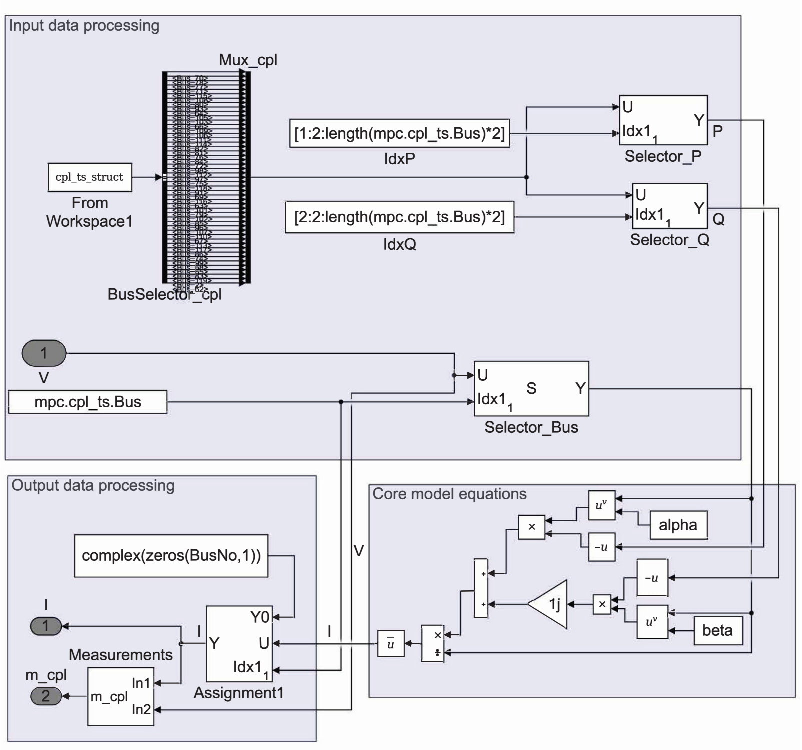

Figure A.3: Adjusted Simulink model

input and output data processing parts of the constant power load model are adjusted according to the underlying data. The connections from the *BusSelector_cpl* to the *Mux_cpl* block seen in Fig. A.3 in the *Input data processing* area are automatically drawn by this script.

Listing A.2: Pre-power flow initialization routine for constant power load model.

```
%List of bus numbers of all cpl_ts components
Bus_ts =mpc.cpl_ts.Bus;
for i=1:length(Bus_ts)
%Extract bus number of present component
bus = Bus_ts(i);;
% Save active and reactive power of i-th constant power load  at time t=0 in variables P_ts and Q_ts
[P_ts Q_ts]=mpc.cpl_ts.PQ(i).Data(1,:);
% Add P_ts and Q_ts to the static data for correct power flow results while taking care of differnt per unit systems
mpc.bus(bus,3)=mpc.bus(bus,3)+P_ts*mpc.baseMVA;
mpc.bus(bus,4)= mpc.bus(bus,4)+Q_ts*mpc.baseMVA;
end
```

Appendix B

Numerical Example for Internal Algorithm

A numerical example for the internal algorithm presented in Chapter 2 is given. For that, a low-voltage feeder with photovoltaic systems is used. The feeder topology can be seen in Fig. B.1. It consists of 19 nodes and 5 PV systems. As listed in Table B.1, seven loads, each having a power of 3 kW are connected to the feeder.

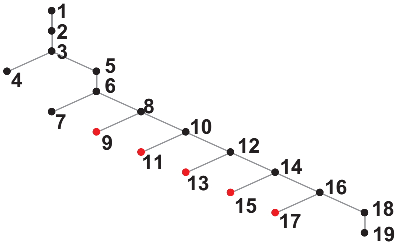

Figure B.1: Topology of the example Grid. Photovoltaic systems are highlighted in red.

Table B.1: Load data of the test feeder.

Bus	Load [kW]	Bus	Load [kW]
5	3	12	3
7	3	15	3
8	3	18	3
11	3		

The branch data is given in Table B.2 in per unit. The base power is 1 MV A and the base voltage is 230 V. The slack bus is located at bus 1 and has a fixed voltage of $1.04\angle 0°$ pu. The PV systems are located at buses 9, 11, 13, 15, 17, having an available active power infeed between 30 and 38 kW. Their voltage dependent active and reactive power characteristics are depicted in Table B.3.

Table B.2: Branch data of the example feeder in per unit notation. The base power is 1 MVA and the base voltage is 230 V.

From	To	r	x	From	To	r	x	From	To	r	x
1	2	0.017	0.094	6	7	0.060	0.008	6	5	0.018	0.007
2	3	0.432	0.067	16	17	0.060	0.008	18	19	0.060	0.008
18	16	0.018	0.007	14	15	0.060	0.008	8	6	0.018	0.007
16	14	0.018	0.007	12	13	0.060	0.008	5	3	0.224	0.035
14	12	0.018	0.007	10	11	0.060	0.008	10	8	0.018	0.007
12	10	0.018	0.007	8	9	0.060	0.008	4	3	0.060	0.008

Table B.3: Voltage dependent active and reactive power characteristics for the photovoltaic systems connected to the example low voltage feeder.

Bus	V_1, V_2, V_3	V_4	y_1, y_2	y_3	V_1	V_2	V_3	V_4	y_1	y_2	y_3
	[pu]	[pu]	[kW]	[kW]	[pu]	[pu]	[pu]	[pu]	[kVA]	[kVA]	[kVA]
9	1.08	1.09	30	10	0.92	0.97	1.03	1.08	-8	0	8
11	1.08	1.09	32	10	0.92	0.97	1.03	1.08	-8	0	8
13	1.08	1.09	34	10	0.92	0.97	1.03	1.08	-8	0	8
15	1.08	1.09	36	10	0.92	0.97	1.03	1.08	-8	0	8
17	1.08	1.09	38	10	0.92	0.97	1.03	1.08	-8	0	8

A power flow is conducted for three cases: In the first case, all photovoltaic systems are disconnected from the feeder. This cases serves as a reference scenario in order to verify the bus voltages for the case in which only the loads are connected. In the second case the photovoltaic systems feed in their full active power without voltage dependent power injection. In the third case all photovoltaic systems are connected and the voltage dependent active and reactive power injection is active.

The results for the bus voltages for each case can be seen in Table B.4, the injected active powers are depicted in Table B.5 and the injected reactive power are depicted in Table B.6. The example is designed such that voltages above 1.1 pu occur for the first case. Therefore, the voltage dependent active and reactive power injection, which is activated in the third case, results in an infeed of reactive power and a reduction in active power. As expected, the voltage dependent active and reactive power injection, activated in the third case, result in a mitigation of the voltage rise caused by the photovoltaic systems. Therefore the bus voltages for the third case are between the bus voltages of the first and second case.

Table B.4: Bus voltages in per unit for the three cases of the example. In the first case all photovoltaic systems are disconnected from the system (no PV). In the second case (full PV), the photovoltaic systems feed in their maximum active power and in the third case voltage dependent active and reactive power injection is activated (P(V), Q(V).

Bus	Case 1	Case 2	Case 3
	no PV	*full PV*	*P(V), Q(V)*
1	$1.040\angle 0^\circ$	$1.040\angle 0^\circ$	$1.040\angle 0^\circ$
2	$1.040\angle -0.1^\circ$	$1.042\angle 0.7^\circ$	$1.038\angle 0.4^\circ$
3	$1.031\angle -0.2^\circ$	$1.098\angle 1.2^\circ$	$1.066\angle 1.6^\circ$
4	$1.031\angle -0.2^\circ$	$1.098\angle 1.2^\circ$	$1.066\angle 1.6^\circ$
5	$1.027\angle -0.2^\circ$	$1.128\angle 1.4^\circ$	$1.081\angle 2.2^\circ$
6	$1.027\angle -0.2^\circ$	$1.131\angle 1.5^\circ$	$1.082\angle 2.2^\circ$
7	$1.026\angle -0.2^\circ$	$1.131\angle 1.5^\circ$	$1.082\angle 2.2^\circ$
8	$1.026\angle -0.2^\circ$	$1.133\angle 1.5^\circ$	$1.084\angle 2.3^\circ$
9	$1.026\angle -0.2^\circ$	$1.135\angle 1.5^\circ$	$1.085\angle 2.3^\circ$
10	$1.026\angle -0.2^\circ$	$1.135\angle 1.6^\circ$	$1.084\angle 2.3^\circ$
11	$1.026\angle -0.2^\circ$	$1.137\angle 1.6^\circ$	$1.085\angle 2.4^\circ$
12	$1.026\angle -0.2^\circ$	$1.137\angle 1.6^\circ$	$1.085\angle 2.4^\circ$
13	$1.026\angle -0.2^\circ$	$1.138\angle 1.6^\circ$	$1.086\angle 2.4^\circ$
14	$1.026\angle -0.2^\circ$	$1.138\angle 1.6^\circ$	$1.086\angle 2.4^\circ$
15	$1.026\angle -0.2^\circ$	$1.140\angle 1.6^\circ$	$1.086\angle 2.4^\circ$
16	$1.026\angle -0.2^\circ$	$1.138\angle 1.6^\circ$	$1.086\angle 2.4^\circ$
17	$1.026\angle -0.2^\circ$	$1.140\angle 1.6^\circ$	$1.087\angle 2.4^\circ$
18	$1.026\angle -0.2^\circ$	$1.138\angle 1.6^\circ$	$1.086\angle 2.4^\circ$
19	$1.026\angle -0.2^\circ$	$1.138\angle 1.6^\circ$	$1.086\angle 2.4^\circ$

Table B.5: Injected active power of the photovoltaic systems for the three cases of numerical example.

Bus	Case 1	Case 2	Case 3
	no PV	*full PV*	*P(V), Q(V)*
9	0	30	21.0
11	0	32	20.2
13	0	34	19.7
15	0	36	19.4
17	0	38	19.4

Table B.6: Injected reactive power of the photovoltaic systems for the three cases of numerical example.

Bus	Case 1	Case 2	Case 3
	no PV	*full PV*	*P(V), Q(V)*
9	0	0	8.0
11	0	0	8.0
13	0	0	8.0
15	0	0	8.0
17	0	0	8.0

Nomenclature

PV	Photovoltaic
LV	Low-voltage
MV	Medium-voltage
HV	High-voltage
RMS	Root mean square
EMT	Electro magnetic transient
DG	Distributed generator
DER	Distributed energy ressource
RES	Renewable energy resources
GUI	Graphical user interface
$Q(V)$	Voltage dependent reactive power injection, sometimes also called local voltage control.
$P(V)$	Voltage dependent active power injection, sometimes also called local voltage control.

List of Symbols

Power flow algorithm

$\underline{S}_k$	Injected complex power into node k
P_k	Injected active power into node k
Q_k	Injected reactive power into node k
$\underline{S}_{k\ell}$	Complex power flow from branch k to ℓ
$P_{k\ell}$	Active power flow from branch k to ℓ
$Q_{k\ell}$	Reactive power flow from branch k to ℓ
$\underline{F}_k$	Power mismatch at node k
V_k	voltage magnitude at node k
δ_k	voltage angle at node k

Synchronous generator

$\underline{E}_{\mathrm{t}}$	complex terminal voltage phasor
E_{t}	terminal voltage magnitude
$\underline{I}_{\mathrm{t}}$	complex terminal current phasor
V_{ref}	reference voltage magnitude
i_{fd}	Field winding current
e_{fd}	excitation voltage
e_{d}	d-axis stator voltage
e_{q}	q-axis stator voltage
i_{d}	d-axis stator current
i_{q}	q-axis stator current
ψ_{d}	d-axis flux
ψ_{q}	q-axis flux
ψ_{fd}	Excitation flux
$\omega_{\mathrm{ref,gen}}$	speed of the reference generator
ω_{r}	rotor speed of the synchronous generator
$\omega_{\mathrm{gov,ref}}$	reference speed of the governor
$\omega_{\mathrm{gov,ref}}$	reference speed of the governor
$\omega_{\mathrm{ref,gen}}$	speed of the reference generator
T_{m}	mechanical torque
T_{e}	electrical torque
R_{a}	Stator resistance
L_{ad}	Mutual d-axis inductance
L_{ffd}	Damper winding self inductance

L_{d}	Synchronous d-axis inductance
L_{q}	Synchronous q-axis inductance
K_{D}	the damping coefficient
ω_{r}	the mechanical speed of the rotor
$\omega_{\mathrm{ref,gen}}$	the mechanical speed of the reference machine
H	inertia time constant
δ	Rotor angle
VA_{base}	Base power of SG parameters
V_{base}	Base voltage of SG parameters
n_{base}	Base speed
V_{ini}	Initial voltage at SG terminal
p	Number of pole pairs
sat	Saturation
x_{d}	Synchronous d-axis reactance
x_{q}	Synchronous q-axis reactance
x'_{d}	Transient d-axis reactance
x'_{q}	Transient q-axis reactance
x''_{d}	Subtransient d-axis reactance
x''_{q}	Subtransient q-axis reactance
t'_{q0}	OC q-axis transient time constant
t''_{d0}	OC d-axis subtransient time constant
t''_{q0}	OC q-axis subtransient time constant
t'_{d}	SC d-axis transient time constant
t'_{q}	SC q-axis transient time constant
t''_{d}	SC d-axis subtransient time constant
t''_{q}	SC d-axis subtransient time constant
r_{a}	Resistance of the stator
x_{ℓ}	Leakage inductance of stator
k_{D}	Damping
H	Inertia constant
J	Moment of inertia (optional because it depends of H)

Diesel generator

T_1	Variable electric control box
T_2	Variable electric control box
T_3	Variable electric control box
T_4	Variable actuator
T_5	Variable actuator
T_6	Variable actuator
K	Proportional gain Actuator
T_D	Time constant engine
T_{min}	Maximal torque
T_{max}	Minimal torque

Photovoltaic system

T_f	Frequency measurement rise time
T_{P}	Rise time active power calculation
T_{Q}	Rise time reactive power calculation
Pn	Nominal power
$Radiation$	Radiation
p_{ini}	Initial active power injection
q_{ini}	Initial reactive power injection
T_V	Time constant for voltage measurement
T_f	Time constant for frequency measurement
PV_{enable}	Activation of voltage dependent active power injection
T_P	Time constant for dynamic $P(V)$ injection
$p_{chara,v}$	Voltage values [V1 V2 V3 V4] of P(V) according to Fig. 2.1
$p_{chara,p}$	Active power values [P1 P2 P3] of P(V)according to Fig. 2.1
$RateLimRise_p$	Positive rate of change limit for active power setpoint
$RateLimFall_p$	Negative rate of change limit for active power setpoint
QV_{enable}	Activation of voltage dependent reactive power injection
T_Q	Time constant for dynamic $Q(V)$ injection
$q_{chara,v}$	Voltage values [V1 V2 V3 V4] of Q(V) according to Fig. 2.1
$q_{chara,q}$	Reactive power values [P1 P2 P3] of Q(V) according to Fig. 2.1
$RateLimChara\_q$	Positive rate of change limit for active power setpoint
$RateLim_q$	Negative rate of change limit for reactive power setpoint
$maxCosPhi$	Maximum cos(phi)
$P_f\_behavior$	Behavior of frequency dependent active power injection
T_{PV}	Inverter time constant

List of Figures

1.1 Thesis structure 3

2.1 Piecewise function for voltage dependent power injection 8
2.2 Smoothing function and its derivative 9
2.3 Illustration of exemplary active and reactive power characteristics . . 10
2.4 Description of the external algorithm. 13
2.5 Description of the internal algorithm. 16
2.6 Two-bus system with a distributed generator connected to bus 1. . . 18
2.7 Active power mismatch and voltage magnitude for external algorithm 20
2.8 Active power mismatch and voltage magnitude for internal algorithm 21
2.9 Inverse nose curve 22
2.10 Determination of working point for simulated two-bus system 23
2.11 Experimental setup of the two-bus system. 25
2.12 Measured $Q(V)$ and $P(V)$ characteristics of the inverter. 25
2.13 Voltages in the two bus system in the lab. 25

3.1 Workflow of the phasor-framework. 38
3.2 Solution method of the phasor-framework. 39
3.3 Solution method of the phasor-framework. 40
3.4 Simulink implementation of the measurement block for the grid model. 40
3.5 Simulink implementation of the current source models 43
3.6 Simulink implementation of the voltage source models. 43
3.7 Kundur single machine infinite bus system 44
3.8 Plot of the rotor angle in the Kundur single machine infinite bus system for two different fault clearing times t_c. 45
3.9 Result from Kundur [34]. The most important part of the plot is the line with constant E_{fd}. This line corresponds well with the result for the clearing time $t_c = 0.07$ in Fig. 3.8. 46
3.10 Simulating parameter variation with the help of a wrapper script. . . 46

4.1 Overview of synchronous generator model. 53
4.2 Implementation of electrical synchronous generator equations. 55
4.3 Implementation of mechanical synchronous generator equations. . . . 56
4.4 Implementation of the dq-transformation. 57
4.5 Block diagram of diesel generator. 62
4.6 Diesel generator droop characteristics. 63

4.7 Overview of the developed small-scale photovoltaic model. 66
4.8 Frequency dependent active power limitation of photovoltaic systems. 69
4.9 State diagram of the P(f) portion of the model of a new photovoltaic system. 70
4.10 State diagram of the P(f) portion of the model of an old photovoltaic system. 71
4.11 Laboratory setup for testing the small-scale photovoltaic system model. 72
4.12 Devices used for the laboratory setup. 72
4.13 AC source performing a voltage step 73
4.14 Steady state investigation of the inverter's $Q(V)$ characteristic. 75
4.15 Inverter terminal voltage after a quasi static variation of the slack bus voltage. 76
4.16 Division of the $Q(V)$ and $P(V)$ characteristics into eight sections. . . 76
4.17 Comparison of simulated and measured reactive power injection response for a setup time of 5 s. 77
4.18 Comparison of simulated and measured reactive power injection response for a setup time of 20 s. 78
4.19 Illustration of reactive power injection delay. 79
4.20 Simulated and measured step response for a setup time of 5 s 79
4.21 Simulated and measured step response for a setup time of 20 s 80

5.1 Network topologies for the study. 83
5.2 Frequency control scheme of the diesel generator. 84
5.3 PV reconnection: New PV systems. 86
5.4 PV reconnection: New PV systems. 86
5.5 PV reconnection: New PV systems. 87
5.6 PV reconnection: New PV systems. 88
5.7 PV reconnection: Old PV systems. 89
5.8 PV reconnection - Detailed plot for old systems. 89
5.9 PV reconnection: Mix of old and new systems. 90
5.10 PV reconnection: Mix of old and new systems. Detailed plot 91
5.11 PV reconnection: Mix of old and new systems. 92
5.12 PV reconnection: Mix of old and new systems. Detailed plot 92

A.1 Overview of the process of developing and adding a new component to the phasor-framework. 101
A.2 Fist step of model development of a constant power load 102
A.3 Adjusted Simulink model 104

B.1 Topology of the example Grid. Photovoltaic systems are highlighted in red. 107

List of Tables

1 Mapping between contents of the thesis and corresponding publications. vi

2.1 Voltage Dependent Power Injection for Distributed Generators 7
2.2 Input data for power flow tool. The data format corresponds to the static portion of the RMS-framework data format described in Table 3.3. 17
2.3 Field *PQULoad*. 17
2.4 Execution modes of the power flow tool. 18
2.5 Parameters of the simulated two-bus system 19
2.6 Voltage characteristic of the simulated two-bus system 19
2.7 Power flow results of the simulated two-bus system 19
2.8 Interim results for each external iteration i of the *external algorithm* for $P(V)$ characteristic of the simulated 2-bus system 23
2.9 Interim results for each internal iteration ν of the *internal algorithm* for $P(V)$ characteristic of the simulated 2-bus system 24
2.10 Voltage characteristics for the performance test of the IEEE 118-bus test system and the real German 234-bus grid. 26
2.11 Comparison of external and internal algorithm (average values and variances. 27

3.1 Comparison between MATLAB-based tools 32
3.2 Properties of phasor-framework 33
3.3 Fields of the input data struct. The data that is needed for the initialization routine is marked with an asterix *. 36
3.4 Input data table for a constant power load with time series. 36
3.5 Input data table for definition of a fault. 44
3.6 Comparison of initial voltage values for fault simulation of SMIB. . . 45
3.7 Input data for parameterizing the fault in the SMIB system. 45

4.1 Input data format for synchronous generator (SG). OC=open circuit, SC=short curcuit 58
4.2 Parameters of the diesel generator 62
4.3 Input data format for photovoltaic model. 67
4.4 Original and adjusted power characteristic setpoints 74

A.1 Overview of example with two voltage source types and two current source types. 99

B.1 Load data of the test feeder. 107
B.2 Branch data of the example feeder in per unit notation. The base power is 1 MVA and the base voltage is 230 V. 108
B.3 Voltage dependent active and reactive power characteristics for the photovoltaic systems connected to the example low voltage feeder. . . 108
B.4 Bus voltages in per unit for the three cases of the example. In the first case all photovoltaic systems are disconnected from the system (no PV). In the second case (full PV), the photovoltaic systems feed in their maximum active power and in the third case voltage dependent active and reactive power injection is activated (P(V), Q(V). 109
B.5 Injected active power of the photovoltaic systems for the three cases of numerical example. 109
B.6 Injected reactive power of the photovoltaic systems for the three cases of numerical example. 109

Listings

A.1 Adding the component to the input data structure. 103
A.2 Pre-power flow initialization routine for constant power load model. 105

Bibliography

[1] European Commision DG Energy, *Study on Technical Assistance in Realisation of the 2016 Report on Renewable Energy, in preparation of the Renewable Energy Package for the Period 2020-2030 in the European Union.* 2017.

[2] DNV-GL, *Energy Transition Outlook.* 2017.

[3] A. Ipakchi and F. Albuyeh, "Grid of the future," *Power and Energy Magazine, IEEE*, vol. 7, pp. 52–62, March 2009.

[4] J. von Appen, M. Braun, T. Stetz, K. Diwold, and D. Geibel, "Time in the sun: The challenge of high pv penetration in the german electric grid," *Power and Energy Magazine, IEEE*, vol. 11, pp. 55–64, March 2013.

[5] A. Monti and F. Ponci, "Power grids of the future: Why smart means complex," in *Complexity in Engineering, 2010. COMPENG.*

[6] A. Woyte, V. Van Thong, R. Belmans, and J. Nijs, "Voltage fluctuations on distribution level introduced by photovoltaic systems," *Energy Conversion, IEEE Transactions on*, vol. 21, pp. 202–209, March 2006.

[7] "IEC 60038 standard voltages," *International Electrotechnical Commission*, 1999.

[8] "Voltage characteristics of electricity supplied by public distribution systems," *European Standard EN 50160, CENELEC*, 2011.

[9] G. Lammert, J. C. Boemer, D. Premm, O. Glitza, L. D. P. Ospina, D. Fetzer, and M. Braun, "Impact of fault ride-through and dynamic reactive power support of photovoltaic systems on short-term voltage stability," in *2017 IEEE Manchester PowerTech*, pp. 1–6, June 2017.

[10] S. Karagiannopoulos, P. Aristidou, and G. Hug, "Hybrid approach for planning and operating active distribution grids," *IET Generation, Transmission Distribution*, vol. 11, no. 3, pp. 685–695, 2017.

[11] R. Tonkoski, D. Turcotte, and T. H. M. EL-Fouly, "Impact of high pv penetration on voltage profiles in residential neighborhoods," *IEEE Transactions on Sustainable Energy*, vol. 3, pp. 518–527, July 2012.

[12] M. Liserre, R. Teodorescu, and F. Blaabjerg, "Stability of photovoltaic and wind turbine grid-connected inverters for a large set of grid impedance values," *IEEE Transactions on Power Electronics*, vol. 21, pp. 263–272, Jan 2006.

[13] D. Hill and A. Bergen, "Stability analysis of multimachine power networks with linear frequency dependent loads," *IEEE Transactions on Circuits and Systems*, vol. 29, pp. 840–848, Dec 1982.

[14] E. Vittal, M. O'Malley, and A. Keane, "Rotor angle stability with high penetrations of wind generation," *IEEE Transactions on Power Systems*, vol. 27, pp. 353–362, Feb 2012.

[15] N. Pogaku, M. Prodanovic, and T. C. Green, "Modeling, analysis and testing of autonomous operation of an inverter-based microgrid," *IEEE Transactions on Power Electronics*, vol. 22, pp. 613–625, March 2007.

[16] J. A. P. Lopes, C. L. Moreira, and A. G. Madureira, "Defining control strategies for microgrids islanded operation," *IEEE Transactions on Power Systems*, vol. 21, pp. 916–924, May 2006.

[17] G. Lammert, K. Yamashita, L. D. Pabón Ospina, H. Renner, S. Martínez Villanueva, P. Pourbeik, F.-E. Ciausiu, and M. Braun, "International Industry Practice on Modelling and Dynamic Performance of Inverter Based Generation in Power System Studies," *CIGRE Science & Engineering*, vol. 8, June 2017.

[18] DIgSILENT GmbH *PowerFactory 2018*.

[19] W. F. Tinney and C. Hart, "Power flow solution by newton's method," *Power Apparatus and Systems, IEEE Transactions on*, vol. PAS-86, pp. 1449–1460, Nov 1967.

[20] F. Milano, *Power System Modelling and Scripting.* Springer, 2010.

[21] A. Cauchy, "Methode general pour la resolution des systemes d'equations simultanees," *Comptes Rendus Hebd. Seances Acad Sci*, pp. 536–538, 1847.

[22] A. A. Goldstein, "Cauchy's method of minimization," *Numer. Math*, pp. 146–150, 1962.

[23] L. Armijo, "Minimization of functions having lipschitz continuous first partial derivatives.," *Pacific J. Math.*, vol. 16, no. 1, pp. 1–3, 1966.

[24] Deuflhard, *Newton Methods for Nonlinear Problems : Affine Invariance and Adaptive Algorithms.* Berlin: Springer, 1966.

[25] T. Stetz, K. Diwold, M. Kraiczy, D. Geibel, S. Schmidt, and M. Braun, "Techno-economic assessment of voltage control strategies in low voltage grids," *Smart Grid, IEEE Transactions on*, vol. 5, pp. 2125–2132, July 2014.

[26] S. Ghosh, S. Rahman, and M. Pipattanasomporn, "Local distribution voltage control by reactive power injection from pv inverters enhanced with active power curtailment," in *PES General Meeting — Conference Exposition, 2014 IEEE*, pp. 1–5, July 2014.

[27] G. Kryonidis, E. Kontis, A. Chrysochos, and M. a. Demoulias, C.S. Farivar, "A simulation tool for extended distribution grids with controlled distributed generation," in *PowerTech*, 2015.

[28] M. Farivar, L. Chen, and S. Low, "Equilibrium and dynamics of local voltage control in distribution systems," in *Decision and Control (CDC), 2013 IEEE 52nd Annual Conference on*, pp. 4329–4334, Dec 2013.

[29] F. Andren, B. Bletterie, S. Kadam, P. Kotsampopoulos, and C. Bucher, "On the stability of local voltage control in distribution networks with a high penetration of inverter-based generation," *Industrial Electronics, IEEE Transactions on*, vol. PP, no. 99, pp. 1–1, 2014.

[30] R. Campaner, M. Chiandone, F. Milano, and G. Sulligoi, "New rules to employ distributed generators in voltage control: Assessment and numerical validation using dome," in *Clean Electrical Power (ICCEP), 2013 International Conference on*, pp. 128–132, June 2013.

[31] E. Demirok, D. Sera, R. Teodorescu, P. Rodriguez, and U. Borup, "Evaluation of the voltage support strategies for the low voltage grid connected pv generators," in *Energy Conversion Congress and Exposition (ECCE), 2010 IEEE*, pp. 710–717, Sept 2010.

[32] J. von Appen, T. Stetz, M. Braun, and A. Schmiegel, "Local voltage control strategies for pv storage systems in distribution grids," *Smart Grid, IEEE Transactions on*, vol. 5, pp. 1002–1009, March 2014.

[33] VDE-AR-N 4120:2015-01 , "Technical requirements for the connection and operation of customer installations to the high-voltage network (TCC High-Voltage)," *VDE Standards*, 2015.

[34] P. Kundur, *Power System Stability and Control.* New York: McGraw - Hill, 1994.

[35] X.-F. Wang, Y. Song, and M. Irving, *Modern Power System Analysis.* Springer, 2009.

[36] T. Van Cutsem and C. Vournas, *Voltage Stability of Electric Power Systems.* Springer 2008.

[37] L. Braz, C. Castro, and C. Murati, "A critical evaluation of step size optimization based load flow methods," *Power Systems, IEEE Transactions on*, vol. 15, pp. 202–207, Feb 2000.

[38] S. Iwamoto and Y. Tamura, "A load flow calculation method for ill-conditioned power systems," *Power Apparatus and Systems, IEEE Transactions on*, vol. PAS-100, pp. 1736–1743, April 1981.

[39] S. Tripathy, G. Prasad, O. Malik, and G. Hope, "Load-flow solutions for ill-conditioned power systems by a newton-like method," *Power Apparatus and Systems, IEEE Transactions on*, vol. PAS-101, pp. 3648–3657, Oct 1982.

[40] M. Dehnel and H. W. Dommel, "A method for identifying weak nodes in non-convergent load flows," *IEEE Transactions on Power Systems*, vol. 4, pp. 801–807, May 1989.

[41] MATLAB, *version 8.0.0.783 (R2012b)*. Natick, Massachusetts: The Math-Works Inc., 2012.

[42] R. Zimmerman, C. Murillo-Saanchez, and R. Thomas, "Matpower: Steady-state operations, planning, and analysis tools for power systems research and education," *Power Systems, IEEE Transactions on*, vol. 26, pp. 12–19, Feb 2011.

[43] University Washington, online https://www2.ee.washington.edu/research/pstca/ , *The Power System Test Case Archive.*

[44] A. Trias, "The holomorphic embedding load flow method," in *Power and Energy Society General Meeting, 2012 IEEE*, pp. 1–8, July 2012.

[45] The Mathworks Inc., "High-performance numeric computation and visualization," *Natick, MA*, 2001.

[46] The Mathworks Inc., "Dynamic system simulation software," *Natick, MA*, 2001.

[47] A. Ishchenko, *Dynamics and stability of distribution networks with dispersed generation.* PhD Thesis, University of Technology Eindhoven, 2008.

[48] F. Wagner, *Modeling Software with Finite State Machines: A Practical Approach.* Auerbach Publications, 2006.

[49] R. Toulson, "Advanced rapid prototyping in small research projects with matlab/simulink," in *2008 IEEE International Symposium on Industrial Electronics*, pp. 1–7, June 2008.

[50] A. B. D. Abel in *Rapid control prototyping*, 2006.

[51] Siemens AG *PSS ®E.*

[52] PowerWorld Corporation *PowerWorld power systems simulation package.*

[53] Generel Electric *PSLF V20.*

[54] F. Milano, "An open source power system analysis toolbox," *IEEE Transactions on Power Systems*, Aug 2005.

[55] J. H. Chow and K. W. Cheung, "A toolbox for power system dynamics and control engineering education and research," *IEEE Transactions on Power Systems*, vol. 7, pp. 1559–1564, Nov 1992.

[56] S. Cole and R. Belmans, "Matdyn, a new matlab-based toolbox for power system dynamic simulation," *IEEE Transactions on Power Systems*, vol. 26, pp. 1129–1136, Aug 2011.

[57] G. Sybille, "Simpowersystems users guide, version 4," *published under sublicense from Hydro-Quebec, and The MathWorks,Inc.*, 2004.

[58] S. Ayasun, C. O. Nwankpa, and H. G. Kwatny, "Voltage stability toolbox for power system education and research," *IEEE Transactions on Education*, vol. 49, pp. 432–442, Nov 2006.

[59] F. Milano and R. Zárate-Miñano, "Using python for the development of electrical engineering projects," in *ICERI 2011, Madrid, Spain, 14-16 November 2011*, 2011.

[60] L. Thurner, A. Scheidler, F. Schäfer, et. al, *pandapower - an Open Source Python Tool for Convenient Modeling, Analysis and Optimization of Electric Power Systems*. IEEE Transaction on Power Systems, 2018.

[61] D. Fetzer, G. Lammert, K. Fischbach, M. Nuhn, J. Weide, D. Lafferte, T. Paschedag, and M. Braun, "Modelling of small-scale photovoltaic systems with active and reactive power control for dynamic studies," in *6th Solar Integration Workshop, Vienna, Austria, November 14-15, 2016*, June 2016.

[62] B. Oswald, *Berechnung von Drehstromnetzen. Berechnung stationärer und nichtstationärer Vorgänge mit Symmetrischen Komponenten und Raumzeigern.*, vol. 2. Vieweg+Teubner, 2013.

[63] M. Kezunovic, A. Abur, G. Huang, A. Bose, and K. Tomsovic, "The role of digital modeling and simulation in power engineering education," *IEEE Transactions on Power Systems*, vol. 19, pp. 64–72, Feb 2004.

[64] P. Idowu, "In search of a perfect power engineering program," *IEEE Transactions on Education*, vol. 47, pp. 410–414, Aug 2004.

[65] G. T. Heydt and V. Vittal, "Feeding our profession [power engineering education]," *IEEE Power and Energy Magazine*, vol. 1, pp. 38–45, Jan 2003.

[66] L. N. Hannett, F. P. D. Mlello, G. H. Tylinski, and W. H. Becker, "Validation of nuclear plant auxiliary power supply by test," *IEEE Transactions on Power Apparatus and Systems*, 1982.

[67] K. E. Yeager and J. R. Willis, "Modeling of emergency diesel generators in an 800 megawatt nuclear power plant," *IEEE Transactions on Energy Conversion*, vol. 8, pp. 433–441, Sep 1993.

[68] E. Nasr-Azadani, *Modeling, Stability Analysis, and Control of Distributed Generation in the Context of Microgrids.* PhD Thesis, University of Waterloo, 2014.

[69] A. Monti and F. Ponci, "Power grids of the future: Why smart means complex," in *Complexity in Engineering, 2010. COMPENG '10.*, pp. 7–11, Feb 2010.

[70] Inernational Energy Agency, *Snapshot of global photovoltaic markets.* 2016.

[71] F. T. Manoel Rekinger, "Global Market Outlook for Solar Power / 2015 - 2019," *SolarPower Europe, Technical Report*, 2014.

[72] J. von Appen, M. Braun, T. Stetz, K. Diwold, and D. Geibel, "Time in the sun: The challenge of high pv penetration in the german electric grid," *IEEE Power and Energy Magazine*, vol. 11, pp. 55–64, March 2013.

[73] T. Stetz, F. Marten, and M. Braun, "Improved low voltage grid-integration of photovoltaic systems in germany," *IEEE Transactions on Sustainable Energy*, vol. 4, pp. 534–542, April 2013.

[74] T. Stetz, K. Diwold, M. Kraiczy, D. Geibel, S. Schmidt, and M. Braun, "Techno-economic assessment of voltage control strategies in low voltage grids," *IEEE Transactions on Smart Grid*, vol. 5, pp. 2125–2132, July 2014.

[75] D. Fetzer, G. Lammert, S. Gehler, J. Hegemann, and M. Braun, "A bisection newton power flow algorithm for local voltage control strategies," *International Journal of Electrical Power & Energy Systems, Elsevier*, submitted for publication in 2016.

[76] R. W. Marco Lindner, "A dynamic rms-model of the local voltage control system q(v) applied in photovoltaic inverters," *23rd International Conference on Electricity Distribution*, Lyon, 15-18 June 2015.

[77] F. Andren, B. Bletterie, S. Kadam, P. Kotsampopoulos, and C. Bucher, "On the Stability of Local Voltage Control in Distribution Networks With a High Penetration of Inverter-Based Generation," *IEEE Transactions on Industrial Electronics*, vol. 62, pp. 2519–2529, Apr. 2015.

[78] VDE, *VDE-AR-N 4105:2015 Technical requirements for the connection and operation of customer installations to the low-voltage network.* 2015.

[79] Western Electricity Coordinating Council (WECC) Renewable Energy Modeling Task Force, "WECC PV Power Plant Dynamic Modeling Guide," 2014.

[80] North American Electric Reliability Corporation (NERC) Special Report, "Standard models for variable generation," May 2010.

[81] G. Lammert, L. D. Pabón Ospina, P. Pourbeik, D. Fetzer, and M. Braun, "Implementation and Validation of WECC Generic Photovoltaic System Models in DIgSILENT PowerFactory," *IEEE PES General Meeting 2016, Boston, USA, July 17-21*, 2016.

[82] VDE Germany, Association for Electrical, Electronic & Information Technologies, “Technical requirements for the connection and operation of customer installations to the high-voltage network (TCC High-Voltage),” *VDE application guide (VDE-AR-N 4120)*.

[83] VDE, *E VDE-AR-N 4105:2017-07 (Draft)*. 2017.

[84] F. Meier, J. Kupka, J.-C. Töbermann, M. Braun, “Assessment of active power curtailment methods with regard to the german regulatory context,” *7th Internation Solar Integration Workshop*, October 2017.

[85] R. I. Amirnaser Yazdani, *Voltage-Sourced Converters in Power Systems : Modeling, Control, and Applications*. WILEY, 2010.

[86] G. Lammert, T. Hess, M. Schmidt, P. Schegner, and M. Braun, “Dynamic Grid Support in Low Voltage Grids – Fault Ride-Through and Reactive Power/Voltage Support During Grid Disturbances,” in *Power Systems Computation Conference (PSCC)*, (Wroclaw, Poland), Aug. 2014.

[87] VDEW, *VDEW 2001, Eigenerzeugungsanlagen am Niederspannungsnetz, 4. Ausgabe 2011,Ergänzungen 2005*. 2001.

[88] M. A. Kumar and A. J. Laxmi, “Application of intentional islanding algorithm for distributed energy resources in disaster management,” in *2016 IEEE International Conference on Power System Technology (POWERCON)*, pp. 1–6, Sept 2016.

[89] I. Mitra, T. Degner, and M. Braun, “Distributed generation and microgrids for small island electrification in developing countries: A review,” *SESI JOURNAL - 2008 Solar Energy Society of India*, vol. 18, no. 1, pp. 6–20, 2008.

[90] D. Arent, J. Barnett, G. Mosey, and A. Wise, “The potential of renewable energy to reduce the dependence of the state of hawaii on oil,” in *2009 42nd Hawaii International Conference on System Sciences*, pp. 1–11, Jan 2009.

[91] S. Hartzog, G. D. Smith, L. E. Humble, R. N. Chapman, and J. F. Hoelscher, “A pv-diesel hybrid system for an operational navy facility on san clemente island,” in *Conference Record of the Twenty Third IEEE Photovoltaic Specialists Conference - 1993 (Cat. No.93CH3283-9)*, pp. 1264–1268, May 1993.

[92] I. Mitra, T. Degner, and M. Braun, “Distributed generation and microgrids for small island electrification in developing countries: A review,” *SESI journal*, 2008.

[93] H. Hilal, M. A. M. Oktaufik, A. Prastawa, B. Prasetyo, and R. Hutahaean, “Smart diesel generator to compensate on-grid pv fluctuation: A case study in sumba island indonesia,” in *2016 3rd Conference on Power Engineering and Renewable Energy (ICPERE)*, pp. 33–37, Nov 2016.

[94] S. Sepasi, A. M. Howlader, E. Reihani, and L. R. Roose, “A coordinated approach for frequency control of zero emission based smart pv-wind-battery power system,” in *2016 9th International Conference on Electrical and Computer Engineering (ICECE)*, pp. 166–169, Dec 2016.

[95] C. I. Forum, “The impact of generator set underloading,” *Online 13.01.2018 - https://forums.cat.com/t5/BLOG-Power-Perspectives/The-Impact-of-Generator-Set-Underloading/ba-p/69719*.

[96] D. Lafferte, A. Klingmann, D. Fetzer, G. Lammert, C. Hachmann, T. Paschedag, and M. Braun, “Black start and island operation of distribution grids with significant penetration of renewable resources,” in *1st International Conference on Large-Scale Grid Integration of Renewable Energy in India*, 2017.

[97] F. M. und J.-Christian Töbermann, “Opsim - a smart grid co-simulation environment,” *Opal-RT RT15 Regional User Group Event, Barcelona*, 2015.

[98] G. Lammert, J. C. Boemer, D. Premm, O. Glitza, L. D. P. Ospina, D. Fetzer, and M. Braun, “Impact of fault ride-through and dynamic reactive power support of photovoltaic systems on short-term voltage stability,” in *2017 IEEE Manchester PowerTech*, pp. 1–6, June 2017.

ISBN 978-3-7376-0608-0

Im ersten Teil dieser Arbeit wird ein Algorithmus vorgestellt, der spannungsabhängige Einspeisung von Wirk- und Blindleistung in den Lastfluss-Algorithmus integriert. Es wird eine Beschleunigung von bis zu einer Größenordnung gegenüber dem derzeit gängigen Verfahren, und eine verbesserte Robustheit erreicht.

Im zweiten Teil wird ein Phasor-Framework zur dynamischen Simulation von Stromnetzen vorgestellt. Die wesentliche Neuheit ist die Möglichkeit der Integration von Zustandsdiagrammen direkt in die Komponentenmodelle. Damit wird eine wesentlich schnellere Modellentwicklung ermöglicht als mit verfügbaren Tools.

Im dritten Teil werden Modelle entwickelt und in das Framework integriert. Der Schwerpunkt liegt auf einem Photovoltaik-Modell welches das dynamische P(V), Q(V) und P(f) Verhalten nach VDE 4105 im Bereich Sekunden bis Minuten abbildet.

Im vierten Teil wird das entwickelte Phasor-Framework verwendet, um das Wiederzuschaltverhalten von Photovoltaikanlagen in einem dieselbetriebenen Inselnetz in der Niederspannung zu untersuchen. Die Untersuchung zeigt, dass ein periodisches Ab- und Abschalten von Photovoltaikanlagen vorkommen kann.

kassel
university
press